DEVELOPMENT OF LIQUID COOLING SYSTEM FOR INDUCTION MOTOR

JENWIT SORARAT

A THESIS SUBMITTED IN PARTIAL FULFILLMENT
OF THE REQUIREMENT FOR THE DEGREE OF
MASTER OF ENGINEERING IN AUTOMOTIVE ENGINEERING
(INTERNATIONAL PROGRAM)
INTERNATIONAL COLLEGE
KING MONGKUT'S INSTITUTE OF TECHNOLOGY LADKRABANG
2011

DEVELOPMENT OF LIQUID COOLING SYSTEM FOR INDUCTION MOTOR

JENWIT SOPARAT

A THESIS SUBMITTED IN PARTIAL FULFILLMENT

OF THE REQUIREMENT FOR THE DEGREE OF

MASTER OF ENGINEERING IN AUTOMOTIVE ENGINEERING

(INTERNATIONAL PROGRAM)

INTERNATIONAL COLLEGE

KING MONGKUT'S INSTITUTE OF TECHNOLOGY LADKRABANG

2011

KMITL-2011-IC-M-004-016

Thesis Certification

International College

King Mongkut's Institute of Technology Ladkrabang

Thesis Title	DEVELOPMENT OF LIQUID COOLING SYSTEM FOR INDUCTION MOTOR
Student	Mr. Jenwit Soparat
Student ID.	50061615
Degree	Master of Engineering
Program	Automotive Engineering (International Program)
Thesis Advisor	Assoc. Prof. Dr. Chinaruk Thianpong
Thesis Co-Advisor	Assoc. Prof. Dr. Seiji Okawa
Thesis Co-Advisor	Dr. Chi-na Benyajati
Thesis Reference Number	KMITL-2011-IC-M-004-016

EXAMINERS		SIGNATURES
Assoc. Prof. Dr. Pongjet	Promvonge	P. Promvonge
Assoc. Prof. Dr. Chinaruk	Thianpong	
Assoc. Prof. Dr. Seiji	Okawa	Seiji Okawa
Dr. Chi-na	Benyajati	
Dr. Preechar	Karin	Preechar Karin

Date 8 May 2012 **Time** 13.00 – 15.00

Place National Science and Technology Development Agency

Anantawat Kunakorn

(Assoc. Prof. Dr. Anantawat Kunakorn)

Dean

8 May 2012

Thesis	Development of Liquid Cooling System for Induction Motor
Student	Mr. Jenwit Soparat
Student ID.	50061915
Degree	Master of Engineering
Program	Automotive Engineering (International Program)
Year	2011
Thesis Advisor	Assoc. Prof. Dr. Chinaruk Thianpong
	Dr. Chi-na Benyajati
	Assoc. Prof. Seiji OKAWA

ABSTRACT

The objective of this study was to develop a cooling system of the induction motor by introducing liquid coolant passages on a housing part to obtain higher cooling efficiency than that of conventional totally enclosed fan cooled system (TEFC).

In order to obtain the model of heat source in motor, a study of heat transfer on an induction motor was carried out on 3.7 kW, 3-phases, TEFC motor. The heat generation of motor was obtained by means of motor losses. Furthermore, two locations of thermal contact were studied i.e. stator-to-housing and rotor-to-stator contact. The developed computational model of TEFC motor was validated by means of resulting temperature distribution comparison.

The validated heat generation model was further used in designing a liquid cooling system. Number of passages, flow pattern and flow rate were the parameters considered. The liquid cooled housing was then optimized by a Response Surface approach. The chosen design points were comprised of 50 passages, 10 mm ∅, and parallel flow pattern at 0.1 kg/s flow rate. A capacity of the chosen design of liquid cooled motor was calculated to increase by at least 20% of a rated workload of conventional TEFC motor. With a criterion of keeping a copper winding temperature under the critical temperature of class-F insulator of 155°C, the motor capacity could be increased by approximately up to 40% of the rated workload of conventional TEFC model.

ACKNOWLEDGEMENT

The study was a scholarship in automotive program under Thailand Advanced Institute of Science and Technology and Tokyo Institute of Technology (TAIST Tokyo Tech) which is a collaboration of National Science and Technology Development Agency, Thailand (NSTDA), Tokyo Institute of Technology, Japan, and King Mongkut's Institute of Technology Ladkrabang, Thailand. This study has been carried during the year 2008-2012 as a part of a research project in the Automotive Laboratory, National Metal and Materials Technology Center, Thailand.

I would like to express my gratitude to my advisors, especially, Dr. Chi-na Benyajati for his guidance and encouragement during the work. I would like to thank Mr. Suphakrit Koocharoenprasit for his help in my research work. I am obliged to Miss Foifon Srisawat for revision of the thesis format. In addition, I would like to thank my colleague, my friends and my family for their supports and helps in everything.

The thermogram measurements of an induction motor were carried out by using the infrared camera. I would like to gratefully acknowledge the Faculty of Mechanical Engineering, Chulalongkorn University for their support in this equipment.

Finally, I would like give all merits of this work to my mother Mrs. Sajee Rakpakdee who always stands by me. I hope she can see my success from somewhere.

May 28, 2012

Jenwit Soparat

TABLE OF CONTENTS

TABLE OF CONTENTS (CONT.)

TABLE OF CONTENTS (CONT.)

TABLE OF CONTENTS (CONT.)

LIST OF TABLES

LIST OF FIGURES

LIST OF FIGURES (CONT.)

LIST OF FIGURES (CONT.)

LIST OF FIGURES (CONT.)

LIST OF FIGURES (CONT.)

LIST OF FIGURES (CONT.)

LIST OF FIGURES (CONT.)

CHAPTER 1

INTRODUCTION

1.1 Background

Generally, an induction motor uses 3–phase AC electricity input applied to winding on stator. This causes electro–magnetic effect that induces a rotor to start rotating. Similar to any other machinery, there are some energy losses occurred when an induction motor operates. Most of these losses are represented in heat occurring in a motor. The induction motor losses could be divided into 5 categories, namely, stator I^2R loss, rotor I^2R loss, core loss, friction loss, and stray loss.

The resulting heat directly affects a function of an induction motor, both in durability and efficiency. Major cause of heat is either from an overload input current when starting up the motor, or from when a motor works under high loads at low speed or with changing speed during an operation.

As a result, the cooling system for motor is an important area of study. Generally, the most common induction motor cooling system is Totally Enclosed Fan Cooled (TEFC) type. In this type, a fan is attached at the rear side of motor. The forced convection of air generated by the rear fan takes the heat away from the surface of motor housing. It could be seen that the atmospheric air temperature plays an importance role for the TEFC cooling system. This could become a problem when using induction motors in Thailand where the temperature could be as high as 39 – 43 degree Celsius during summer.

Thus, the focus of the current project was to develop an induction motor for an automotive application. This was because an induction motor had relatively simple structures for manufacturing, durable, and involved low maintenance cost. It could also be applied in various applications. Furthermore, an induction motor could vary a rotational speed after equipped with appropriate electronic equipment.

The concept of a new liquid cooling system was a closed circuit system comprising of radiator, pump, and liquid cooled housing. The liquid cooled housing was developed by means of

accommodating the coolant passages on the housing of the induction motor. The proper cooling system was designed via a finite element method and optimization.

1.2 Objectives

- To study a heat transfer phenomenon in an induction motor
- To obtain a heat generation model for a computational analysis of an induction motor
- To obtain a liquid cooling system to replace a conventional Totally Enclosed Fan Cooled (TEFC) system with an improved motor cooling capacity

1.3 Scopes

- To study a heat transfer phenomenon in the TEFC motor by experimental and computational methods
- To determine an appropriate heat generation and computational model by a comparison of resulting temperature distribution on a motor housing
- To design the liquid cooling system by finite element method using the data of heat transfer on TEFC
- To estimate the operating capacity of the motor installed with the proposed liquid cooled system under a criterion of maximum permissible copper winding insulation temperature

1.4 Thesis Outlines

The thesis is organized in 6 Chapters, the contents of which are summarized as followed:

Chapter 1 : Introduction

This chapter introduces the general background of induction motor, the important of the cooling system for an induction motor, the objectives of this study, and the scopes of work in this study.

Chapter 2 : Literature Reviews

This chapter citations reviews the published literature on the causes of electrical machinery failure, the previous studies and simulations related to the heat transfer of electrical machinery, and governing equation for simulation of heat transfer related to this study.

Chapter 3 : Research Methodology

This chapter explains the process of experiments and simulations. The procedures of research are comprised of the measurement of efficiency and temperature, the experiment of thermal contacts, and the setup of heat transfer simulation.

Chapter 4 : Results

This chapter demonstrates the experimental results of TEFC motor such as motor efficiency and temperature. Then, the simulated results of both TEFC motor and Liquid cooled motor are presented.

Chapter 5 : Discussions

The obtained results from the previous chapters would be discussed in this chapter. The discussions are included with experimental temperature results, the heat generation model, thermal contact resistances, designing of liquid cooling system, and the cooling capacity of both systems.

Chapter 6 : Conclusions

A brief summary of the work is presented in this chapter.

CHAPTER 2

LITERATURE REVIEWS

In general, majority of cooling system for induction motor use air for heat reduction. The Total Enclosed Fan Cool Motor (TEFC) is one of the most popular motor in many industries. Generally, this type of motor has an enclosed housing with a fan attached at the rear side of motor. The fan function is to blow surrounding air to cool down the housing surface. Figure 2.1 shows the example of TEFC Motor.

Figure 2.1 Example of Total Enclosed Fan Cool Motor (TEFC)

In tropical country such as Thailand, the normal surrounding air temperature could be up to 35 $^{\circ}$C. In some applications, a cooling system by air might not be enough for the induction motor such as an electric vehicle. It is therefore necessary to develop a better cooling system for the induction motor. Any induction motor design is thermally limited according mainly to the conductor insulation class. Generally, an insulation life decreases very rapidly with temperature increases over the rated value such that for an extra 10 $^{\circ}$C the lifetime could even be halved [Champrnois et al., 1994].

2.1 Failures in Three-Phase Squirrel-Cage Induction Motor

2.1.1 Insulation Classes of motor

Insulation systems are rated by standard IEC (International Electrotechnical Commission Standard) classifications according to maximum allowable operating temperatures:

Table 2.1 Insulator Classes of Motor [IEC, 2004]

	Temperature Tolerance Class			
	A	B	F	H
Maximum Operation Temperature Allowed (°C)	105	130	155	180
Allowable Temperature rise at full load 1.0 service factor motor	60	80	105	125
Allowable Temperature Rise 1.15 service factor motor	70	90	115	-

Allowable temperature rises are based upon a reference ambient temperature of 40°C. The term "Operation temperature" is normally a combination of reference temperature, allowable temperature rise, and allowance for "hot spot" winding.

2.1.2 Thermal Aging

AIEE 510 [1956] and IEEE 275 [1992] test procedures can be used to determine the effects of temperature on the winding insulation system. This method establishes a minimum insulation life of 20,000 hours for the test sample, namely, a scale model of a stator coil winding, under the prescribed test condition as shown in Figure 2.2. As a rule of thumb, for every 10°C increase in temperature, the insulation life is halved. Figure 2.2 indicates the relationship between the various classes of insulation and operating temperatures. Unless the operating temperature is extremely high, the normal effect of thermal aging is to render the insulation system vulnerable to other influencing factors or stresses that actually produce the failure. Once the insulation system has lost its physical integrity, it no longer resists the normal dielectric, mechanical, and environmental stresses. It should be pointed out that if any of the stresses become severe enough, a winding failure will occur regardless of temperature on thermal aging. There are two obvious

approaches to ensure longer thermal life i.e. either reducing the operating temperature or increasing the class of insulator materials used.

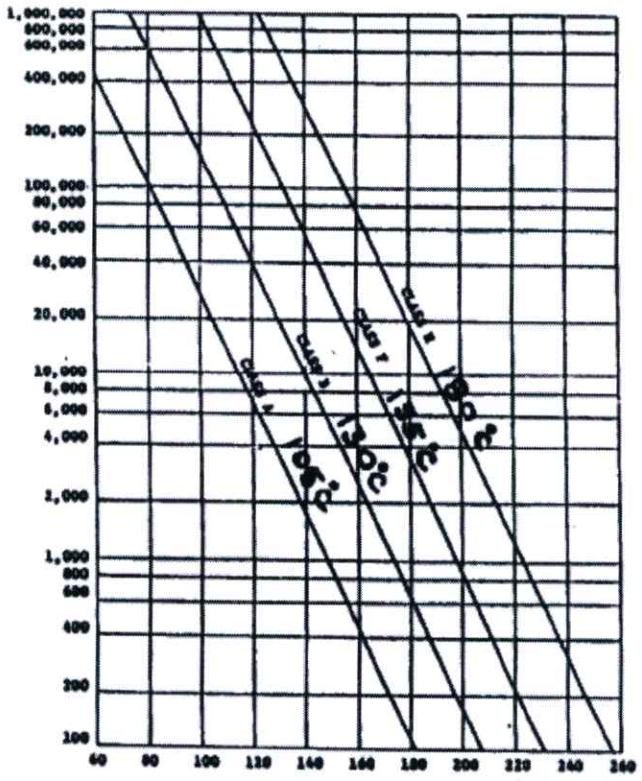

Figure 2.2 Total winding temperature (^{o}C) versus insulator life [Bonnett et al., 1992]

2.1.3 Overloading

Motor manufacturers normally design a certain amount of margin into their motors. This is usually done by designing the motor to operate below the normal limits for a specific insulation system or using an insulation system with a rating that is well above the operating temperature. On the latest NEMA rates, this is usually accomplished by using a class-F insulation system with class-B operating temperatures. Within certain limits, it can be estimated that the winding temperature rise will increase as a square of the load. By using this in conjunction with Figure 2.2 for temperature against life, it is possible to estimate the effect of loading on winding life.

2.2 Previous studies on heat transfer in induction motor

Analytically, one of the most common methods employed to study a heat transfer of electrical machines including an induction motor has been a thermal network method. Generally, the method considers the objects as a homogenous body where temperature is the same all over. The temperature of such a body varies in time if the heat produced inside by losses in the induction motor is applied at a certain point after starting the motor [Boldea et al., 2002]. The heat balance equation is

$$P_{loss} = C_t \frac{d(T-T_0)}{dt} + \frac{(T-T_0)}{R_t} \tag{2.1}$$

where $C_t = Mc_t$, $R_{conv} = \frac{1}{Ah}$, and $R_{cond} = \frac{l}{KA}$

This is equivalent to a parallel electric circuit fed from a current source P_{loss} with a voltage $T - T_0$ as displayed in Figure 2.3

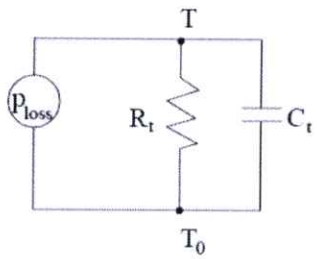

Figure 2.3 Equivalent thermal circuit [Boldea et al., 2002]

For steady state, C_t is excluded from the equation (2.1) and the equivalent circuit in Figure 2.3. The solution of such electric circuit could be represented as

$$T = (T_{max} - T_0)\left(1 - e^{-\frac{t}{\tau_t}}\right) + T_o e^{-\frac{t}{\tau_t}} \tag{2.2}$$

The thermal time constant term $\tau_t = C_t R_t$ is very important as it limits the machine working time depending on a certain level of losses and given cooling conditions. The thermal time constant increases with a machine size and capacity of the cooling system.

Yoon et al. [2005] developed the thermal network for a small TEFC induction motor. This model was a symmetric model along a shaft axis as shown in Figure 2.4. The motor was divided into 44 control volumes. Losses in the motor were considered as a heat source in the thermal analysis. The total loss, the input energy subtracted by the mechanical energy, included the

resistance losses in stator coils and rotor bars, iron loss, friction and windage losses and stray load loss according to IEEE 112. The losses were measured from the locked, no-load, and rated load tests.

It was found that thermal capacitance played an important role in starting and transient operating states. It was related to the time needed to reach steady state acting as a heat sink during the starting time. It was also reported that the largest portion of the generated heat was transferred from the frame to the outer air. There were large differences in the heat transfer rates between both end cap surfaces, which indicated that the assumptions on the symmetric boundary condition in the axial direction might have significant errors.

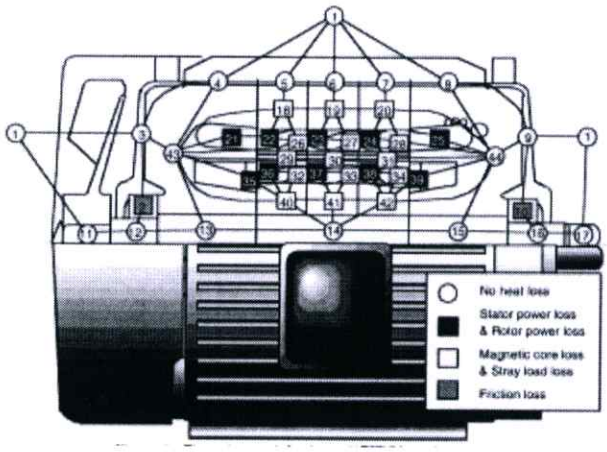

Figure 2.4 Thermal network for small TEFC induction motor [Yoon et al., 2005]

In addition, there have been other various studies on thermal performance of an electrical motor by using a thermal network method such as Sarii et al. [1998] who used the thermal network to investigate a high speed induction machine as shown in Figure 2.5. Majority of proposed models showed that a highest temperature would occur on a wiring on the stator [Huai et al., 2003, Bellettre et al., 2005]. However, one of main limitations for such method was that no detail of temperature contribution on motor parts was provided. Also, part geometries were not taken into the account either.

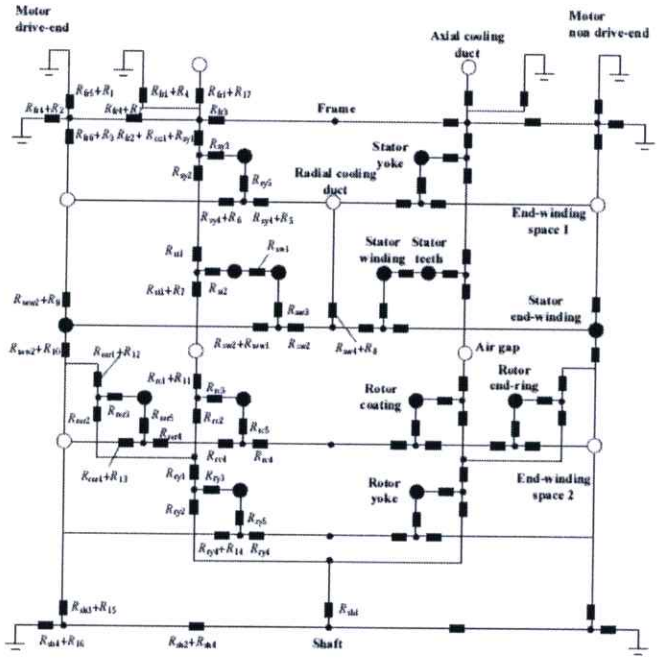

Figure 2.5 A circuit diagram of thermal network for high speed induction machine [Sarii et al., 1998]

In another analytical method, Lee et al. [2002] employed resistance-based temperature estimation (RTE) method by using model-based R_s estimation for stator winding temperature estimation to monitor the stator winding temperature. The results showed the advantages of the method over conventional thermal-model-based temperature estimation (TMTE). However, it was reported that RTE methods were very sensitive to errors in some parameters, especially, during high-speed operation.

Furthermore, another common approach to investigate the heat transfer of induction motor has been an empirical method. Saari et al. [1995] presented equations for a calculation of the average heat transfer coefficient, h. The high-speed machine was divided into different areas or geometries such as air gap, shaft surface, rotor disks, end-winding space, stator core, and frame. Every area of the machine was treated as a particular geometry and the Nusselt number was calculated for every section of machine which provided the average heat-transfer coefficient. There were several convection correlations for the Nusselt number, Nu. The average heat transfer coefficient could be obtained from:

$$h = \frac{k_f Nu}{l} \tag{2.3}$$

Jaaskelainen et al. [2009] then applied such empirical method to determine a heat transfer coefficient in a simulation of 31,500 rpm and 130 kW permanent magnet machine. The empirical and numerical results in the air gap were close to other compared methods. Also, the empirical values of the coefficient of convection for the shaft and the underside area of the end-winding could be determined easily because of their simple geometries and there were not too many disturbances affecting the cooling flow in this area. Only the average velocity needed to be determined for these regions. Nonetheless, the other parts of the machine were not so easy to model empirically i.e. the rotor disks, the end of the stator yoke, the upside area of the end winding and the channel between the stator yoke and the stator frame. The problem was that it was not easy to determine the average velocity of the fluid on the surface as well as complicating geometries. The computer program showed big fluctuations in the velocity on these surfaces. The fluctuations were produced by corners in the machine. It was determined that the airflow behind the end winding was especially turbulent which affected the velocity on the end of the stator yoke surface. These areas could be modeled well enough only by numerically via a computer program.

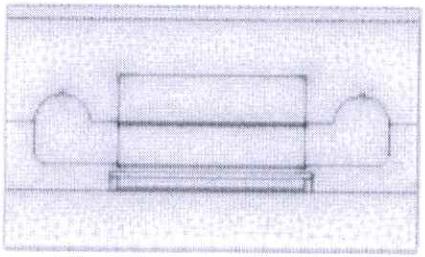

Figure 2.6 The finite element mesh of the 2D symmetric geometry of the high speed electrical machine [Jaaskelainen et al., 2009]

In addition, it has been shown by Sarkar et al. [1998] that, at least in small power induction motors, approximately 80% of the heat loss in the stator coil overhangs was transmitted through conduction to the winding part in slot and to the core. It was also shown that 60 to 70% of rotor losses were transferred through the air gap to the stator core.

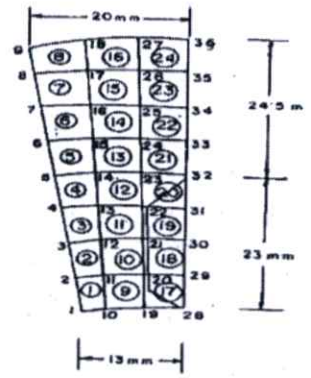

Figure 2.7 Slice of core iron and winding divided into arch shaped finite elements [Sarkar et al., 1998]

Apart from the analytical studies reviewed above, there have also been some of experimental studies on heat transfer behavior of an induction motor. It has been shown by Farsane et al. [2000], a Laser Doppler Anemometry technique was employed to measure air velocity around the motor housing. It was reported that the shape of motor housing had a significant effect on both air velocity and a flow pattern along the housing. Thus, a performance of a motor cooling system could be directly affected by the design of housing and other parts. It was necessary to take into account presence of structures which could obstruct the air flow and reduce air velocity.

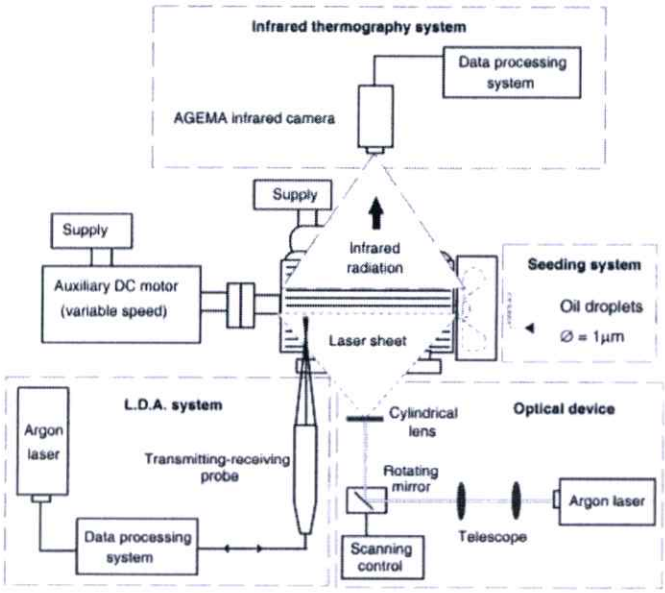

Figure 2.8 Experimental setup of Laser Doppler Anemometer technique for measurement of air velocity along motor housing [Farsane et al., 2000]

2.3 Computational fluid dynamics theory

The one-dimensional convective-diffusion equation can be expressed by considering in x-direction. [Dechaumphai, 2001]

Given c is the specific heat capacity of substrate.

k is the specific thermal conductivity of substrate.

And assume c and k are constant.

$$\rho c \frac{\partial T}{\partial t} - k \frac{\partial^2 T}{\partial x^2} + \rho c u \frac{\partial T}{\partial x} = Q \tag{2.4}$$

The first term on left hand side is the heat accumulation in the body. The second term is the heat diffusion by conduction and the third term is the heat diffusion by convection. In the right hand side Q is the summation of the internal heat generation and the heat diffusion.

2.3.1 Computational Fluid Dynamics in CFX

The instantaneous equation of mass, momentum, and energy conservation are presented [ANSYS-CFX, 2011]. For turbulent flows, the instantaneous equations are averaged leading to additional terms. These terms, together with models for them, are discussed in Turbulence and wall function Theory. The instantaneous equations of mass, momentum and energy conservation can be written as follows in a stationary frame:

The Continuity equation :

$$\frac{\partial p}{\partial t} + \nabla \cdot (\rho U) = 0 \tag{2.5}$$

The Momentum equations :

$$\frac{\partial (\rho h_{tot})}{\partial t} + \nabla \cdot (\rho U \otimes U) = -\nabla p + \nabla \cdot \tau + S_M \tag{2.6}$$

Where the stress tensor, τ, is related to the strain rate by

$$\tau = \mu \left(\nabla U + (\nabla U)^T - \frac{2}{3} \delta \nabla \cdot U \right) \tag{2.7}$$

The Total energy equation

$$\frac{\partial (\rho h_{tot})}{\partial t} - \frac{\partial p}{\partial t} + \nabla \cdot (\rho U h_{tot}) = \nabla \cdot (\lambda \nabla T) + \nabla \cdot (U \cdot \tau) + U \cdot S_M + S_E \tag{2.8}$$

Where h_{tot} is the total enthalpy, related to the static enthalpy $h(T, p)$ by :

$$h_{tot} = h + \frac{1}{2} U^2 \tag{2.9}$$

The term $\nabla \cdot (U \cdot \tau)$ represents the work due to viscous stresses and is called the viscous work term.

The term $U \cdot S_M$ represents the work due to external momentum sources and is currently neglected

2.3.2 $k - \varepsilon$ Turbulence Model

The $k - \varepsilon$ turbulence model is valid for a turbulence transport at high Reynolds number. This model gives a closure to the system and results in the following equations for the conservation of momentum and continuity.

$$\rho \frac{\partial \boldsymbol{U}}{\partial t} - \nabla . \left[\left(\mu + \rho C_\mu \frac{k^2}{\varepsilon} \right) . (\nabla \boldsymbol{U}) + (\nabla \boldsymbol{U})^T \right] + \rho \boldsymbol{U} . \nabla \boldsymbol{U} + \nabla \boldsymbol{P} = \boldsymbol{F} \tag{2.10}$$

$$\nabla . \boldsymbol{U} = 0 \tag{2.11}$$

The two new variables in equation (2.10) are the turbulent kinetic energy k and the dissipation rate of the turbulent energy ε. Two extra equation for k and ε are solved for these two introduced variables :

$$\rho \frac{\partial k}{\partial t} - \nabla . \left[\left(\mu + \rho \frac{C_\mu k^2}{\sigma_k \varepsilon} \right) \nabla k \right] + \rho \boldsymbol{U} . \nabla k = \rho C_\mu \frac{k^2}{2\varepsilon} (\nabla \boldsymbol{U} + (\nabla \boldsymbol{U})^T)^2 - \rho \varepsilon \tag{2.12}$$

$$\rho \frac{\partial \varepsilon}{\partial t} - \nabla . \left[\left(\mu + \rho \frac{C_\mu k^2}{\sigma_\varepsilon \varepsilon} \right) \nabla \varepsilon \right] + \rho \boldsymbol{U} . \nabla \varepsilon = \rho C_{\varepsilon 1} \frac{k}{2} (\nabla \boldsymbol{U} + (\nabla \boldsymbol{U})^T)^2 - \rho C_{\varepsilon 2} - \rho C_{\varepsilon 2} \frac{\varepsilon^2}{k} \tag{2.13}$$

$C_\mu, C_{\varepsilon 1}, C_{\varepsilon 2}, \sigma_k$ and σ_ε are model constants and determined from the experimental data. The values for the coefficients are presented in Table 2.2.

The $k - \varepsilon$ turbulence model gives an isotropic turbulence, which is a turbulence constant in all directions

Table 2.2 Model constants for equation (2.12) and (2.13)

C_μ	$C_{\varepsilon 1}$	$C_{\varepsilon 1}$	σ_k	σ_ε
0.09	1.44	1.92	0.9	1.3

2.3.3 Scalable wall functions

The wall-function approach is an extension of the method of Launder of Spalding. In the log-law region, the near wall tangential velocity is related to the wall-shear-stress (τ_ω) by means of a logarithmic relation.

In the wall-function approach, the viscosity affected sublayer region is bridged by employing empirical formulas to provide near-wall boundary conditions for the mean flow and turbulence transport equations. These formulas connect the wall conditions (e.g., the wall-shear-stress) to the dependent variables at the near-wall mesh node which is presumed to lie in the fully-turbulent region of the boundary layer.

The logarithmic relation for the near wall velocity is given by:

$$u^+ = \frac{U_t}{u_\tau} = \frac{1}{k} ln(y^+) + C \tag{2.14}$$

where $y^+ = \frac{\rho \Delta y u_\tau}{\mu}$ and $u_\tau = \left(\frac{\tau_\omega}{\rho}\right)^{1/2}$.

u^+ is the near wall velocity, u_τ is the friction velocity, U_t is the known velocity tangent to the wall at a distance of Δy from the wall, y^+ is the dimensionless distance from the wall, τ_ω is the wall shear stress, k is the von Karman constant and C is a log-layer constant depending on wall roughness (natural logarithms are used).

Equation (2.14) has the problem that it becomes singular at separation points where the near wall velocity (U_t) approaches zero. In the logarithmic region, an alternative velocity scale, u^* can be used instead of u_τ :

$$u^* = C_\mu^{1/4} k^{1/2} \tag{2.15}$$

This scale has the useful property that it does not go to zero if U_t goes to zero. Based on this definition, the following explicit equation for u_τ can be obtained :

$$u_\tau = \frac{U_t}{\frac{1}{k}\ln(y^*)+C} \tag{2.16}$$

The absolute value of the wall shear stress (τ_ω) is then obtained from:

$$\tau_\omega = \rho u^* u_\tau \tag{2.17}$$

where $y^* = (\rho u^* \Delta y)/\mu$.

2.3.4 GGI and MFR Theory

A control surface approach is used to perform the connection across a GGI attachment or periodic condition. A physically based intersection algorithm is employed to provide the complete freedom to change the grid topology and physically base intersection algorithm is employed to provide the complete freedom to change the grid topology and physical distribution across the interface.

A general intersection algorithm permits connections to be successfully made, even when the resultant surfaces on either side of an interface do not physically " fit" together to form a well-defined physical connection. In addition, an automatic surface trimming function is performed by the GGI algorithm, to account for mismatched surface extent. This means that a GGI attachment or periodic condition can be successfully defined where the surface on one side of the interface is larger (in extent) than the surface on the other side of the interface. The interface is constructed between the overlapping regions of the two sides of the interface.

Multiple Frames of Reference (MFR) allows the analysis of situations involving domains that are rotating relative to one another. For CFX, this feature focuses on the investigation of rotor/stator interaction for rotating machinery. Since MFR is based on the GGI technology, the most appropriate meshing style may be used for each component in the analysis.

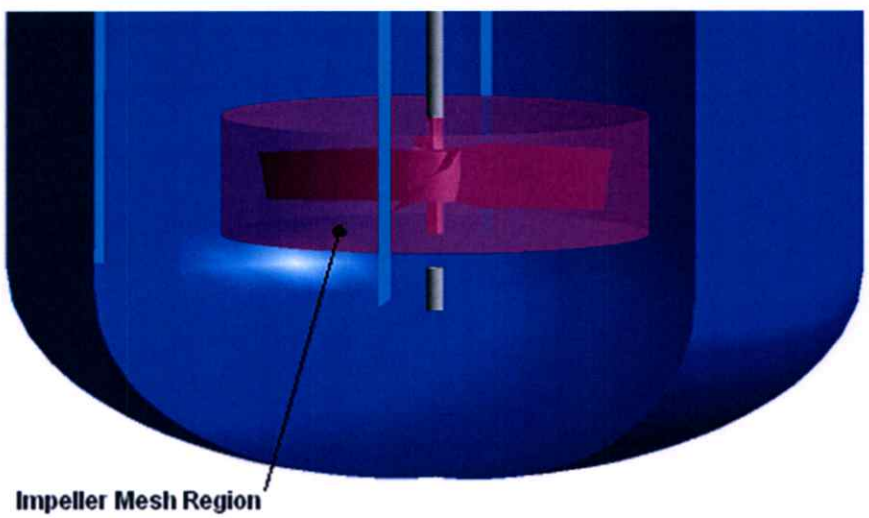

Figure 2.9 Example of Total Enclosed Fan Cool Motor (TEFC)

CHAPTER 3

RESEARCH METHODOLOGY

3.1 Experimental Procedures

3.1.1 Induction Motor Specifications

A 3-phase AC induction motor was the main focus of this work. A small general industrial-type motor, i.e. 5 horsepower, was chosen to allow convenience during all experimental studies. This was based on a concept that all range of 3-phase AC induction motors shared similar structural details and worked under the same principal, and hence a comparable heat generating behavior. Therefore, the results obtained from small-sized induction motor could be applied in a relevant development of larger-scaled induction motors.

Induction motors employed in this study were 3-phase, 4 poles, 5 horsepower industrial type manufactured by Teco Electric and Machinery (Thai). The technical specifications of this motor are shown below in Table 3.1.

Table 3.1 Technical specifications of studied induction motor

Type	Specifications
Manufacturer	Teco Electric and Machinery (Thai)
Cooling system	Totally Enclosed Fan Cooled
Power	3.7 kW
Pole	4
Input Voltage	3-phaseAC 220 V
Nominal rotational speed	1450 rpm
Housing length	0.272 m
Stator length	0.095 m
Shaft length	0.370 m
Wiring length	0.183 m
Stator outer diameter	0.190 m
Rotor outer diameter	0.120 m
Fan diameter	0.240 m

Table 3.1 Technical specifications of studied induction motor (Cont.)

Type	Specifications
StatorandRotor gap	0.0003 m
Stator wiring slots	36
Rotor slots	8
Number of housing fins	23
Number of fan blades	10

A cooling system of the chosen induction motor was Totally Enclosed Fan Cooled (TEFC) in which a rotational movement of a fan located at a rear end of a motor resulted in an air flow that would take away generated heat from a motor housing. General configuration and important components of the employed induction motor are shown in Figure 3.1 - Figure 3.3.

Figure 3.1 General layout of employed 3-phase 5 HP induction motor

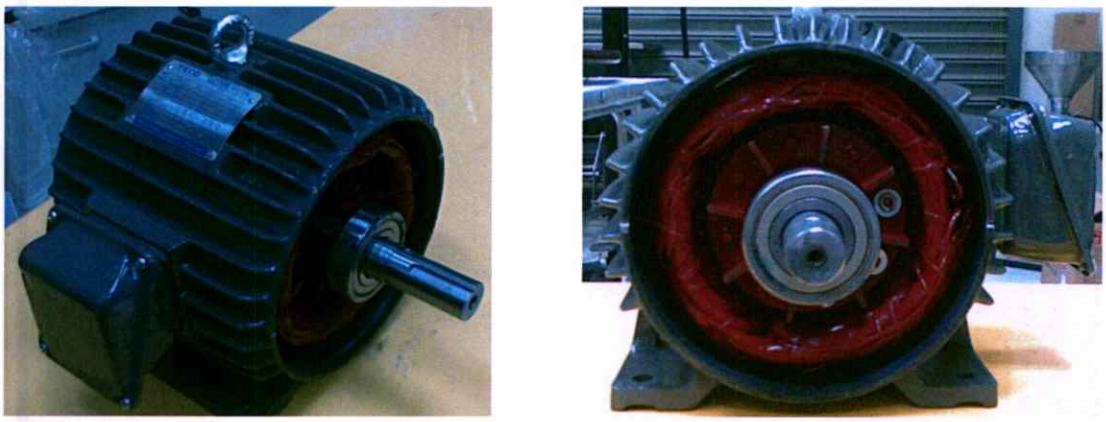

Figure 3.2 Internal layout of employed 3-phase 5 HP induction motor

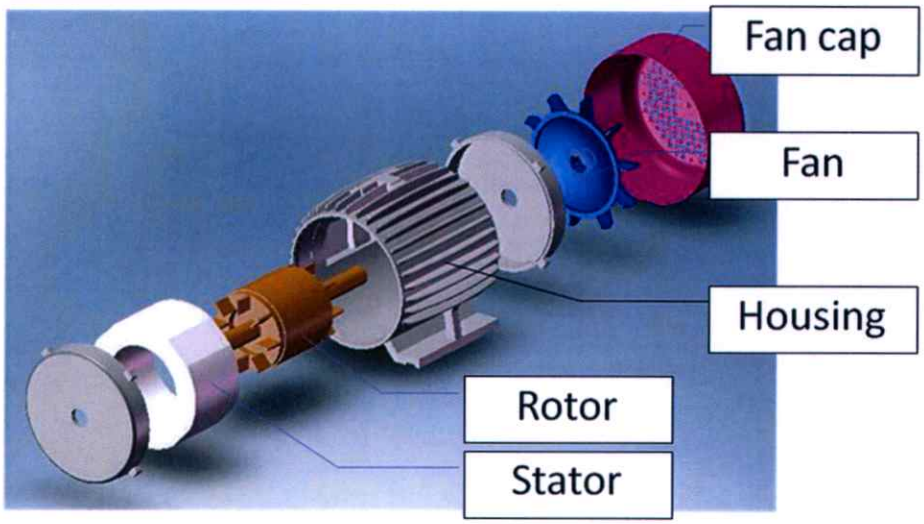

Figure 3.3 Main components of induction motor

As can be seen from Figure 3.3, main components of AC induction motor consist of rotor, stator, housing, fan, and fan cover. Details of each component are described below:

- Rotor: Rotating part located at the central core of a motor. A rotor is comprised of a driving shaft inserted into a center of a rotor core made of series of thin metal sheet compressed together to obtain good electromagnetic properties. Both ends of driving shaft are supported by bearings which are located at front and rear cover of motor in order to reduce a rotational friction during operation.

- Stator: A main portion of stator is made by similar method as that in rotor i.e. a series of thin metal sheet compressed together. At the center, there is a hole with slightly larger diameter than that of rotor. Furthermore, along an inner circumference, array of slots are made to accommodate a copper wiring. Once a current is fed through these wirings, a resulting electromagnetic field would induce a rotor to rotate along its axis.

- Housing: Housing is an external part that holds all the components together in designated locations. Additionally, it functions as a medium to take away heat from internal parts while also protects all the parts from surrounding environment. A housing of motor used in this study was made of casting metal divided into 3 parts i.e. front cover, rear cover, and central body.

- Fan: A plastic fan attached on the rear end of motor driving shaft. The one used in this work had an overall diameter of 19 cm. with total blade number of 10. A fan rotates at the same rotational speed of the induction motor.
- Fan cover:While acting as a safety part relating to a fan, another important function is to direct an air flow resulting from a fan movement. An air inlet is at the rear surface with a square grate pattern while an opposite side is an outlet, which is a series of gap formed between a fan cover and a central body of the housing.

3.1.2 Induction Motor Efficiency Test

A motor efficiency test is generally performed by means of a dynamometer configuration creating a mechanical rotational load on an interested motor. Three main parameters that can be obtained from the test are energy input, work output, and losses. Furthermore, Losses can be divided into 5 parts which are core loss, stator I^2R loss, rotor I^2R loss, friction and windage loss, and stray loss. Majority of these losses are presented in a form of heat.

In order to understand a mechanism of heat generation in an induction motor, a motor efficiency test was carried out on the chosen induction motor under a different load conditions of 100%, 125%, and 150%. All the tests were done at a motor testing centre according to the IEEE 112 and IEC 34-2 standards. The testing configuration where the test motor was attached to a dynamoter is shown in Figure 3.4 and the details of test apparatus are given in Table 3.2.

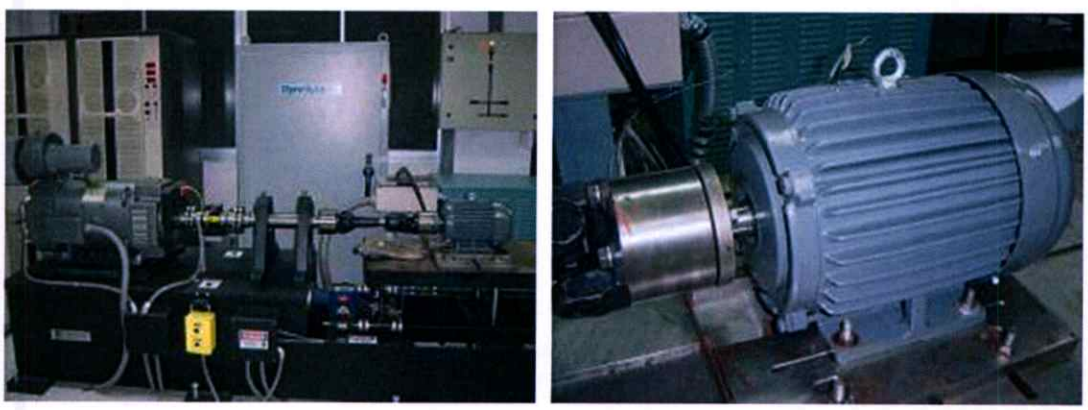

Figure 3.4 Motor efficiency test configuration

Table 3.2 Details of motor efficiency testing apparatuses

Apparatus	Details			
	Model	Accuracy	Serial No.	Certificate No.
1. 120 KVA AC Power Supply	BL120	According IEEE112	05036	-
2. Digital Power Analyzer	6530	V. < ±0.2% of fsc A. < ±0.2% of fsc	1158-0400	EL-0220/01
3. Dynamometer 3HP- 20 HP	Dyne System	< ±0.2% of fsc	SN.2000439	164-3/2545
4. Resistance Meter	2318	± 0.1% ± 1 digit	1.0752001	EL-0221/01
5. Digital Temperature Measuring Ins.	NI 4351	System error ± 1.5 °C	00300375	02/0033

Induction motor efficiency method : IEEE-112 Method B

IEEE-112 method B is a motor efficiency testing based on a comparison of input and output to determine an amount of different losses occurred in the tested motor. Details of this standard are explained in this section.

1. Calculate Total Loss from an Input and Output measured by the test apparatus using the equation:

$$\text{Total Loss} = \text{Input} - \text{Output} \tag{3.1}$$

2. Divide calculated Total Loss into Stator I^2R Loss, Rotor I^2R Loss, Core Loss, Friction and Windage Loss , and Stray-Load Loss. For Method B, Stray-Load Loss is calculated by subtracting Total Loss with other losses taking into account an effect of torque and other factors.
3. Rated Load Temperature test: a motor sample which is connected to a dynamometer will be operated at rated load which is normally at specified 100% and wait until the temperatures are stable before proceeding to the next step.
4. Loaded motor test: different desired test loads from dynomometer are applied to a test motor while the corresponding current and voltage are measured in a shortest time possible to avoid a temperature effect. A compensation factor from a dynamometer should also be taken into account.

5. No-load motor test: a test motor is operated with no load until temperature and input parameters reach stable state. The corresponding current is measured in this condition for a calculation of core loss and friction & windage loss.
6. Determination of core loss and friction & windage loss

   - Measure input power or loss in motor under no-load condition. Then, after excluding a stator I^2R loss from the measured value, the remaining value is a summation of friction & windage loss and core loss

   - Power input minus the stator I^2R loss is plotted vs. voltage, and the curve so obtained is extended to zero voltage. The intercept with zero voltage axis is the friction and windage loss. The intercept may be determined more accurately if the input minus stator I^2R loss is plotted against the voltage squared for values in the lower voltage range. An example is the dashed curve shown in Figure 3.5.

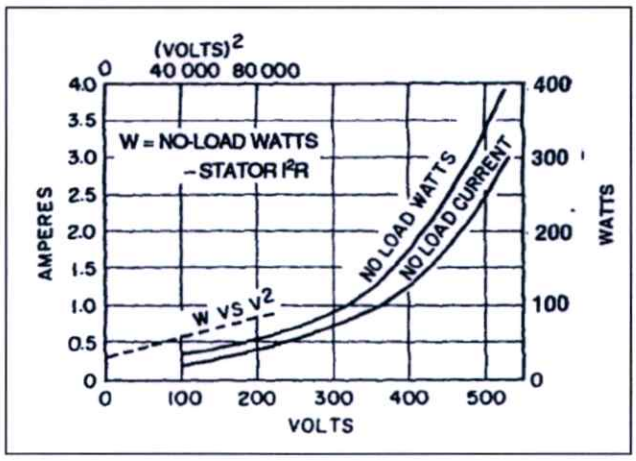

Figure 3.5 Example of Friction and Windage Loss determination

(ref: IEEE 112-1996 Standard test procedure for motor and generators)

- Core loss can be separated from friction & windage loss by measuring voltage, current, and power input at rated frequency from 125% of rated voltage, by decreasing voltage until the current increase.

- The core loss at no load and rated voltage is obtained by subtracting the value of friction and windage loss from the sum of the friction, windage loss, and core loss

7. Calculation of stator I^2R loss: For 3-phase motor, this loss can be calculated in Watt by equation (3.2)

$$\text{Stator } I^2R \text{ Loss} = 1.5\ I^2R \qquad (3.2)$$

where I is rms current between lines at specific working load

R is direct current (DC) resistance between lines at specific temperature

8. Calculation of rotor I^2R loss: Including brush-contact losses for wound-rotor machine, slip has to be taken into account by following equation.

$$\text{Rotor } I^2R \text{ Loss} = (\text{Measured Stator Input Power} - \text{Stator } I^2R \text{ Loss} - \text{Core Loss}) \times \text{Slip} \qquad (3.3)$$

3.1.3 Induction Motor: Temperature Measurement

In addition to a motor efficiency test explained in previous section, external and internal temperature of motor was measured throughout the test. Two different methods were employed in this study to observe and record the change in temperature: a thermal infrared camera (Figure 3.6) and type-K NiCr-NiAl thermocouples.

Figure 3.6 Thermal infrered camera (Flir Systems S65)

Both types of apparatuses were employed simultaneously during the test since each one had their own limitation. For thermocouple, there was a complexity in attaching probes in the measurement area. If the probes were not attached securely to the surface of interest, there might be a significant error in a reading. On the other hand, a thermal camera could not detect a surface temperature of those components with an obstructed view. This made a measurement by a thermal camera of internal motor components, such as rotor and stator, impossible. Additionally, there might also be a discrepancy due to a camera position or certain surfaces, which could have specific effect with an infrared. Therefore, by using a combination of two apparatuses, any possible error due to limitations of each method was minimized.

3.1.3.1 Temperature Measurement: Thermal Infrared Camera

This study was selected thermal infrared camera as Flir systems S65. This model was a long wave, focal plain array camera that was capable of temperature measurement. The camera specifications were accuracy at +/- 2°C, temperature range -40 to 1500 °C, thermal sensitivity < 0.01 at 30 °C and emissivity adjustment 0.01-1.00.

In order to measure the motor temperature during the motor operated, the infrared camera was attached on a stable camera tripod. The distance from the specimen to the camera was set to 2 m. The view on camera is perpendicular to the side surface of motor which the left border of frame is near the motor shaft. Whole motor body was arranged on the center frame with more than 85 % of frame area.

3.1.3.2 Temperature Measurement: Thermocouple

A thermocouple is a temperature-reading probe, which works under a principal of a change in electrical property of two different, contacting metals when subjected to a change in temperature. Thermocouple is categorized by type of combined metals at the probe, which would give a different reading sensitivity at different ranges of temperature. Since a temperature range of interest for this work was between a room temperature of 25 °C up to 250 °C, a thermocouple type-K was chosen. Technical specifications of type-K thermocouple used in this work are given in Table 3.3 below.

Table 3.3 Technical specifications of type-K thermocouple employed in this work

Coupled meterials	Nickel-Chromium withNickel-Aluminum
Temperature range	-200 to1250 °C
Limit of error	Standard: 2.2 °C or 0.75% at higher than 0 °C 2.2 °C or 2.0% at lower than 0 °C Special : 1.1 °C or 0.4 %
Suggestion, bar wire environment	Clean oxidizing and inert ; Limited use in vacuum or reducing ; Wide Temperature range ; Most popular calibration
Reference junction	32 °F

In order to observe a temperature variation during the motor test, there were four different areas that were attached with a set of thermocouples: housing surface, stator core surface, copper wiring, and inside stator core. The details of thermocouple attachment in each area are given in a following section.

- **Housing Surface: Temperature Meaurement**

Since a material of motor housing was a cast iron, which typically had a rough surface finish, as well as there were an anti-corrosion coating and some oil stains on the surface, the first step was to clean up and scrape all the coatings off the interested section of the housing surface with a sandpaper or metal file. Then, an aluminum adhesive paper with special strength and high temperature resistance was used to attach the thermocouple probe securely to the prepared housing surface as shown in Figure 3.7.

Figure 3.7 Thermocouples attachment on motor housing surface

- **Stator Core Surface: Temperature Measurement**

Since a stator was an internal component, small parts of motor housing was drilled to allow an access for thermocouples to a stator core. Furthermore, as a stator core had an overall shape of a cylinder, front and rear faces of stator core were flat. Hence, it was convenient to prepare the surface for thermocouple installation using aluminum adhesive papers. After cleaning all oil stains off the measurement locations, 4 thermocouples were installed on each front and rear face of the stator core at roughly 90 degree apart as shown in Figure 3.8.

Probe attachment on Stator

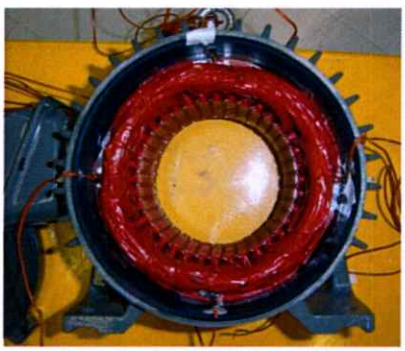

Overall measurement locations on Stator

Figure 3.8 Thermocouple attachment on stator core surface

- **Copper Wiring: Temperature Measurement**

Copper wires were wound around a stator core inside a housing. Therefore, holes were introduced on a housing to allow an access for thermocouples in similar way to that of stator core surface. The probes were placed amongst the copper wirings coming out at the front and rear end of a stator. An epoxy resin was used to secure the probes in positions without damaging an insulation coating on copper wires in order to prevent potential damage to equipment and operators.

- **Stator Core (Inside): Temperature Measurement**

Temperature measurement of position inside a metal bulk of stator core was done by making a small hole, roughly a size of thermocouple probe, on a stator core with a desired depth from the stator surface. A thermocouple was then slotted through with its probe just

about touching a bottom of the hole. An epoxy resin was then applied to prevent a thermocouple movement during the test as shown in Figure 3.9.

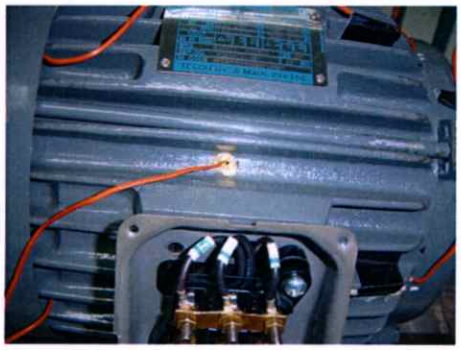

Epoxy resin holding thermocouple wire to housing

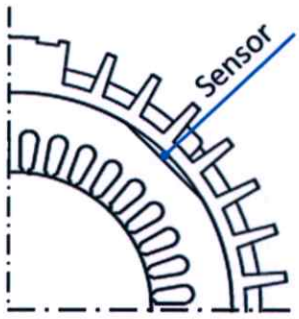

Thermocouple probe installation into stator core

Figure 3.9 Thermocouple installation inside a stator core

3.1.4 Material Properties Testing for Computational Analysis

In order to perform a computational analysis on a heat transfer phenomena in an induction motor involving heat conduction and heat convection mechanisms, following material properties of both solid objects and coolant were required:

- Thermal conductivity
- Density
- Specific heat capacity

Generally, when considering a cross-sectional view of an induction motor, a relationship between a temperature distribution and a radial distance away from a center of a driving shaft through rotor, stator, and housing to a surrounding air could be displayed as shown in Figure 3.10.

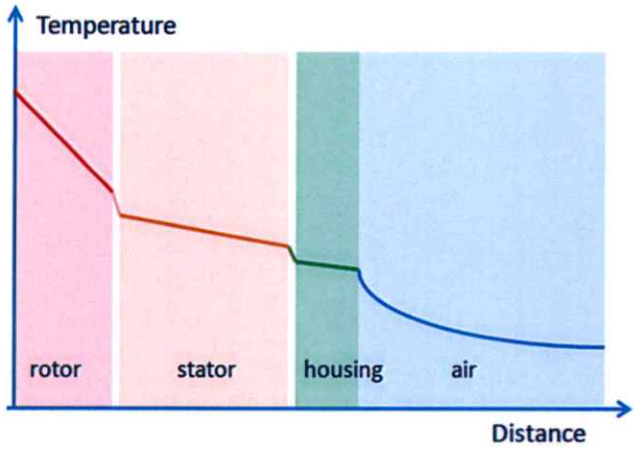

Figure 3.10 Radial temperature distribution of electric motor during operation againstdistance from driving shaft via housing to a surrounding air

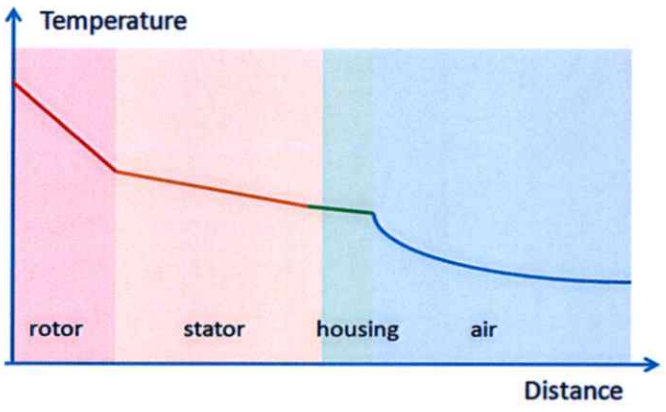

Figure 3.11 Radial temperature distribution of electric motor during operation against distance from driving shaft via housing to a surrounding air (ignoring contact surface property)

However, by taking into account only thermal conductivity of rotor, stator, and housing, the resulting radial temperature distribution could be shown in Figure 3.11. The difference between this computed temperature and that from the actual case (Figure 3.10) could be seen and could be significant in some cases if the computational model could not appropriately predict the phenomena. A source of such difference came from an interface between each motor component. Depending on a physical contact condition between each component, a corresponding thermal conductivity might not be the same as those of surrounding materials. In other word, this property is known as Thermal contact resistance. In a computational model of an induction motor

used in this study, there were two main contact interfaces i.e. rotor-to-stator and stator-to-housing. An experimental setup regarding these interfaces will be later explained in this section.

3.1.4.1 Materials Property – Solid

Majority of solid objects considered in a computational analysis were motor components. The main ones directly related to heat transfer phenomena are shown in Figure 3.12 along with their respective materials.

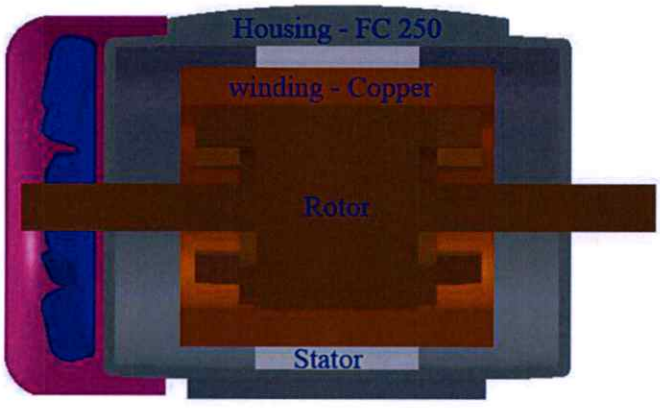

Figure 3.12 Induction motor components relating to heat transfer mechanism

In order to study a heat transfer phenomena on solid objects, two necessary materials properties were Specific heat capacity (C_p) and Thermal conductivity. The corresponding values for each motor component were obtained by means of a laboratory testing. Specimens from each relevant component were prepared and tested at National Metal and Materials Technology Center (MTEC) using following techniques:

- **Thermal constant analyzer (Hot disk TCA)**

This is a technique for determination of various thermal properties of materials such as conductivity, heat capacity, or thermal diffusivity. Related technical specifications of a test machine were:

  - Hot Disk, Thermal Constant Analyzer
  - Thermal conductivity range : 0.005 W/m.K to 500 W/m.K

- Reproducibility : thermal conductivity + 2%, thermal diffusivity + 5% and specific heat (per unit volume) + 7%
- Temperature range : room Temperature
- Sample size : diameter/thickness > 5 mm

- **Differential Scanning Calorimetry (DSC) & Differential Thermal Analysis (DTA)**

DSC and DTA are a technique that determines a temperature and quantity of heat that materials absorb or release when there is a change in physical or chemical property under a testing program of increasing or decreasing temperature. They are also used to study a chemical reaction or phase transformation of materials under changing temperature or time. List of testing includes:

- Melting Temperature or T_m
- Heat of Fusion or ΔH
- % Crystallinity in polymer
- Glass transition Temperature or T_g
- Crystallization Temperature or T_c
- Specific heat capacity or C_p
- Oxidative Induction Time or OIT
- Purity
- Crosslink reaction in thermosetting

The employed test machine was Perkin Elmer, DSC 7 with following technical specifications.

- Calorimetric precision: + 2%
- Temperature range : Room Temperature to 500 °C, with + 0.1 °C accuracy and precision

3.1.4.2 Material Property – Coolant

In case of a TEFC induction motor, a surrounding air is the main coolant and its appropriate properties could be found from any Thermodynamics textbook or a simulation software database.

For a new cooling system of a motor in which a liquid would be the main cooling medium instead of an air, the most important property was specific heat capacity (C_p),which was directly related to an amount of heat that a coolant could carry away in a convective heat transfer by the coolant. One of coolants of interest for this study was an industrial cooling oil. The chosen coolant was tested in similar fashion to those solid objects to determine its C_p. Moreover, by using a liquid in a cooling system, one needed to consider an additional presence of a pump and valves to regulate a coolant flow inside the whole system. As a result, other liquid properties, which were related to a functionality of a pump, had to be considered. Primarily, some necessary properties of a chosen cooling oil could be acquired from its manufacturer information site.

3.1.4.3 Thermal Contact Resistance

As mentioned earlier, in an induction motor, there were two main contact interfaces i.e. rotor-to-stator and stator-to-housing. These contacts are shown graphically in Figure 3.13.

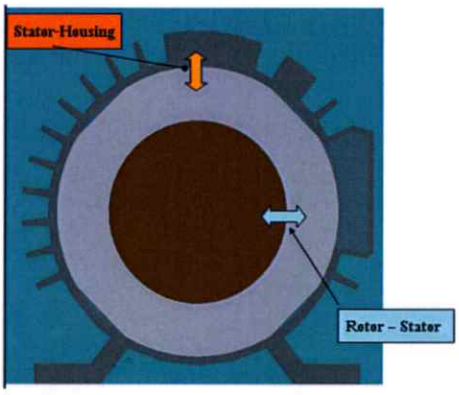

Figure 3.13 Thermal contact areas in an induction motor

In order to assign appropriate values of thermal contact resistance to a developed computational model, two separate experimental tests had been set up as explained below.

- **Stator – Housing**

To determine a thermal resistance of a contact between stator and housing, a controlled heat source was installed along an inner circumference of a stator. This heat source was to apply a controlled amount of heat to a housing through a stator in a radial direction. A temperature measurement was done on the outer surface of a housing. In addition, heat insulation was used to prevent a heat transfer in any undesirable direction as shown in Figure 3.14.

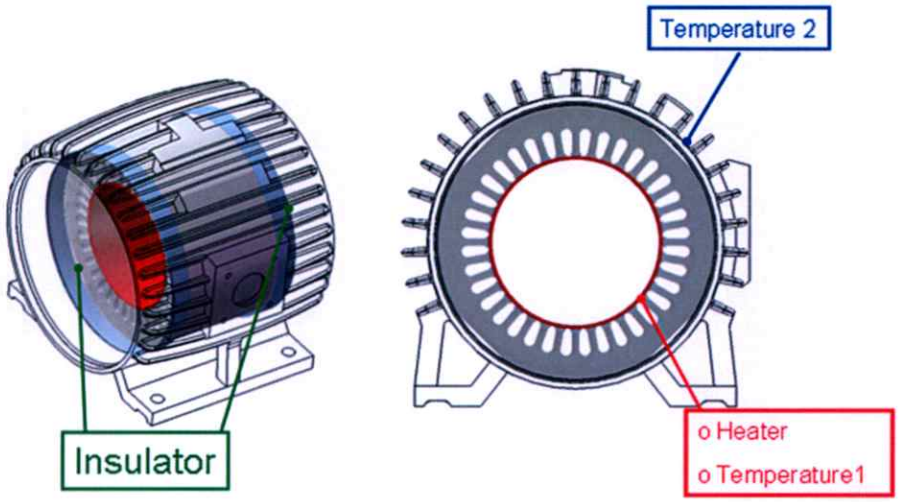

Figure 3.14 Schematic diagram of an experimental setup for a determination of thermal contact resistance for stator-to-housing contact

Below are detailed explanations of the involved test procedures to determine a thermal contact resistance for stator-to-housing contact.

- Assembled a stator core without a copper wiring into a motor housing around the same position/orientation as in a normal assembly.
- Installed a controllable heat source, i.e. an electronic heater, to an inner curved surface of a stator core and placed a temperature sensor on an outer surface of a housing as shown in Figure 3.15.

Figure 3.15 Test apparatuses confuguration in an experiment to determine thermal contact resistance for stator-to-housing contact

- Position a thermal infrared camera to enable a temperature measurement for all housing, stator, and heater or in the same view as that shown in Figure 3.15.
- Measured a room temperature before starting the test.
- Started applying a heat via an electronic heater by setting up a fixed target temperature. Checked the temperature by a thermal camera and thermocouple sensors while the overall temperature of the assembly rose steadily. Recorded all the corresponding temperatures once the temperature of all the components reached steady values.
- Determine an initial thermal resistance network of a whole system using assumptions that all heat transfer occurred in radial direction only and that heat transfer properties of all materials were isotropic. Then, at a thermal steady state, the thermal network of the test configuration could be represented as shown in Figure 3.16.

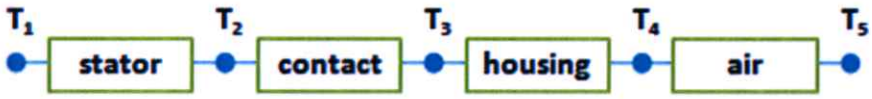

Figure 3.16 One-dimensional thermal network in a radial direction of an experiment to determine a Thermal Contact Resistance between stator and housing

From the above model, under a thermal steady state, it could be deduced that

$$Q = \frac{(T_2 - T_3)}{R_{stator-housing}} \tag{3.4}$$

where $R_{stator\text{-}housing}$ is a thermal contact resistance between stator and housing

With a known heat source (electronic heater) and a measured temperature difference by temperature sensors, a corresponding resistance could be determined. After calculating a thermal contact resistance using the above equation, the obtained value was used further in a three-dimensional heat transfer analysis. In this analysis, a 3-D computational model of a stator-housing assembly similar to that shown in Figure 3.14 was created. This previously calculated thermal contact resistance using Equation 3.4 was assigned to the relevant contact areas in the model as one of the boundary conditions. The analyzed results were then compared to those from the experiment. The resulting difference between two sets of results was then used as a guideline to adjust the thermal contact resistance that was used in the simulation until a good agreement could be observed between analysis and experiment. The final appropriate value of thermal contact resistance would be further employed in a heat transfer analysis of an induction motor.

- **Rotor - Stator**

Since a rotor would be in a constant movement during the operation, it was difficult to insert any temperature measuring equipment as well as a controlled heat source on a rotor. It was decided to mainly use a computational analysis to determine a relevant contact resistance. However, an experiment was performed to roughly approximate a thermal contact resistance between rotor and stator. Below are detailed explanations of the involved test procedures.

- Prepared a stator and rotor specimen for thermocouple installation by drilling blind holes into specimens using a milling machine as shown in Figure 3.18. As shown in Figure 3.17, the thermocouple locations were:
  - Heater surface (Heater1)
  - Contact surface between heater and rotor (Heater2)
  - Rotor outer surface (Outer Rotor)
  - Inner surface of stator (Inner stator)
  - Near contact between rotor and stator (Outer surface rotor)
  - Outer surface of stator (Outer surface stator)

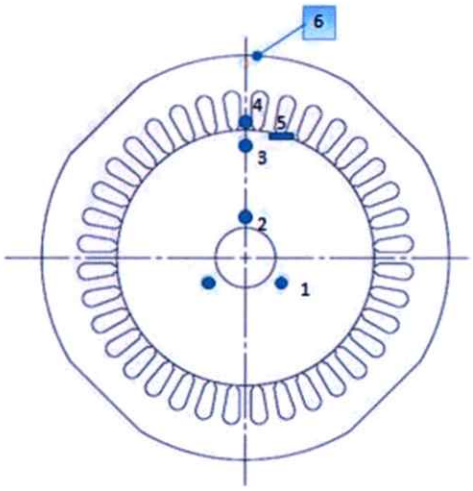

Figure 3.17 Thermocouple positioning on stator and rotor specimen in rotor-stator thermal contact resistance experiment

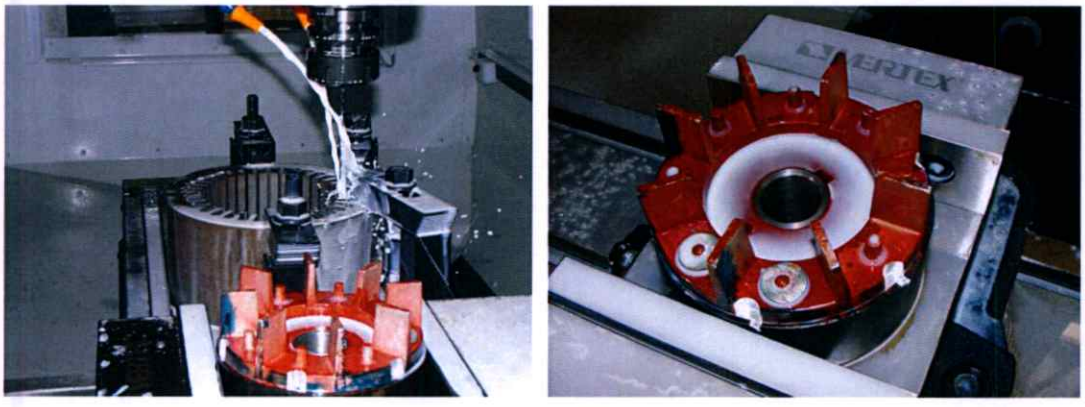

Figure 3.18 Specimens preparation for rotor-stator thermal contact resistance experiment

- Inserted a cylindrical-shaped heater into a center of rotor to replicate an actual heat source when a motor was operating normally. Connected all the thermocouples at the designed locations shown in Figure 3.17 to data logger equipment so that all the temperature changes could be recorded throughout the test. The overall configuration is shown in Figure 3.19.

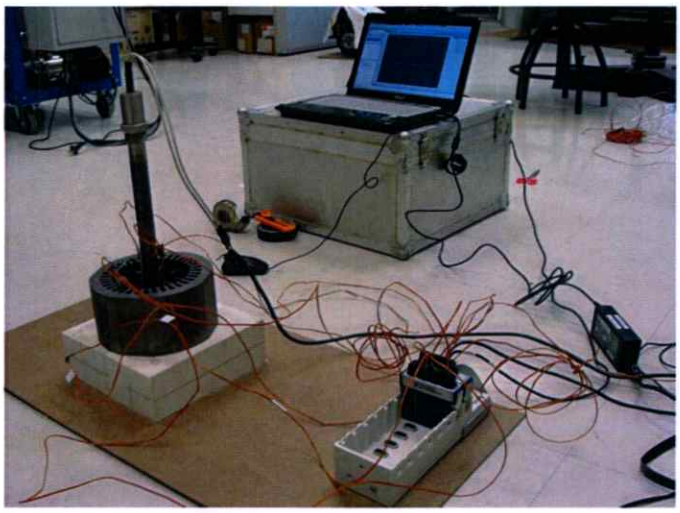

Figure 3.19 An experimental configuration to determine of a thermal contact resistance between rotor and stator

- Measured corresponding temperatures resulting from a heater located at the center of rotor until a thermal stability was observed at all 6 thermocouple positions.
- Determine an initial thermal resistance network of a whole system using assumptions that all heat transfer occurred in radial direction only and that heat transfer properties of all materials were isotropic. Then, at a thermal steady state, the thermal network of the test configuration could be represented as shown in Figure 3.20.

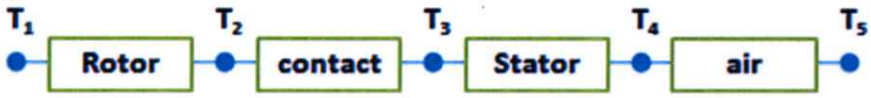

Figure 3.20 One-dimensional thermal network in a radial direction of an experiment to determine a Thermal Contact Resistance between rotor and stator

Similar to the case of stator-housing contact, following equation could be deduced under a thermal steady state.

$$Q = \frac{(T_2 - T_3)}{R_{rotor-stator}} \tag{3.5}$$

With a known heat source (electronic heater) and a measured temperature difference by temperature sensors, a corresponding resistance could be determined. After calculating a thermal contact resistance using the above equation, the obtained value was used further in a three-dimensional heat transfer analysis. In this analysis, a 3-D computational model of a stator-housing assembly similar to that shown in Figure 3.19 was created. This previously calculated thermal contact resistance using Equation 3.5 was assigned to the relevant contact areas in the model as one of the boundary conditions. The analyzed results were then compared to those from the experiment. The resulting difference between two sets of results was then used as a guideline to adjust the thermal contact resistance that was used in the simulation until a good agreement could be observed between analysis and experiment. The final appropriate value of thermal contact resistance would be further employed in a heat transfer analysis of an induction motor.

3.1.4.4 Air Velocity Measurement in TEFC Induction Motor

Apart from all the temperature measurements on different parts of the induction motor as explained in previous sections, another experiment was carried out to measure an air velocity around the studied TEFC induction motor. This was to verify a computational result of an air flow analysis resulting from a rotation of a fan. A hot-wire anemometer shown in Figure 3.21 was used in this experiment.

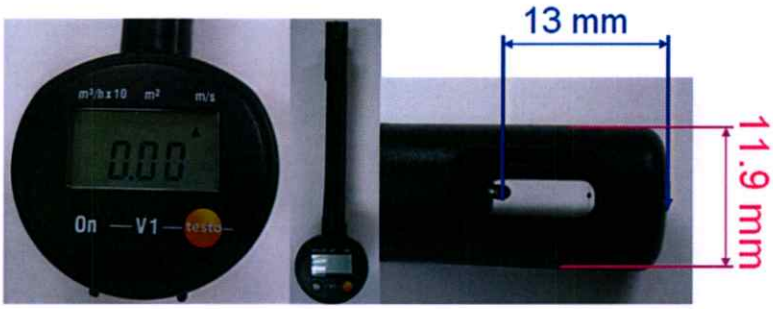

Figure 3.21 Air velocity measuring equipment: Hot-wire anemometer

In order to verify a suitability of the developed computer model, a comparison between a measured and analyzed velocity profile along an axis direction of a motor from a rear end of the housing to the front end was carried out. For the experimental results, measurements were made along a total of 30 gaps between each cooling fin on the housing. The first measurement was made at the air outlet from the fan cover before it was repeated at every 5 mm towards the front of motor until the end of fin as shown in Figure 3.22.

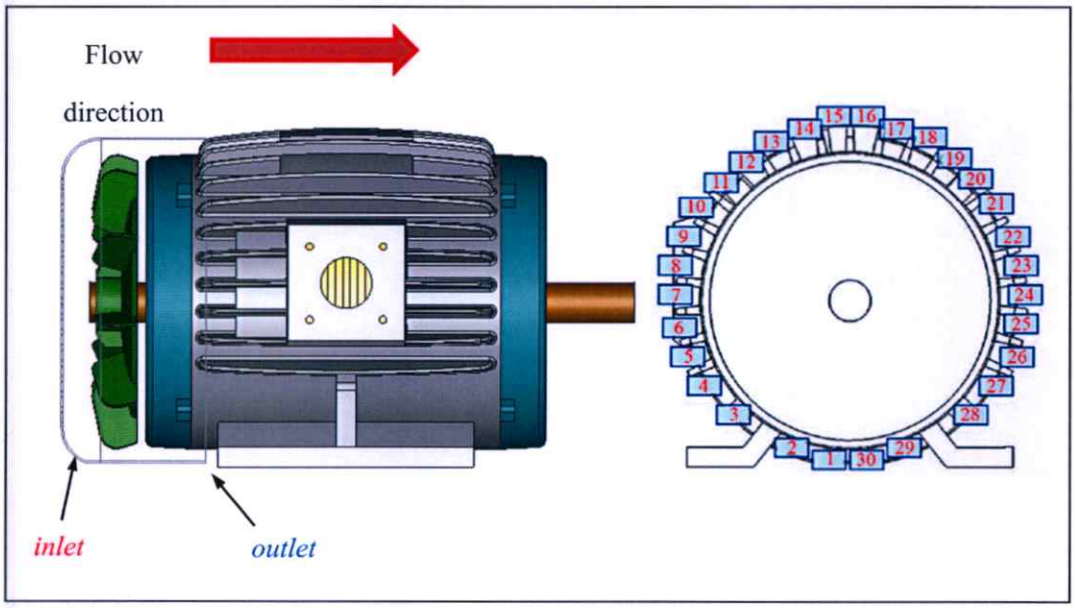

Figure 3.22 An air flow direction from a rotation of a fan and velocity measurement positions between fins on housing of an induction motor

Figure 3.23 Air velocity measurement method

In order to obtain the results from the analysis, it was necessary to allocate specific locations in the computation model that the velocity results would be displayed from. Thus, it was logical to pick the location where the probe of anemometer would be in an actual situation. From Figure 3.23, it can be seen that when measuring the air velocity, the tip of the anemometer was put as close to a surface of housing as possible. As a result, the probe would be approximately 13 mm away from the housing surface during the test (Figure 3.21). Therefore, it was specified in the analysis to display the calculated air velocity along a position that was 13 mm higher from the housing surface for computational results verification.

3.2 Analytical Procedures: Heat Transfer Analysis of TEFC Induction Motor

3.2.1 Motor CAD Model Preparation

The main induction motor components that were necessary for computational analysis were comprised of total of 6 internal and external parts as shown in Figure 3.24.

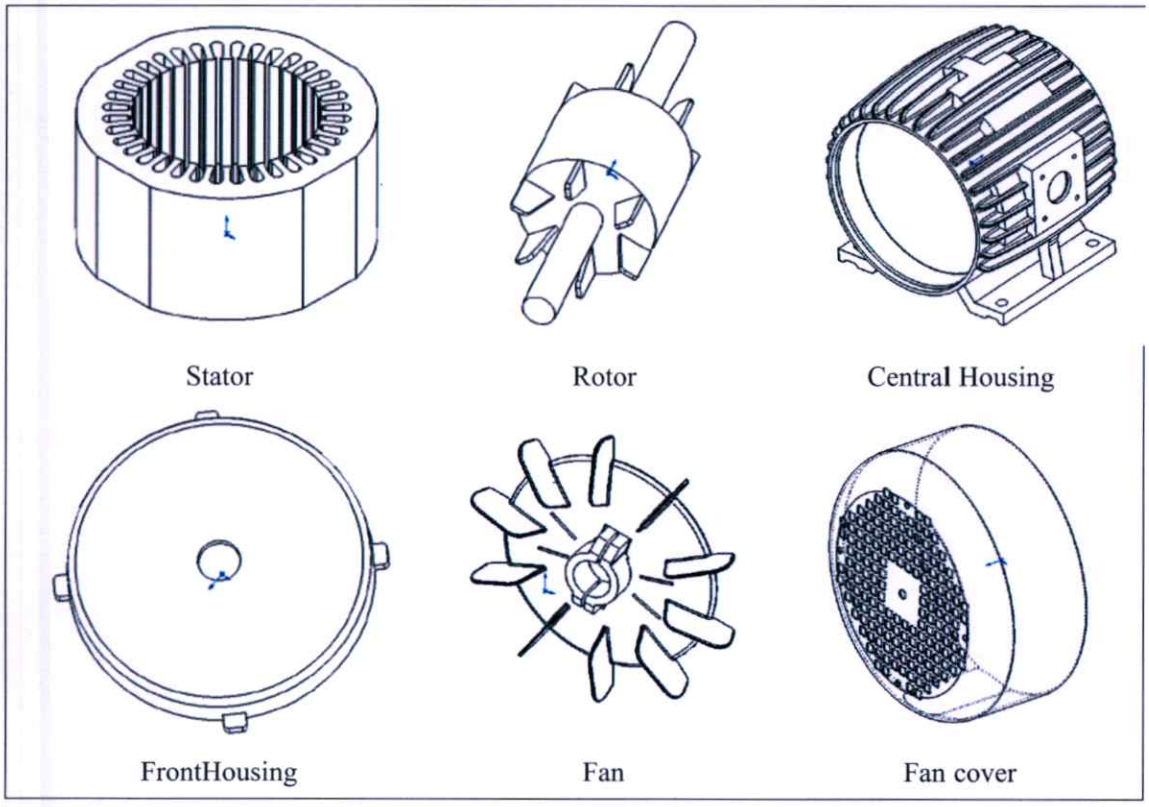

Figure 3.24 CAD models of induction motor parts necessary for computaional analysis

For stator, rotor, housing, and fan cover part, the relevant computational models were created in CAD software using manual measurements as a reference. On the other hand, a fan model o was created by means of 3D scanning an actual part such that all the relevant profiles of fan and blades were accurately captured onto CAD model.

3.2.2 Air Domain Preparation

In a heat transfer analysis of TEFC induction motor, there were two different parts of air that needed to be considered in a fluid flow analysis i.e. a surrounding air outside a motor housing (external) and an air space inside a motor (internal). In each part, a solid CAD model was

created to occupy a volume where an air space would be in an actual motor such that it could be assigned as an air domain in the analysis. Nonetheless, different analyses could require different considerations of a flow pattern. In some cases, only the external air domain was needed, while both domains were necessary in others. Details of external and internal air domains preparation are given in the next sections.

3.2.2.1 External Air Domain Preparation

Since all the motor tests were carried out in a 10 m long air-conditioned laboratory, theoretically a corresponding external air domain should be prepared with the same overall size. However, in practice, performing an analysis with a large domain would require a large computational resource and would be very time-consuming. Therefore, an overall scale of created air domain had to be reduced to allow a reasonable analytical time. Basically, all the boundaries of the air domain were placed at a distance away from the test motor by approximately 4 times of the test motor size. However, as the motor was located on a flat platform during the test, a bottom boundary of the air domain was placed right next to the motor. The final shape of the external air domain was a semi-cylindrical as shown in Figure 3.25. Additionally, front and rear faces, and a curved surface of the domain were allocated as an "open" boundary, which effectively remained at an atmospheric pressure while allowing a surrounding air to flow freely in and out of the boundary in the direction perpendicular to the boundary surfaces. Such boundary setting would not have a significant effect on airflow around the induction motor.

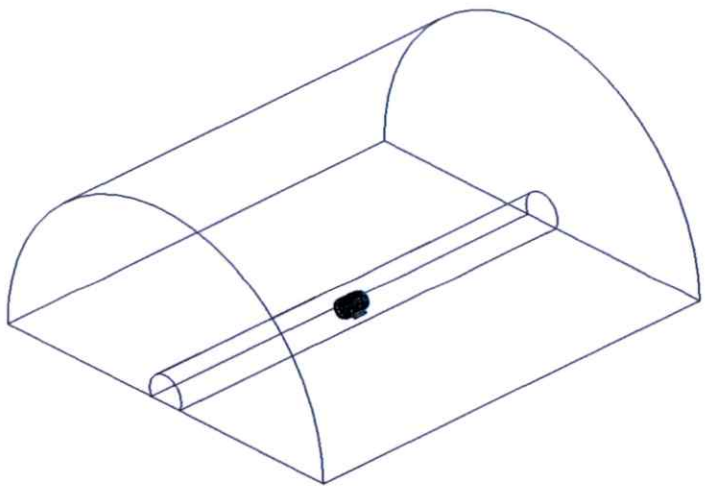

Figure 3.25 A solid model using as an external air domain in the motor analysis

Furthermore, the external air domain explained above was divided further into another smaller domain, a sub-domain, which was employed in a flow analysis concerning a rotation of a fan at the rear section of the motor. This sub-domain had to cover the whole vicinity of the fan while also having a symmetrical shape in the rotating direction as shown in Figure 3.26. As for an analysis, the sub-domain was assigned as a Moving Frame Reference (MFR) to take into account a fan rotation. Additionally, an interface interaction between the domain and sub-domain had to be defined such that a conservation of momentum of airflow between the two domains was satisfied.

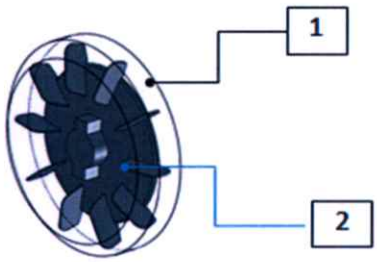

Figure 3.26 Solid model using as external air sub-domain to take into account an effect of fan rotation (1) Air sub-domain and (2) Fan model

3.2.2.2 Internal Air Domain Preparation

Within a confined space inside a motor housing, there were generally a rotor and a stator and an air space. During a motor operation, a rotor would be rotating around its axis leading to a movement of end fins on both sides of rotor face to create airflow inside the housing. Hence, in similar fashion to that of external air domain, an internal air domain was divided into three sub-domains e.g. two domains covering the fin areas on both ends of rotor and another representing the rest of air space inside the housing. An employed internal air domain is displayed in Figure 3.27.

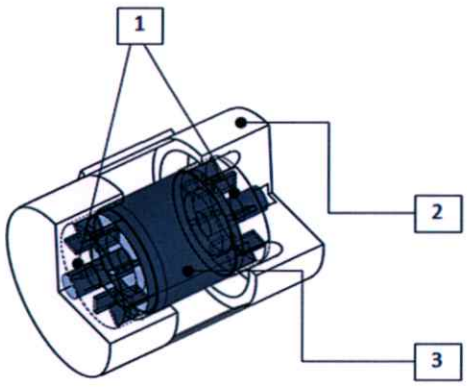

Figure 3.27 Solid model using as internal air sub-domains to take into account an effect of rotor rotation (1) Air sub-domains around rotor fins, (2) Remaining internal air space domain and (3) Rotor model

Similar to the motor fan case explained in previous section, the domains around the rotor fins were assigned as a Moving Frame Reference (MFR) to take into account fins rotation during a motor operation. Additionally, all domain interface interaction shad been defined to allow a continuous transfer of air velocity vectors resulting from a rotor rotation between all three sub-domains under a conservation of momentum. All air velocities calculated here would then be used further in an analysis to study a heat transfer behavior inside a TEFC induction motor during operation.

3.3 Mesh Models Preparation for Heat Transfer Analysis

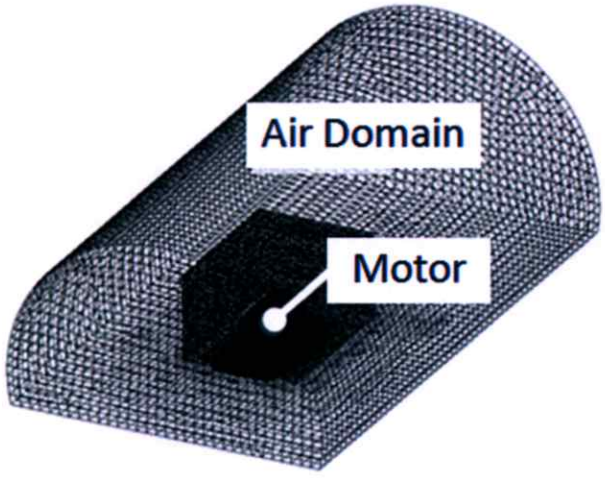

Figure 3.28 Overall 3D mesh models for heat transfer analysis

After all relevant solid CAD models had been prepared as explained in previous sections, the next step was to convert these models into mesh models that could be used in computational fluid dynamics (CFD) and heat transfer analysis as shown in Figure 3.28. Especially for the CFD analysis, chosen mesh size and distribution could have a significant impact on the obtained results due to a non-linear nature of the analysis. This was particularly prominent in areas where there were changes in geometry profiles or where the fluid came to contact with other objects. As a result, fine meshes had to be used to ensure suitable analytical results. However, using fine meshes in all calculated domains would result in a very large amount of Degree of Freedom (DOF) that could not be efficiently handled by existing computational resources. Therefore, fine meshes were assigned at only necessary locations in order to limit a total number of meshes and to effectively manage an available computational resource. The details of mesh set up at these particular areas are given below.

3.3.1 Mesh Preparation for Motor Fan and Nearby Air

Choosing an appropriate mesh type around the area of motor fan and nearby air was important because the resulting airflow from fan rotation would be used in further heat transfer analysis. Principally, different approaches were used in this study depending on the method

chosen to take into account the rotation of solid sub-domains i.e. Immerse Solid or Moving Frame Reference (MFR). Each method had different purpose in an analysis. Immerse Solid had an advantage of being relatively simpler to prepare but did not allow a heat transfer calculation between solid models. In cases that heat transfer had to be considered together with a rotation, MFR had to be considered. For the motor fan simulation, Immerse Solid was chosen.

In preparation for the fan rotation simulation by Immerse Solid approach, the solid model of the fan was located in an overlap with the air domain under the main condition that the whole of solid domain was to be totally submerged or "immersed" within a fluid (air) domain throughout. Another important condition was that the mesh size of both solid and fluid domains had to be identical or as close as possible. The final appearance of meshed model in the motor fan area is shown in Figure 3.29.

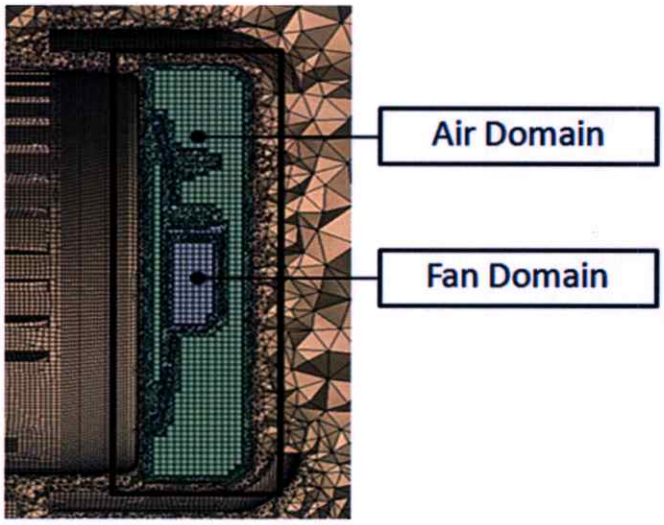

Figure 3.29 The final appearance of meshed model in the motor fan area with equal mesh size between solid (fan) and fluid (air) domains

3.3.2 Mesh Preparation for Boundary Layer Areas

Fine meshes were employed in those areas near solid surfaces such as fan, housing, and fan cover whereas coarser meshes were used in other remote areas as shown in Figure 3.30. This was due to the effect of air viscosity near the solid surface, giving rise to a non-linear behavior and a turbulence flow pattern. These areas are also known as "Boundary Layer" which requires fine mesh details for a flow analysis to adequately predict the flow behavior.

Additionally, an "Inflation" command was utilized to assist the mesh preparation in the boundary layer areas. An example of such mesh layout is shown in Figure 3.31.

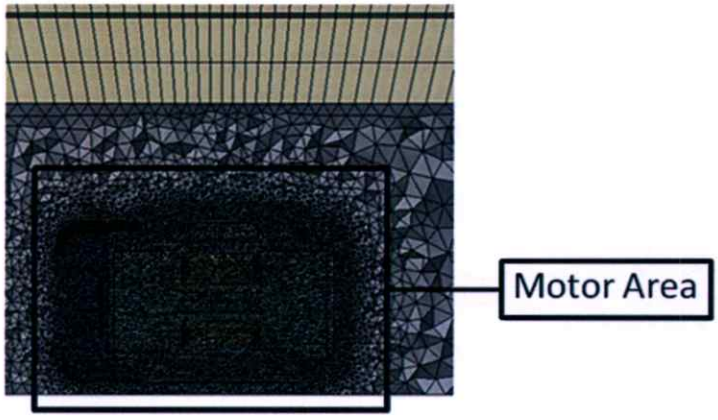

Figure 3.30 Mesh distribution pattern: denser distribution with finer meshes in vicinity of a motor

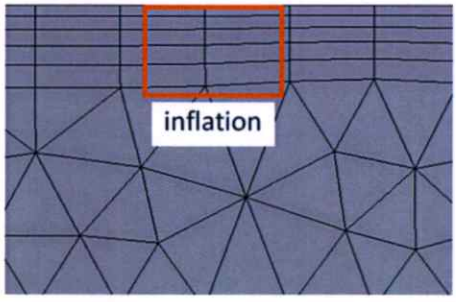

Figure 3.31 Mesh distribution pattern using "Inflation" command

3.3.3 Mesh Preparation for Narrow Air Gap

Examples of a narrow air gap area were gaps formed between a motor housing and a fan cover. Extra fine meshes were used in these areas. More importantly, there should have been at least 3 meshes across the gap between a housing and a fan cover to avoid the effect of boundary layer that would have made the air velocity along the air gap dropped to zero. For this study, around 4-5 meshes were assigned across all the narrow air gaps such as those displayed in Figure 3.32.

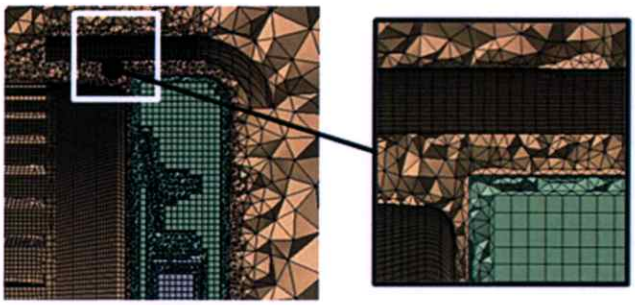

Figure 3.32 Mesh pattern along the narrow air gap e.g. air exit formed by fan cover and housing

3.3.4 Mesh Preparation for Rotor

Majority of airflows inside a motor were a result of a rotation of rotor with fins along both ends. As rotor rotated, there was also a heat transfer taking place between a rotor and a surrounding air inside the motor. Thus, the analysis model was prepared using the MFR approach which could handle both rotational movement and heat transfer simultaneously as explained in previous section.

In preparation for the MFR analysis model, sub-domains of air were made in the vicinity of rotor fins with a symmetrical shape in a rotating direction. Furthermore, a partial volume of this sub-domain with the exact shape of the rotor fins was subtracted from each sub-domain such that the solid model of rotor with fins could fit perfectly with these sub-domains. Then, when assigning a mesh, it was necessary that the nodes along the interface between two domains, solid (rotor) and fluid (air), had to be positioned at the exact location on both domains to minimize any potential error in the calculation.

3.4 Boundary Conditions for Induction Motor Heat Transfer Simulation

After appropriate mesh models were prepared as explained in a previous section, several relevant boundary conditions needed to be applied to the whole model in order to carry out the required computational analysis. It can be from the previous sections that the computational model could basically be divided into several domains of solids and fluid. The solid domains were mainly categorized by the main components of the induction motor while the fluid or air domains could be separated by the details of the analysis. The following sections will explain the boundary conditions used in this study for flow and heat transfer analysis of an induction motor.

3.4.1 External Air Domain

The physical properties of air for the external air domain which covered the volume outside the motor housing including fan and its cover are given in Table 3.4.

Table 3.4 Physical properties of air

Properties	Value
Density(kg/m^3)	1.225
Specific heat : C_p (j/kg-k)	1006.43
Thermal Conductivity (w/m-K)	0.0242
Viscosity (kg/m-s)	1.7894×10^{-5}

A viscous flow was considered for the flow analysis with a k-ε turbulence model, which was generally chosen for the turbulence flow analysis with low degree of gradient and vortex circulation. Additionally, a "Scalable" function was assigned to the boundary layer areas for extra accuracy in the flow analysis in case there was any unexpected high velocity gradient along the solid surface.

In order to carry out the heat transfer analysis between the air and the motor housing, the interface between two domains was set as "Conservative Interface Flux" which would allow the heat to travel between the two domains under the conditions of conservation of energy.

Considering the outside shape of the external air domain, there were four boundaries, which defined the overall analysis frame of the model as discussed in previous section. The boundary conditions applied to each boundary are shown in Figure 3.33.

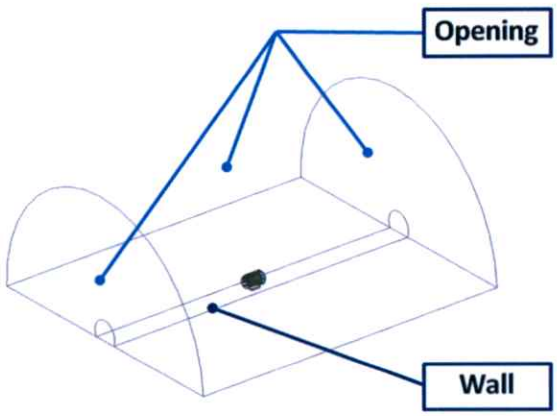

Figure 3.33 Boundary conditions applied to surface boundaries of external air domain

It could be seen from the image that only the bottom bounday of external air domain was assigned as "Wall". In further details, a "Non-slip" wall with a wall roughness of "Smooth wall" was defined together with the assumption of "Adiabatic" heat transfer property i.e. no heat transfer occurred. This was to reflect the actual testing conditions where the test motor was installed on a test platform. On the other hand, other domain boundaries represented the surrounding atmosphere in the motor testing laboratory. Therefore, they were allocated as an "open" boundary, which effectively remained at an atmospheric pressure while allowing a surrounding air to flow freely in and out of the boundary in the direction perpendicular to the boundary surfaces.

Another important boundary condition for external air domain was for the rotation of fan at the back of the motor. Since there was no need the resulting temperature distribution on the fan, only the fan rotational movement parameter was considered in the simulation with heat transfer left out. This led to the Immerse solid approach as explained in the mesh preparation section. The rotational speed of 1,450 RPM, which was the actual motor speed during operation, was assigned to the relevant air sub-domain in the analysis.

3.4.2 Internal Air Domain

As explained earlier, the internal air domain was comprised of three different domains connected together. There were two domains, covering the fin areas on both ends of rotor, which needed to take into account the rotation of rotor, while another domain, representing the rest of air

space inside the housing, was in connection with solid models of rotor, stator, copper winding, and inner surface of housing.

The physical properties of the air were the same as those used with the external air. Furthermore, viscous flow analysis coupled with a k-ε turbulence model was considered in all three domains.

For the calculation of rotor rotation, since there was a need to consider the heat transfer between rotor and surrounding air, the MFR approach was applied in the flow analysis as explained previously in the mesh preparation section. The two domains at both ends of rotor were given a rotational speed of 1,450 RPM. The interface parameter between the rotor and the air was chosen as "Frozen Rotor" which was suitable for a steady state analysis that consisted of large displacement away from the reference points. In addition, at the domain interface, meshing condition was chosen as "General Grid Interface" (GGI) to compensate the inconsistency in mesh distribution along the two domains.

3.4.3 Solid Domains

The main solid domains in this study were motor housing, rotor, stator, and copper wiring, with the last three also acting as heat sources. The corresponding heat values that were assigned to each relevant domain were taken from the experimental results obtained from the motor efficiency test according to IEEE-112 standard as previously explained in section 3.1.2. All the heat source values were given in unit of W/m^3 and could be categorized for each solid domain as shown in Table 3.5.

Table 3.5 Heat source specification

Domain	Relevant Motor Loss
Rotor	Rotor I^2R Loss + Friction Loss + Stray Loss
Stator	Core Loss +Stray Loss
Copper wiring	Copper I^2R Loss

All the heat transfer phenomena were controlled under the "Conservative Interface Flux". Moreover, there were two interfaces which required a special heat transfer property i.e.

rotor-to-stator and stator-to-housing contact interface. The corresponding thermal contact resistance, obtained from a combination of experimental and 3D analytical work as explained in section 3.1.4.3, was applied to each appropriate contact interface ($K.m^2/W$).

3.5 Conclusions

The research methodology , first are various experiments and measurements to obtain the data of TEFC motor such as the motor efficiency (IEEE-112 standard), the heat transfer properties of motor component, temperature measurement of motor both internal and external component, air flow velocity measurement. The obtained TEFC motor's data was analyzed and simulated to obtain the heat transfer and heat generation model of an multi-phases induction motor.

As following to the previous procedure, the heat transfer model of an multi-phases induction motor was obtained including with the internal behavior of motor such as the stator and rotor I^2R loss, core loss, stray loss, friction loss and the air flow circulation in motor housing caused by the rotation of rotor. The methodology also demonstrated the method to study the external behavior of motor such as the external air flow caused by the rotation of rear fan. The obtained heat transfer model of motor were applied to designed and optimized the liquid cooling system as discussed in next chapter.

CHAPTER 4

RESULTS

4.1 Totally Enclosed Fan Cooled Motor Efficiency Test and Temperature Measurement

The efficiency test was carried out on 2 different samples of TEFC motor with the same power rating and technical specifications. As explained in the previous chapter, the tests were operated by dynamometer at the motor testing center according to IEEE 112 standard. Furthermore, the corresponding temperature of the motor was measured by means of Infrared camera and thermo couple once the steady rated load, which was applied by the dynamometer, was reached.

4.1.1 Totally Enclosed Fan Cooled Motor Efficiency Test Results

The efficiency of an induction motor was measured according to IEEE standard 112 Method. There were 2 sets of results from 2 different samples of motor of the same model. Table 4.1 displays the comparison of efficiency results between the first and the second motor sample.

Table 4.1 Efficiency test results comparison between 1st and 2nd motor sample

Motor 1 : Average Cold Stator Winding Resistance Between Terminals (1) 2.6207 Ohms@ (2) 25.905°C Motor 2 : Average Cold Stator Winding Resistance Between Terminals (1) 2.6827 Ohms@ (2) 26.976°C							
Motor1: Rated load Heat Run Stator Winding Resistance Between Terminals (3) 3.6110 Ohms@ (4) 102.08 °C Ambient in °C (5) 25.525 Motor2: Rated load Heat Run Stator Winding Resistance Between Terminals (3) 3.3863 Ohms@ (4) 95.546 °C Ambient in °C (5) 25.067							
Item	**Descriptions (Motoring)**	**150%**		**125%**		**100%**	
		Motor1	**Motor2**	**Motor1**	**Motor2**	**Motor1**	**Motor2**
6	Ambient Temperature, in °C	25.691	25.124	25.778	25.127	25.749	25.084
7	(t_1)Stator Winding Temperature, in °C	80.812	91.704	80.793	91.784	80.804	92.271
8	Frequency, in (Hz)	50.006	50.003	50.003	50.003	50.006	50.006
9	Synchronous Speed, in r/min	1500.18	1500.09	1500.09	1500.09	1500.18	1500.18
10	Slip Speed, in r/min	150.18	186.09	117.09	135.09	87.18	97.18
11	Speed, in r/min	1350.0	1314.0	1383.0	1365.0	1413.0	1403.0
12	Line-to- Line Voltage, in V	379.71	379.84	380.18	380.46	380.59	380.96
13	Line Current, in A	12.86	14.536	10.546	11.216	8.501	8.835
14	Stator Power, in W	7317.65	8319.49	5978.46	6444.06	4752.44	5018.97

Table 4.1 Efficiency test results comparison between 1stand 2nd motor sample (Cont.)

Item	Descriptions (Motoring)	150%		125%		100%	
		Motor1	Motor2	Motor1	Motor2	Motor1	Motor2
15	Core Loss, in W	124.91	121.73	124.91	121.73	124.91	121.73
16	Stator I^2R Loss, in W, at (t_1) °C	787.18	1060.73	529.35	631.68	343.97	392.54
17	Power Across Air Gap, in W	6450.55	7137.03	5324.20	5690.65	4283.55	4504.70
18	Rotor I^2R	641.25	885.37	415.58	512.47	248.93	291.81
19	Friction and Winding Loss, in W	50.69	26.52	50.69	26.52	50.69	26.52
20	Total Conventional Loss, in W	1604.03	2094.35	1120.53	1292.40	768.50	832.60
21	Torque (Nm)	38.68	40.49	32.21	32.38	25.75	25.18
22	Dynamometer Correction (Nm)	1.14	1.54	1.14	1.54	1.14	1.54
23	Corrected Torque (Nm)	39.82	42.03	33.35	33.92	26.89	26.72
24	Shaft Power, in W	5629.33	5783.88	4829.87	4849.07	3978.73	3926.19
25	Apparent Total Loss, in W	1688.32	2535.61	1148.59	1594.99	773.71	1092.78
26	Stray-Load Loss, in W	84.29	441.26	28.06	302.59	5.21	260.18
	Correlation Factor = 0.932	Intercept=87.22		Slope = 0.089		Point Deleted = -	
27	Stator I^2R Loss, in W ,at (ts) °C	894.39	1073.06	601.48	638.86	390.83	396.41
28	Corrected Power Across Air Gap, in W	6298.35	7124.70	5252.07	5683.46	4236.70	4500.83
29	Corrected Slip, in r/min	160.37	188.31	125.04	136.67	93.10	98.16
30	Corrected Speed, in r/min	1339.81	1311.78	1375.05	1363.42	1407.08	1402.02
31	Rotor I^2R Loss, in W, at (ts) °C	673.28	894.37	437.79	517.79	262.91	294.51
32	Corrected Stray-Load Loss, in W	141.21	312.63	99.05	203.63	64.39	126.36
33	Corrected Total Loss, in W	1884.48	2428.31	1313.91	1508.54	893.73	965.53
34	Corrected Shaft Power, in W	5433.17	5891.18	4664.55	1935.52	3858.71	4053.44
35	Shaft Power, in hp	7.29	7.90	6.26	6.62	5.17	5.44
36	Efficiency, in %	74.25	70.81	78.02	76.59	81.19	80.76
37	Power Factor in %	86.52	87.00	86.09	87.19	84.81	86.09

The efficiency test was performed under various load conditions ranging from 25-150 % of the rated load. Table 4.2 shows the comparison of main motor characteristics between two motor samples at 25-150% of the rated load.

Table 4.2 Summary of main motor operating characteristics

Load, in % of rated	25		50		75		100		125		150	
	Motor1	Motor2	Motor1	Motor2	Motor1	Motor2	Motor1	Motor2	Motor1	Motor2	Motor1	Motor2
Load, in hp	1.25	1.25	2.50	2.50	3.75	3.75	5.00	5.00	6.25	6.25	7.50	7.50
Power Factor in %	49.50	48.98	70.52	71.45	80.23	80.96	84.39	85.15	85.81	86.72	86.09	86.65
Efficiency, in %	78.47	81.53	83.37	84.74	83.57	84.25	81.61	81.93	78.04	78.02	73.39	72.71
Speed, in r/min	1480	1483	1459	1461	1438	1438	1412	1413	1375	1377	1332	1329
Line Current, in A	3.64	3.55	4.82	4.67	6.33	6.21	8.21	8.09	10.54	10.42	13.40	13.42

The efficiency and loss measured from each sample of motor was plotted together against various load conditions as shown below in Figure 3.1 and Figure 4.2 respectively. The results of efficiency showed small difference between the samples at both lower and higher ends of tested load range. The maximum difference between efficiency results was about 3-5% observed at 120% rated load. On the other hand, results of the total loss showed an increasing difference as higher load was applied.

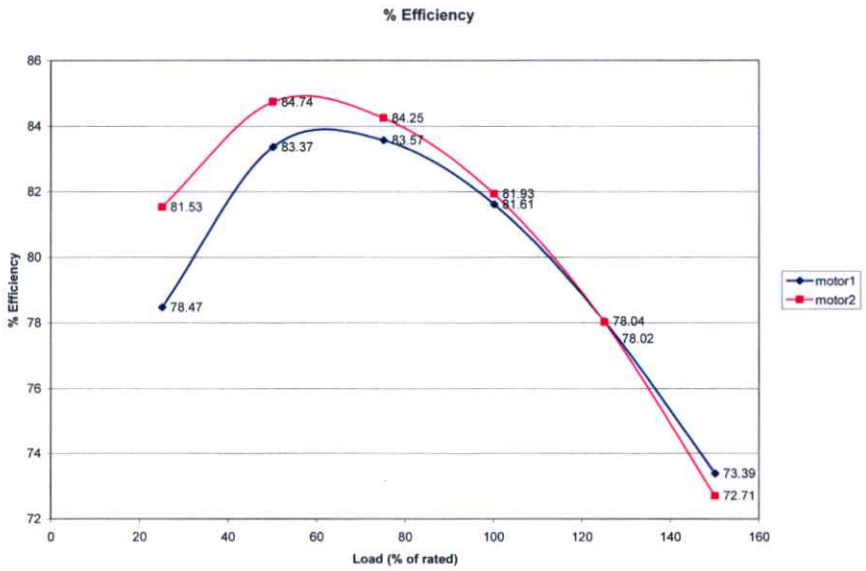

Figure 4.1 Comparison of efficiency results between 1st motor and 2nd motor

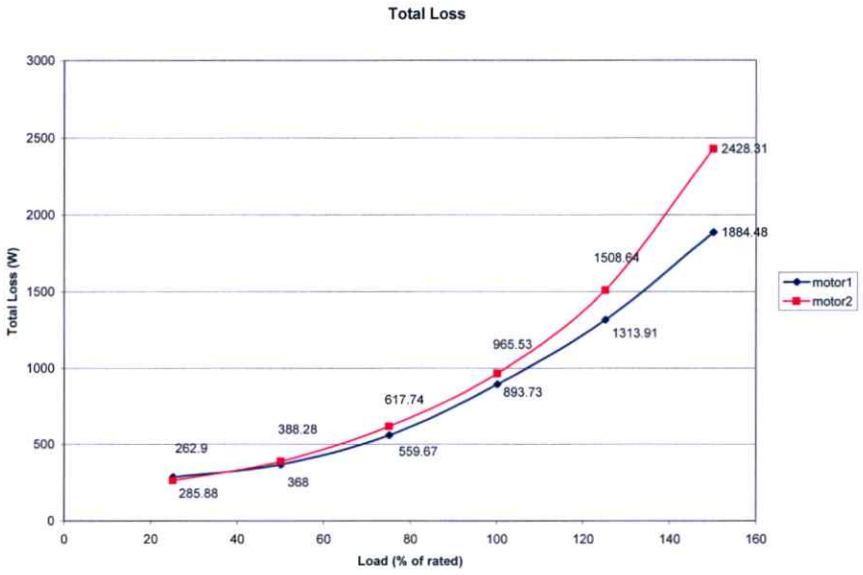

Figure 4.2 Comparison of measured total loss between 1st motor and 2nd motor

According to Figure 3.1, the maximum difference of efficiency between motor sample No.1 and No.2 was 3.06% at 25% rated load. However, in this study, the interesting range of work load was 100-150% of rated load. In this range, the maximum difference was 0.68% at the 150% rated load. This results can be determined those motor samples had a similarity in their efficiency.

Table 4.3 shows the details of losses occurred in each motor sample under the varied load. There were generally 5 types of loss occurred when the induction motor operated i.e. core loss, stator I^2R loss, rotor I^2R loss, friction and windage loss and stray loss.

Table 4.3 Type of losses in 1st motor and 2nd motor

Type of loss	150		125		100	
	Motor1	Motor2	Motor1	Motor2	Motor1	Motor2
Core loss + Stator I^2R Loss	1019.3	1195.33	726.39	760.59	512.74	518.14
Rotor I^2R Loss	641.25	885.37	415.58	512.47	248.93	291.81
Friction and Windage (W)	50.69	26.52	50.69	26.52	50.69	26.52
Stray Loss (W)	141.21	312.63	99.05	203.63	64.39	126.36

Regarding the difference observed in the total loss results in Figure 4.2, the relevant parameters of heat generation, which were determined from the results of efficiency test, were applied in the simulation by using the higher set of values from the measured results.

4.1.2 Temperature of Totally Enclosed Fan Cooled Motor

The external temperature of TEFC motor was measured by the infrared camera and thermocouples simultaneously during the tests. The external temperature was measured at 3 different loads: 100%, 125% and 150% of rated load.

4.1.2.1 Experiment #1 : 100 % rated load / 1st motor sample

This section contains results obtained from the 1st motor sample. In this test, there were 8 locations for thermocouple on the external surface of the motor housing. There were also 2 measurement locations for internal temperature of stator winding. The locations of temperature measurement by thermocouple were shown graphically in Figure 4.3. The actual probe attachments are displayed in both Figure 4.4 and Figure 4.5.

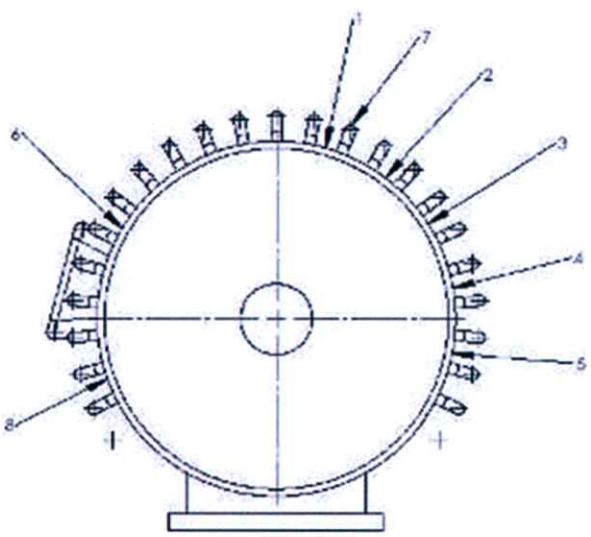

Figure 4.3 Thermocouple locations of external temperature measurement in experiment #1

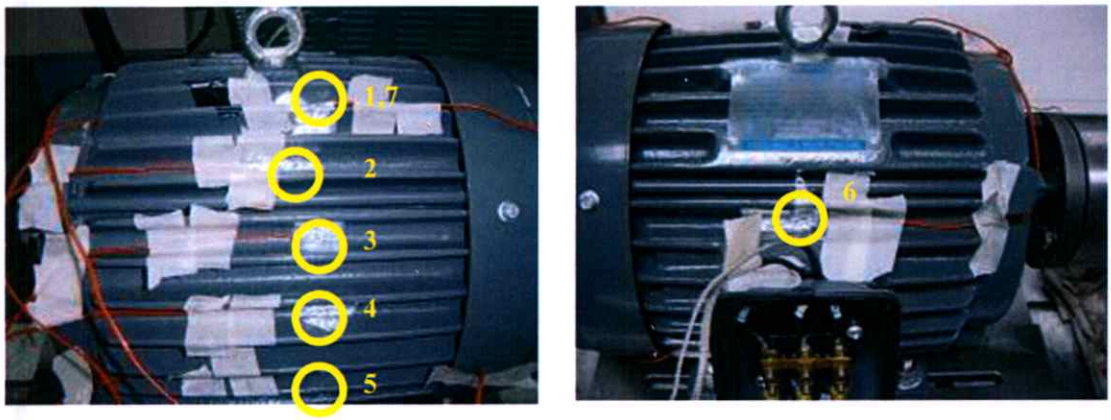

Figure 4.4 Thermocouple probes attachment on housing for external temperature measurement in experiment #1

Figure 4.5 Thermocouples attachment for stator winding temperature measurement by drilling through housing

The temperature measurement had begun at the start of the test until the temperature rose to a steady point. Figure 4.6 shows the temperature rising profile during motor operation. As explained previously, there were 8 external locations on the housing and 2 internal locations at the stator winding.

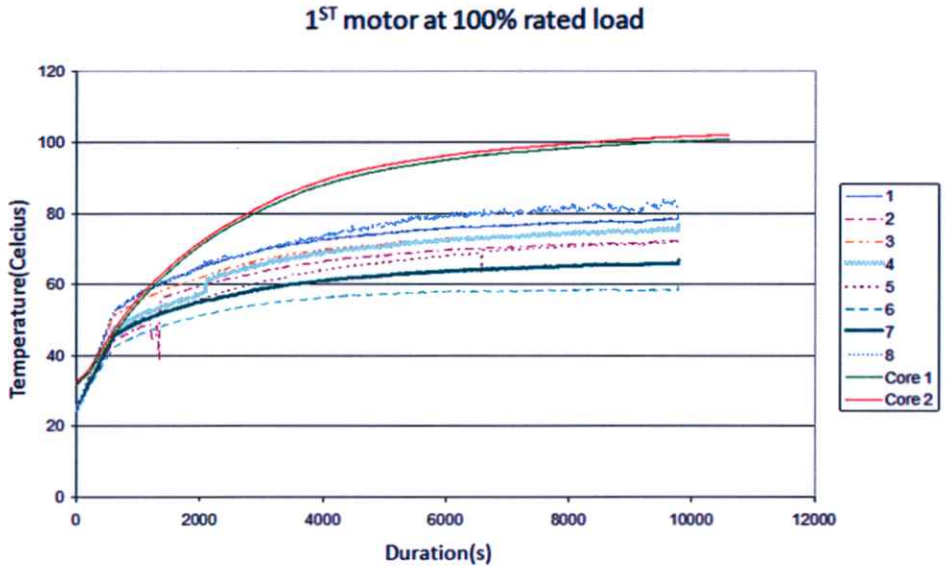

Figure 4.6 External and internal Temperature profile measured by thermocouples from experiment #1

From the measured results, the stator winding temperatures were higher than those external temperatures for approximately 20 °C at steady state. The temperatures at each measurement location on housing surface were similar to each other with the averaged housing surface temperature of 77°C. The values from No.6 and No.7 locations were an exception with lower temperature than others. The No.7 was measured at the tip of motor fin surface while No.6 was measured at housing surface similar to others. It was noticed that there could be an error as the probe was found slightly loosen on the stator surface after the test.

As previously mentioned, the temperature was also measured using an infrared camera. The infrared camera could measure only the temperature of visible surface and displayed the measurement by means of thermograms, which is an image of temperature contour. Several thermograms were captured at constant time interval during the motor test. An example of thermogram at the steady state after 5500 second test period is shown in Figure 4.7. In this study, the temperature levels were separated by a contour at every 5 °C interval.

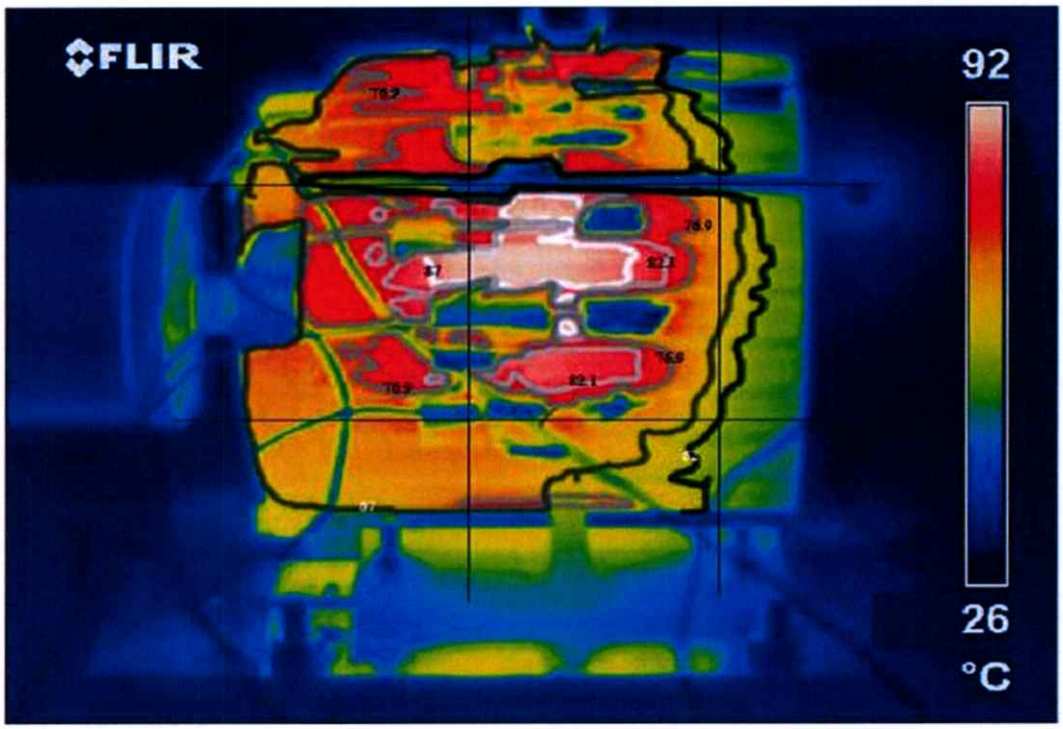

Figure 4.7 Example of thermogram at steady state conditions from experiment #1

4.1.2.2 Experiment #2 : 150 % rated load / 1st motor sample

The applied load at 150% rated load was the highest operating conditions for the motor samples in this study. The 1st motor sample was damaged due to overheat in this experiment. Similar to previous test, there were 8 locations for thermocouples on the external surface of housing and 2 additional measurement locations for internal temperature on stator winding. The locations of temperature measurement by thermocouple were the same as experiment #1 except for the No.8 location, which was on the front-end of housing surface. Figure 4.8 shows the locations of thermocouple probe in this second experiment.

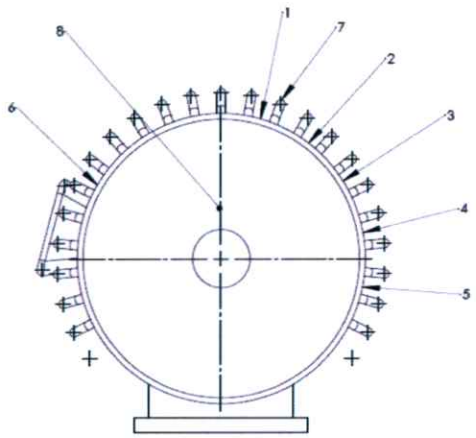

Figure 4.8 Thermocouple attachment locations for experiment #2

Table 4.4 Measured temperatures from the motor before and after operated at 150% rated load

Location	1	2	3	4	5	6	7	8	Internal 1	Internal 2
Temp. at start (°C)	27.2	26.8	26.7	26.4	26.2	26	26.1	26.1	26.865	27.02
Temp at shut down (°C)	107.4	97.5	120.4	113.8	100.5	87.6	94.6	96.8	141.49	148.13

The measurement began when the motor was started to operate. The motor sample could operate at 150% rated load up until 1000 seconds. There was a smoke observed from an inside of housing. As a result, the motor operation was shut down in order to protect a short circuit. Table 4.4 shows the temperature results at the beginning of the test and immediately after a safety shutdown.

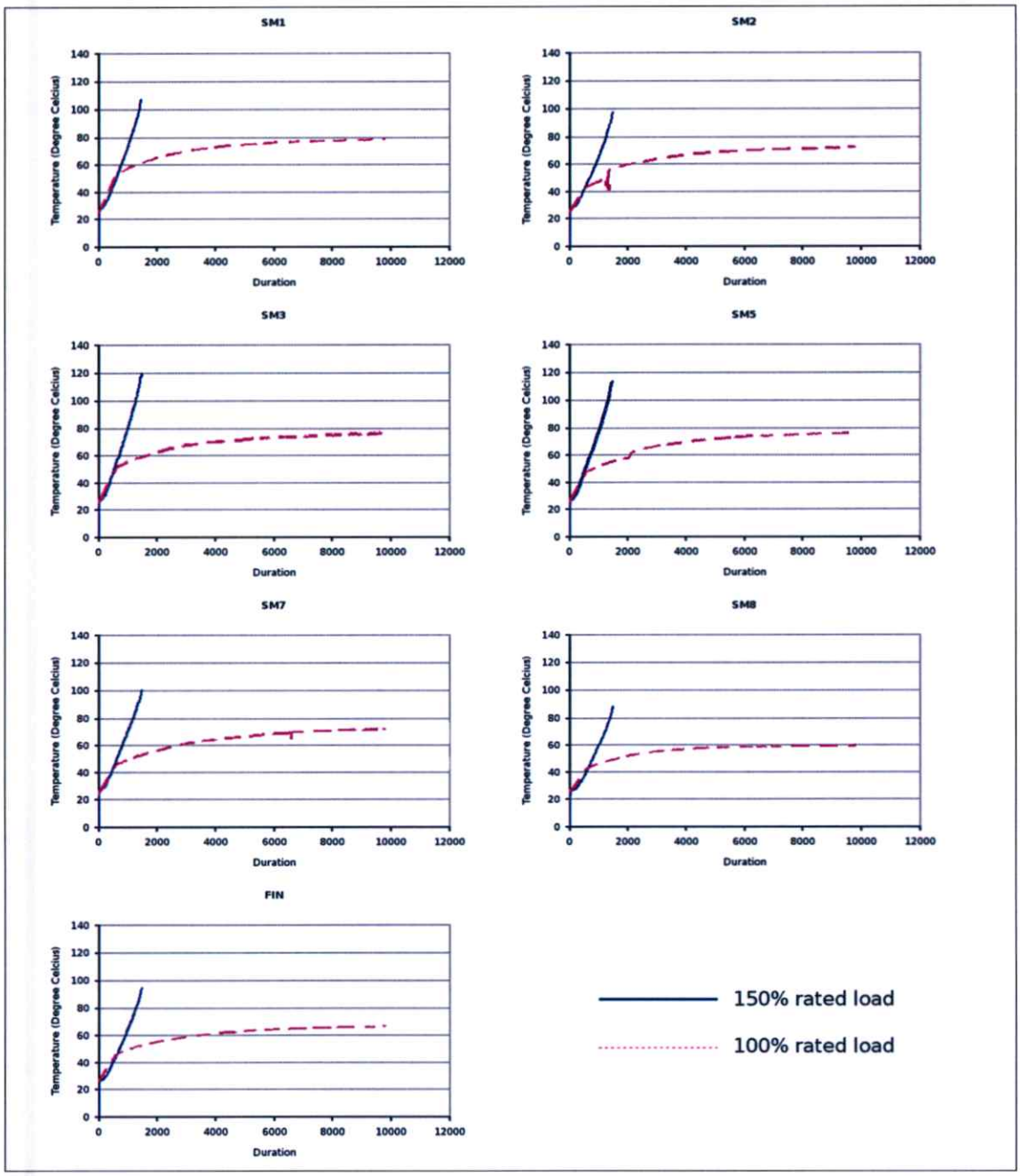

Figure 4.9 Comparison of motor housing surface temperature between 100% rated load and 150% rated load case

As can be seen from Figure 4.9, the temperature raising under the 150% rated load were similar to that under the 100% rated load in the early period of the test. However, the generated temperature in the 150% rated load rose dramatically. This rising of temperature caused damage to the 1st motor sample due to overheat of internal components.

As in previous case, the housing surface temperature was also measured using an infrared camera. An example of thermogram picture with the highest observed temperature at the moment before the motor was shut down is shown in Figure 4.10. The maximum temperature occurred at 25 minutes after the test was carried out. The temperature level were separated by contour line for every 5 °C interval

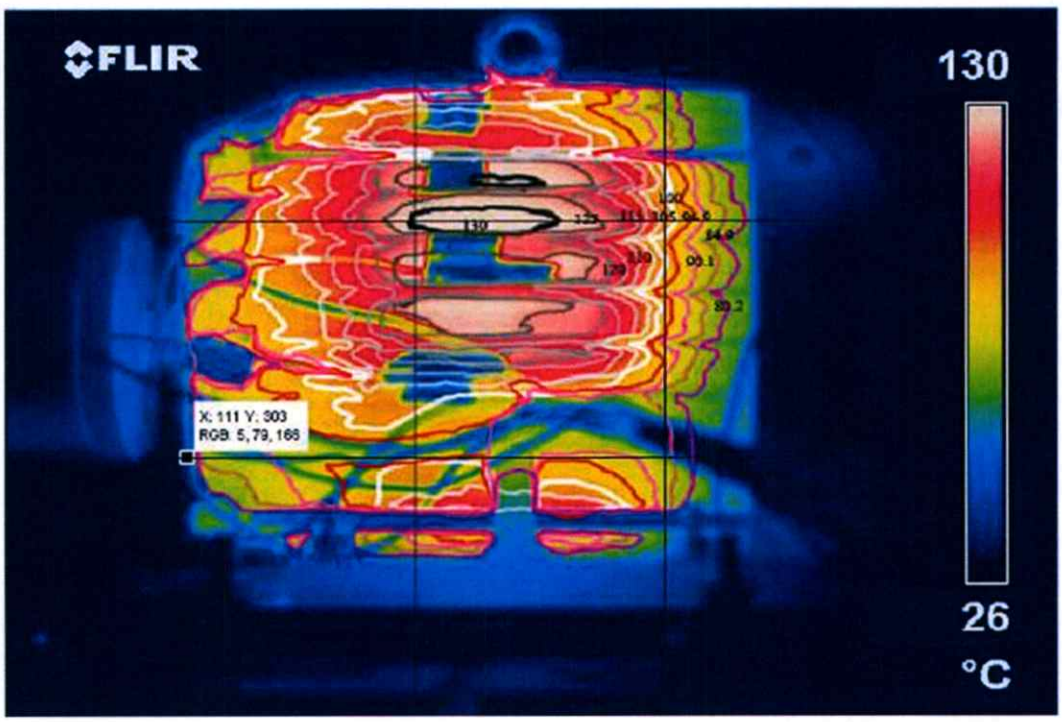

Figure 4.10 Thermogram of maximum temperature of 1st motor operated at 150% rated load

Additionally, after the test motor was shut down, it was observed that the temperature kept rising until the maximum value of 151 °C was recorded by the thermocouple as shown in Figure 4.11. Then, the housing temperatures decreased slowly towards a room temperature. This observed temperature rise after the motor shutdown demonstrated the significance of cooling provided by the motor rear fan.

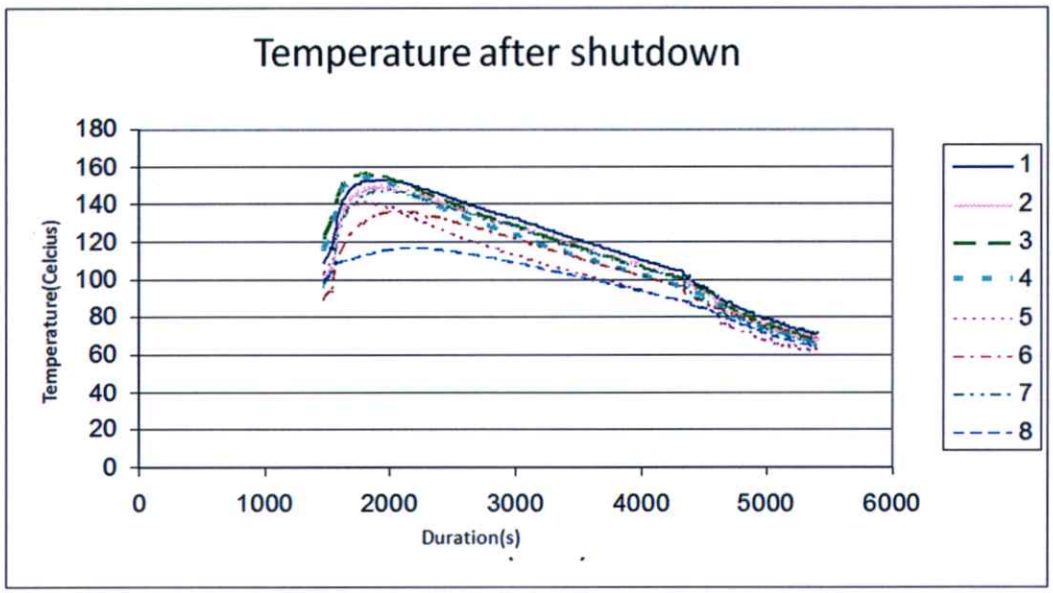

Figure 4.11 Housing temperature profile after motor shut down in 150% rated load test

Table 4.5 Temperature of motor housing operated at 150% rated load after shutdown

Location	1	2	3	4	5	6	7	8
Temperature at shutdown (°C)	107.4	97.5	120.4	113.8	100.5	87.6	94.6	96.8
Maximum temperature(°C)	153.3	149.8	156.3	154.4	141	136.2	147.8	116.7
Shutdown duration (s)	1880	1940	1790	1770	1800	2020	1980	2150

4.1.2.3 Experiment #3 : 100 % rated load / 2nd motor sample

Due to the damage of the 1st motor sample in the 150% rated load test, further experiment was carried out on the2nd motor sample, which was the same model. The measurement locations for thermocouples were added from 8 points to 29 points in order to obtain more detailed information with more internal measurement locations. In this test, the 100% rated load experiment was repeated to obtain more information under this load condition and to compare with the previous results from the experiment #1. All thermocouple probe locations were explained as followed:

1. 3 locations on the housing surface at front end (shaft side) as shown in Figure 4.12

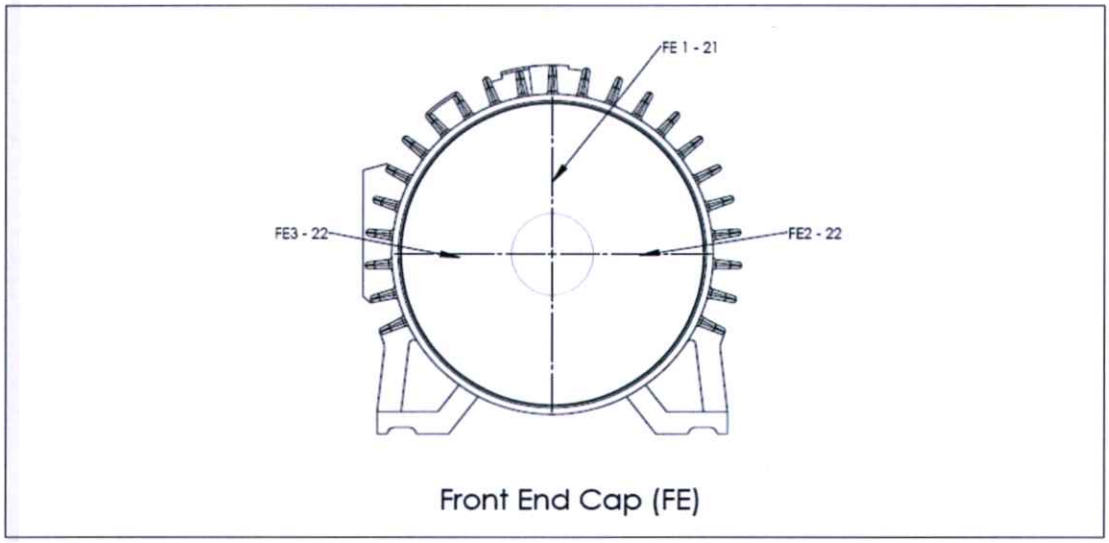

Figure 4.12 The thermocouple probe locations at front end of housing

2. 8 locations on the cylindrical surface of the main housing near the shaft side as shown in Figure 4.13

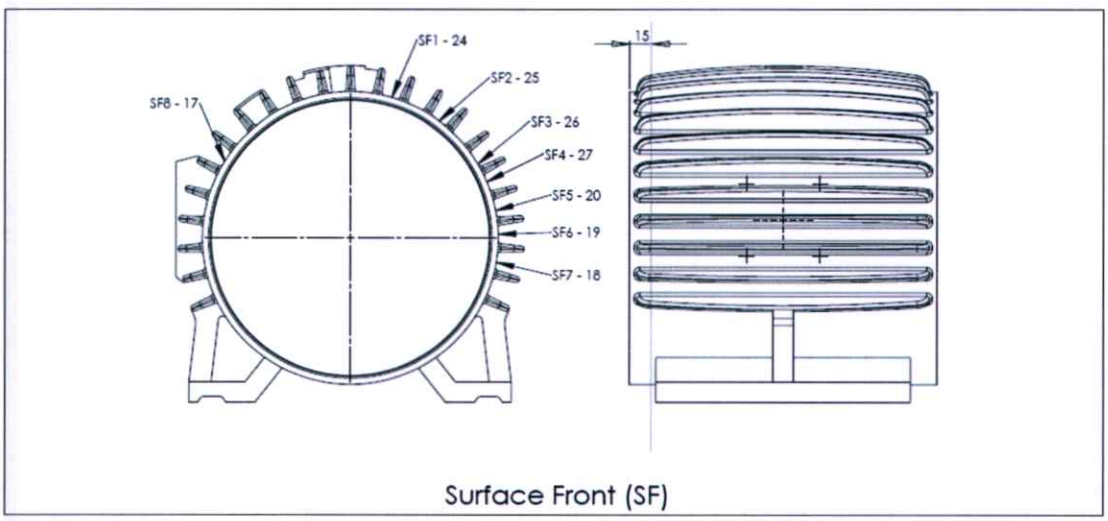

Figure 4.13 The thermocouple probe locations at main housing surface near the shaft

3. 8 locations on the middle section of the cylindrical surface of the main housing as displayed in Figure 4.14

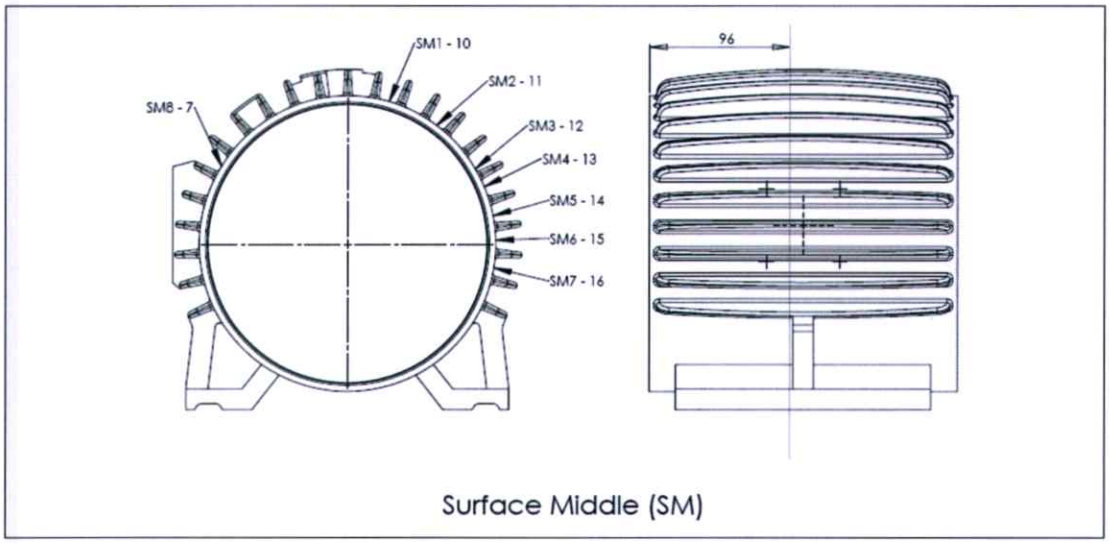

Figure 4.14 The thermocouple probe locations at cylindrical surface around the middle section of housing main body

4. 4 locations on each front and rear end surface of stator as shown in Figure 4.15

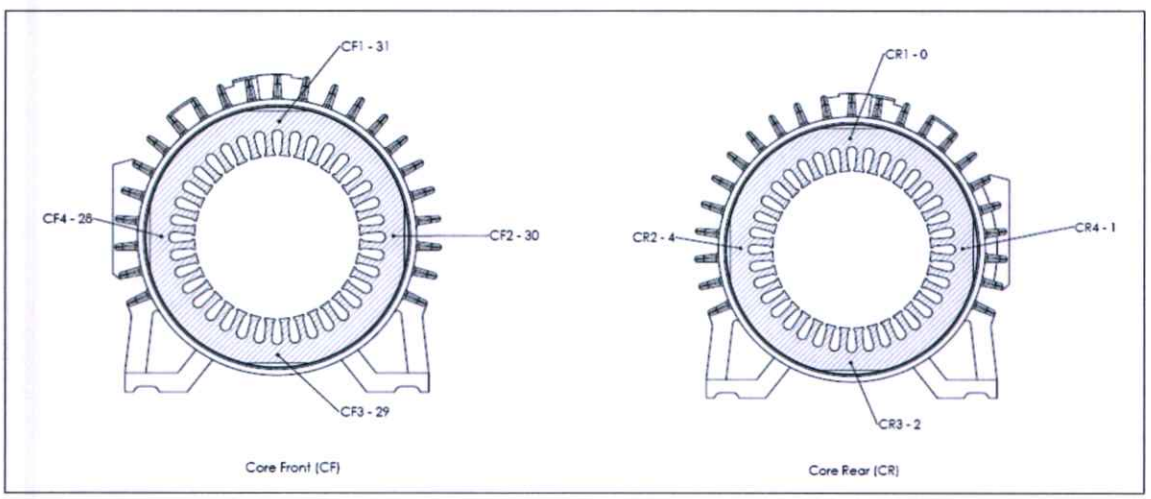

Figure 4.15 The thermocouple probe location at front and rear surface of stator core

5. 2 locations on the side surface of stator core in the middle section as shown in Figure 4.16

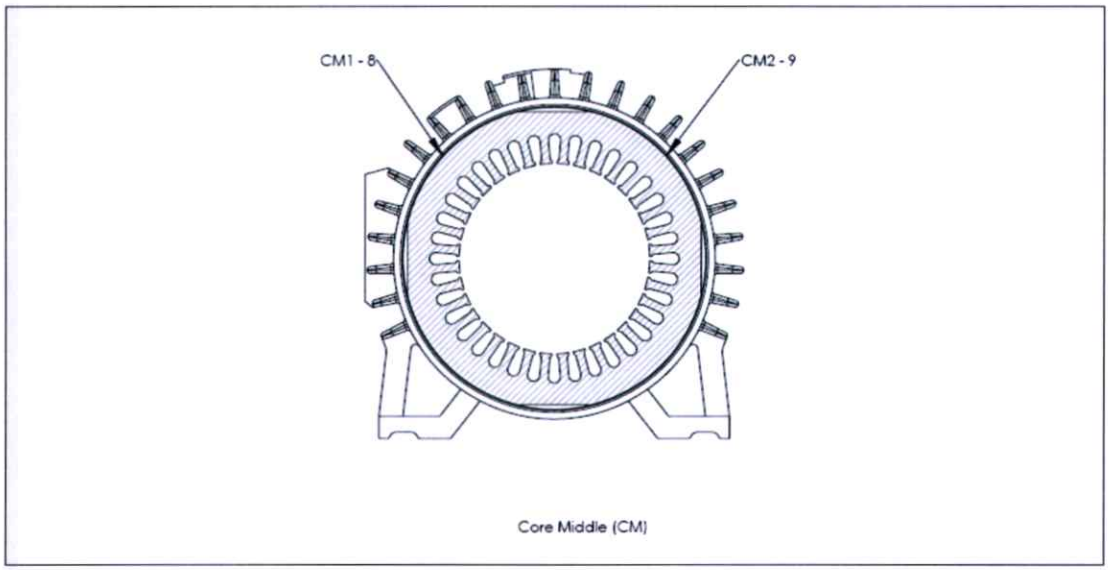

Figure 4.16 The thermocouple probe locations on side surface of stator core

The results of temperature variation by the measurement locations during the test are plotted below from Figure 4.17 to Figure 4.22.

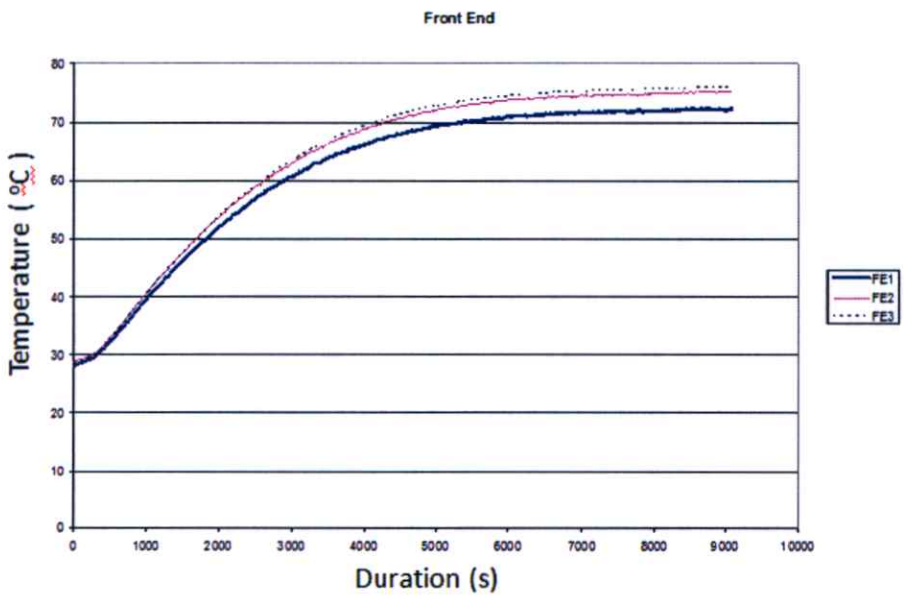

Figure 4.17 Temperature on the front end surface of housing (shaft side) at 100% rated load

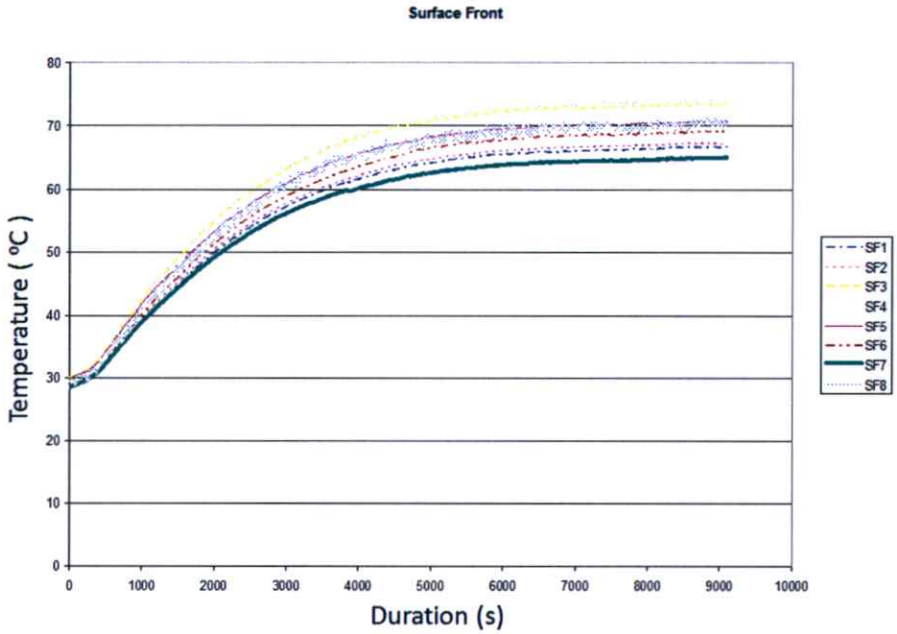

Figure 4.18 Temperature on the cylindrical housing surface closed to the shaft side at 100% rated load

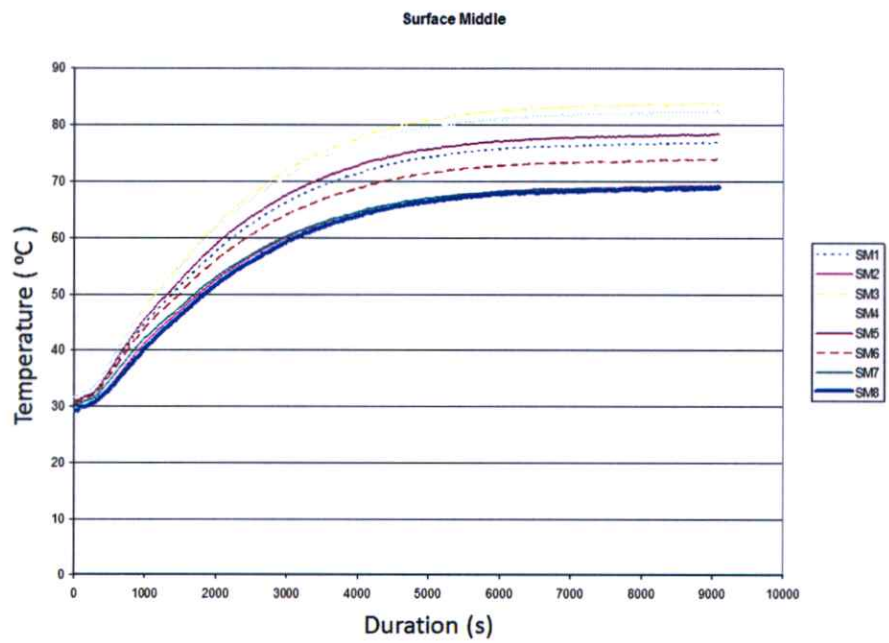

Figure 4.19 Temperature on the cylindrical housing surface around the middle section of body at 100% rated load

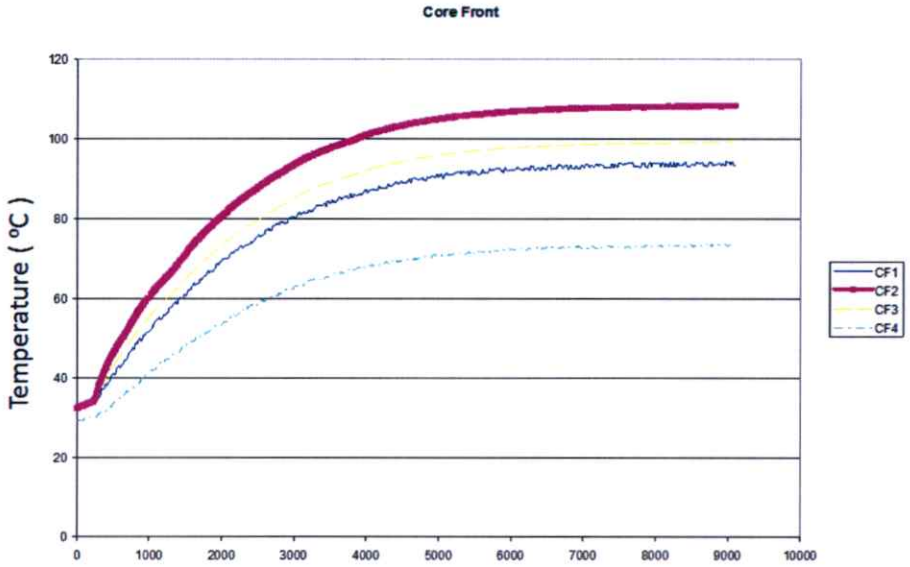

Figure 4.20 Temperature on the front end of stator core at 100% rated load

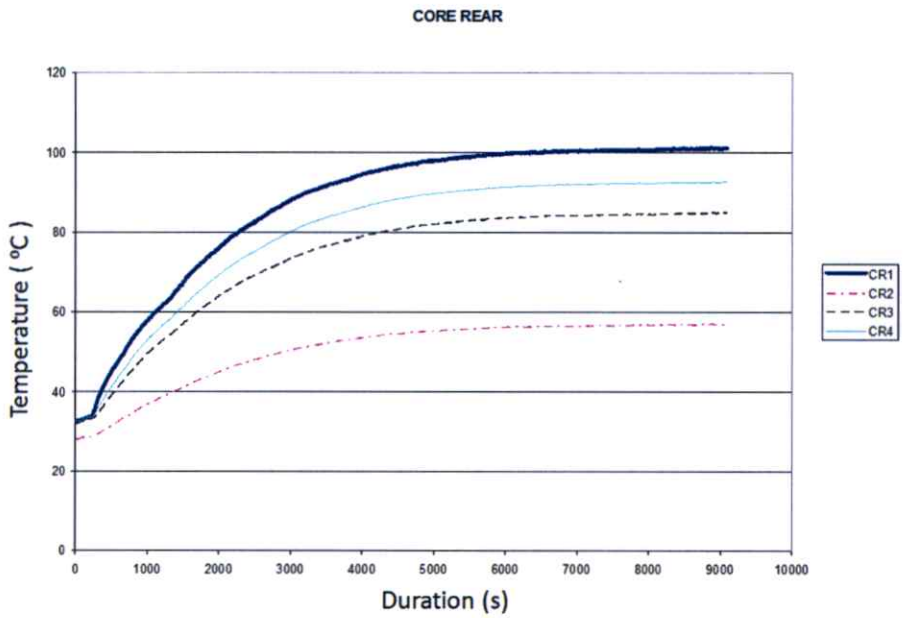

Figure 4.21 Temperature on the rear end of stator core at 100% rated load

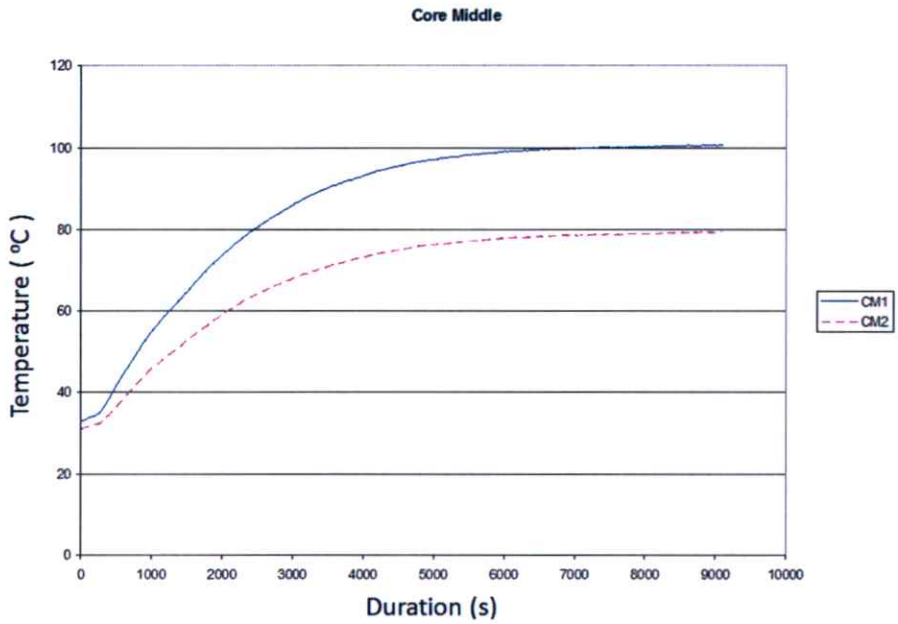

Figure 4.22 Temperature on the middle surface of stator core at 100% rated load

4.1.2.4 Experiment #4 : 120 % rated load / 2nd motor sample

According to the motor damage at 150% rated load in the previous experiment (#2), only 120% rated load was applied to the 2nd motor in this experiment. The same 29 probe locations were used as explained in the previous experiment. The resulting temperature variations from each local area of the test motor are shown in Figure 4.23-Figure 4.28. Additionally, the corresponding thermogram of the maximum temperature observed on the motor sample at the end of the test is shown in Figure 4.29.

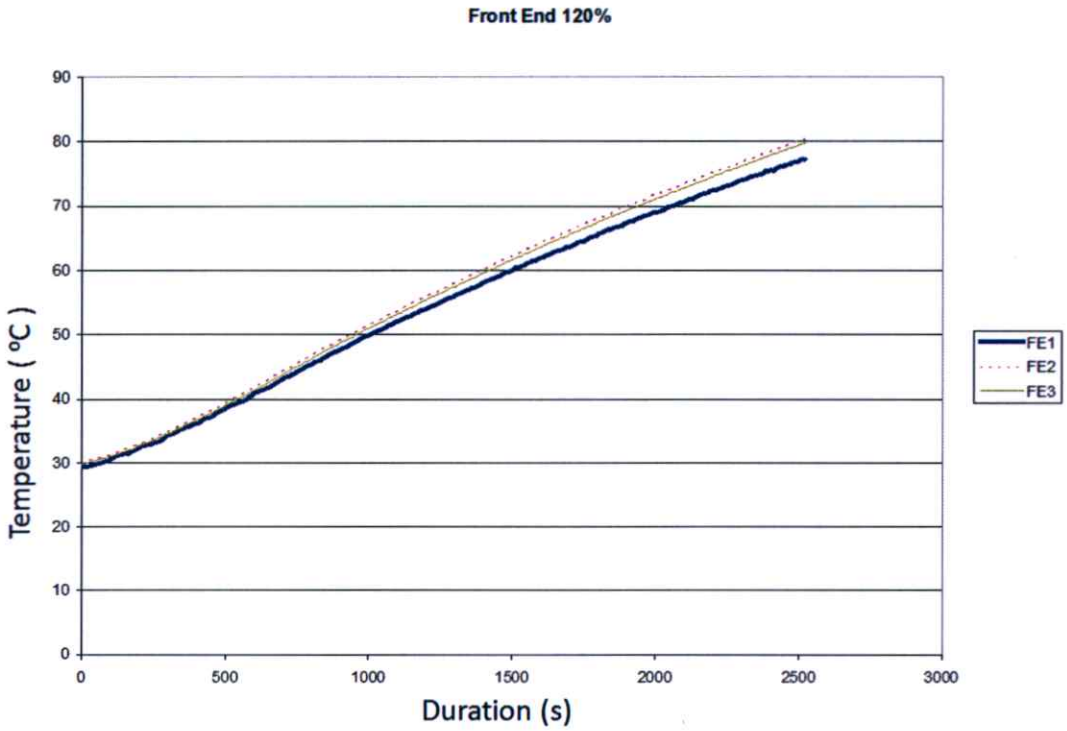

Figure 4.23 Temperature on the front end surface of housing (shaft side) at 120% rated load

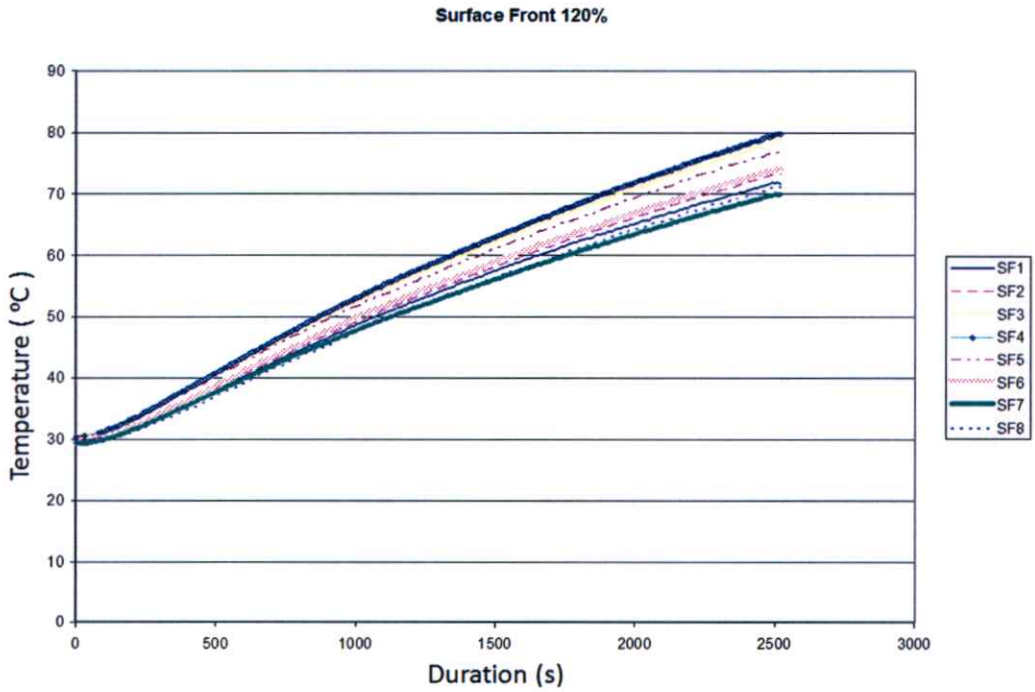

Figure 4.24 Temperature on the cylindrical housing surface closed to the shaft side at 120% rated load

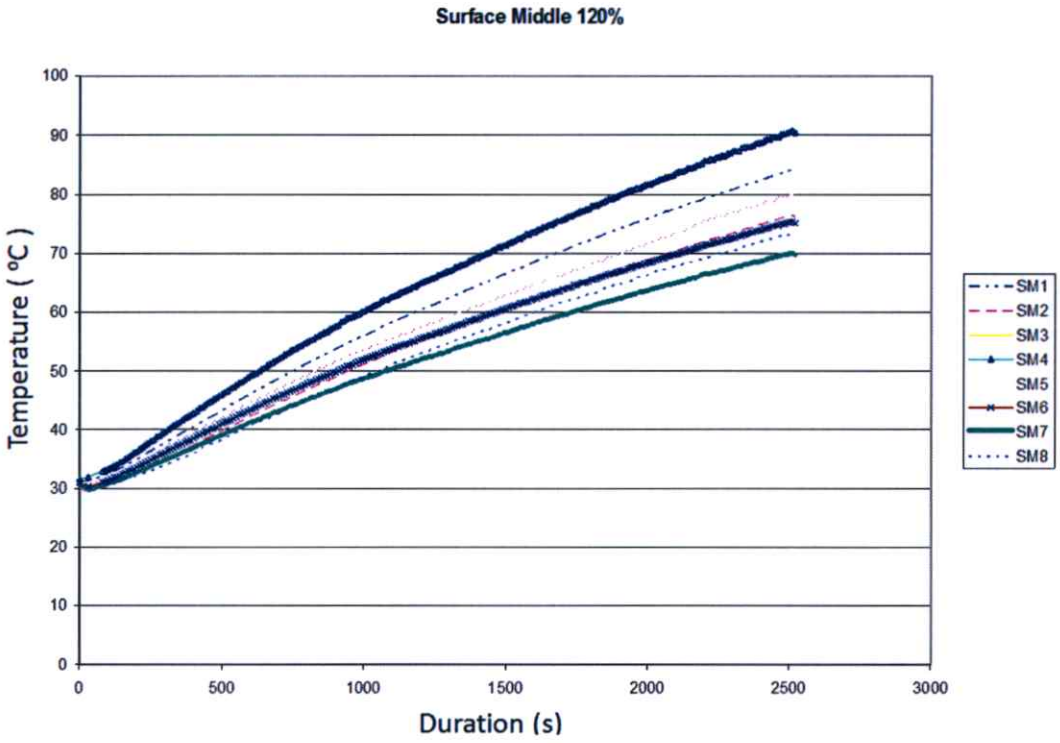

Figure 4.25 Temperature on the cylindrical housing surface around the middle section of body at 120% rated load

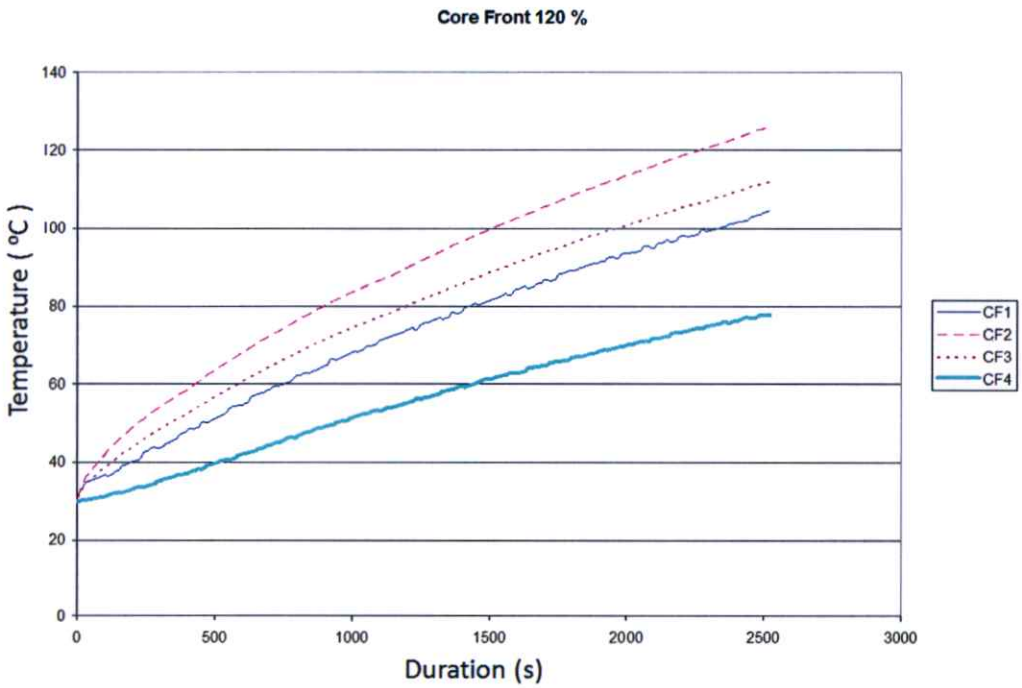

Figure 4.26 Temperature on the front end of stator core at 120% rated load

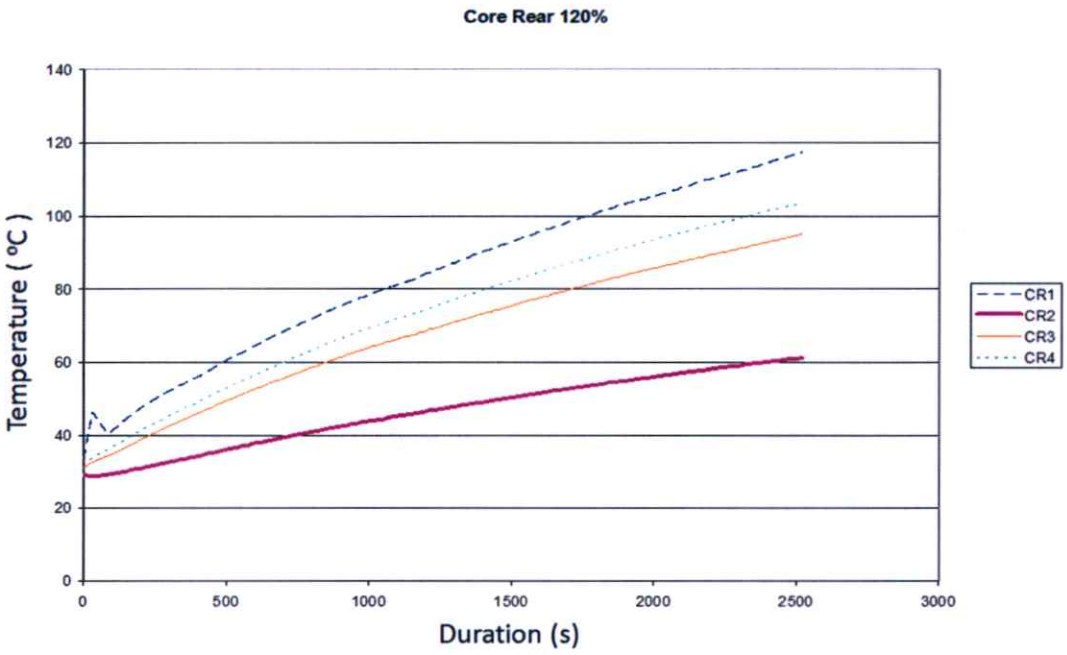

Figure 4.27 Temperature on the rear end of stator core at 120% rated load

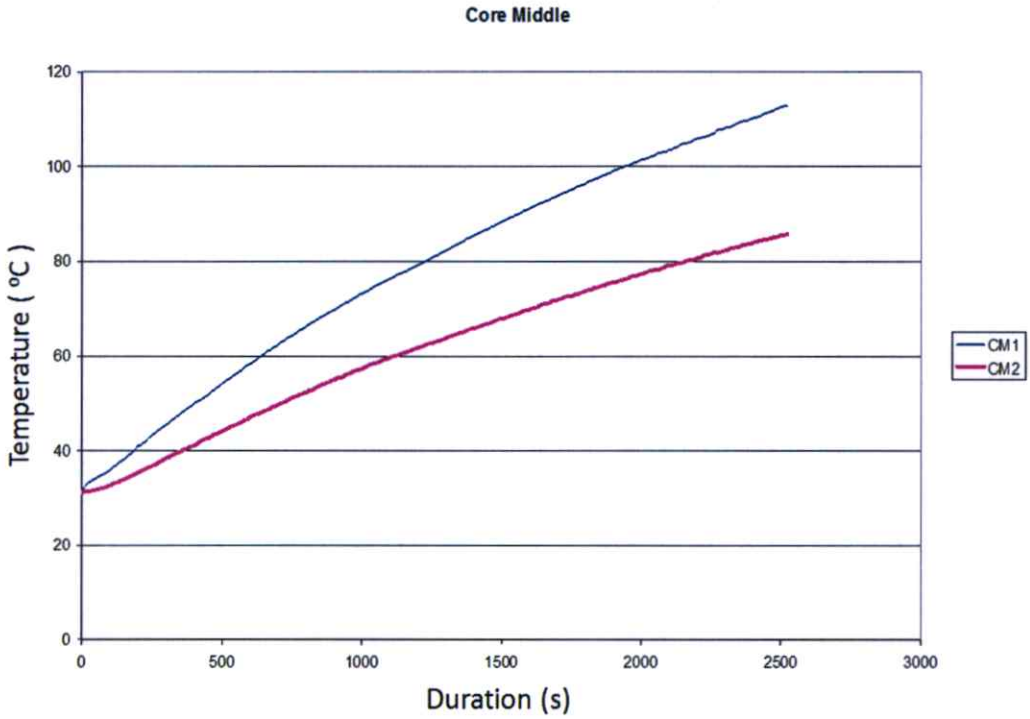

Figure 4.28 Temperature on the middle surface of stator core at 120% rated load

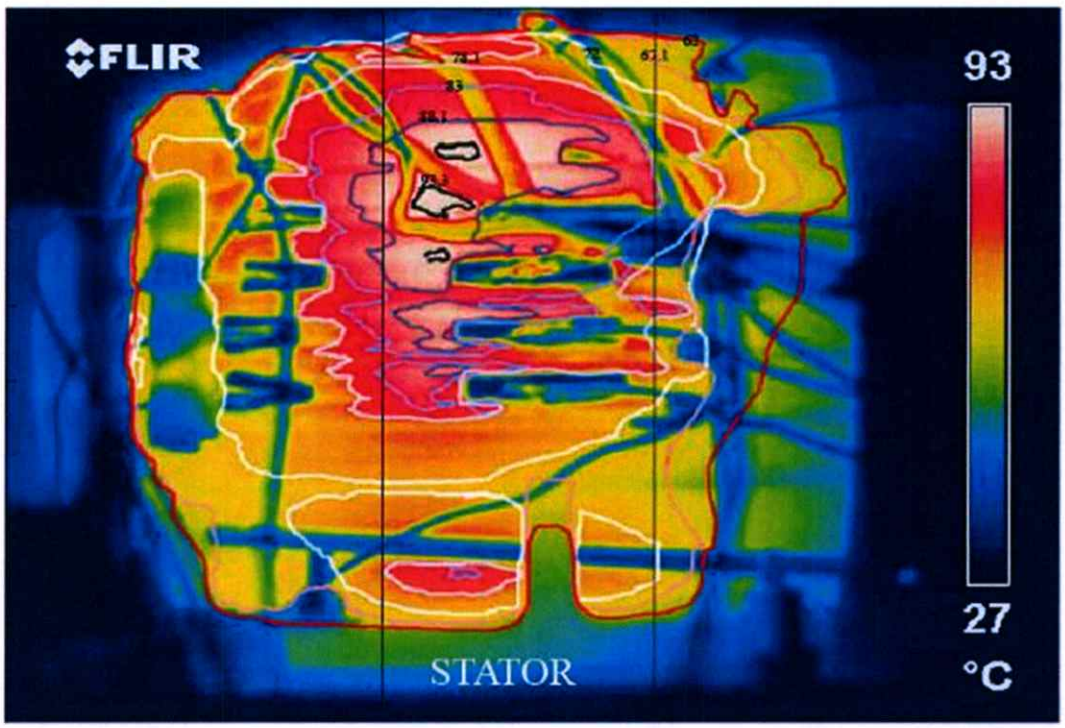

Figure 4.29 Thermogram of the 2nd motor sample operated at 120% rated load captured at the end of the test (before unloaded)

Moreover, at the end of the main experiment (120% load), the motor was further operated under no-load condition in which there was no mechanical load applied to the motor while the motor shaft i.e. the fan was allowed to rotate to generate the air flow to cool down the motor, preventing overheat observed from the 150% load case. The observed temperature declines from various locations are displayed in Figure 4.30. The results obtained from this case could be applied to calculate the cooling capacity of fan.

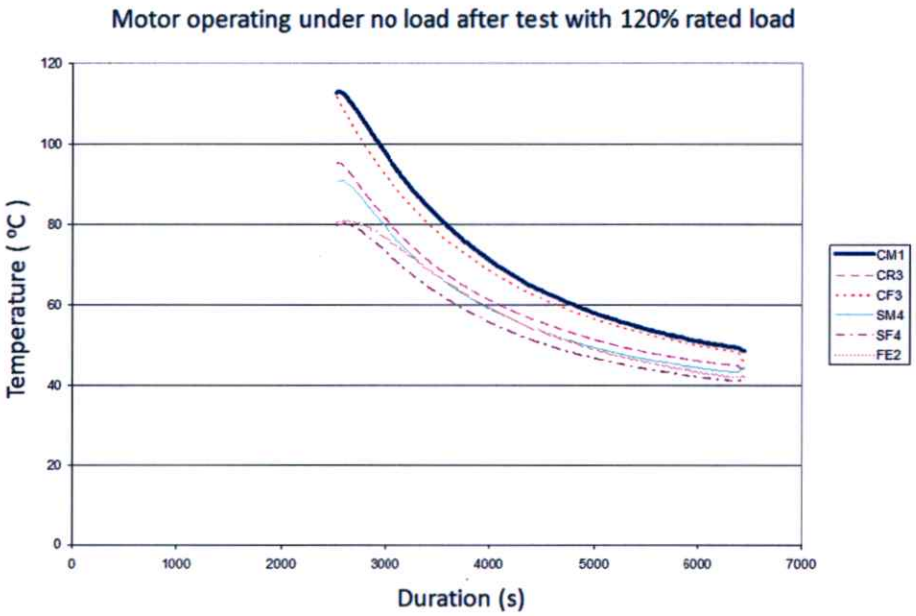

Figure 4.30 Temperature variation of motor parts operating under no mechanical load after a test with 120% rated load

4.1.2.5 Experiment #5 : 100 % rated load / 2nd motor sample/ Internal temperature measurement

In a further attempt to validate the computational results on a temperature distribution inside the motor, the corresponding temperatures of several internal components such as rotor, stator, and copper winding were measured during the test using the infrared camera. In order to carry out this particular test, the front and main housing of test motor were partially cut on the top-right quarter of the frame as shown in Figure 4.31 and Figure 4.32. A 100% rated load was applied to the motor in this test.

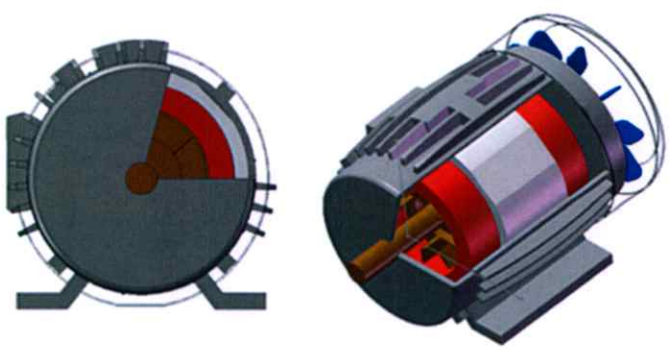

Figure 4.31 Schematic layout of housing preparation for internal temperature measurement by thermo camera

Figure 4.32 Actual test motor with cut-off housing for internal temperature measurement

Since the use of thermocouples was not applicable on the internal components for safety reason, the infrared camera was employed. The camera was firmly fixed on a tripod to ensure the same measurement location each time during the test while the temperature markers were assigned on the camera screen to display the desired temperatures. The measurement was recorded on 7 locations for the temperature of internal components as listed below and displayed in Figure 4.33.

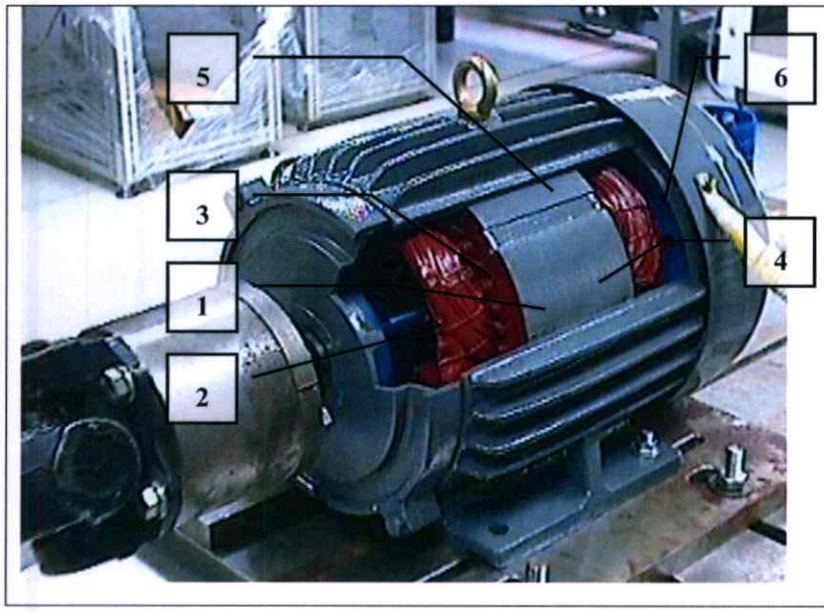

1. Front surface of stator core
2. Rotor core
3. Copper winding at the front end of stator core
4. Middle of cylindrical surface of stator core
5. Interface between housing and stator core
6. Copper winding at the rear of stator core
7. Tip of rotor fin

Figure 4.33 The selected locations for internal temperature measurement by infrared camera

The results of measurement on internal motor components were recorded as graphical thermograms as shown in Figure 4.34. The highest temperature could be seen, in descending order, on the fin of rotor core, rotor shaft, and the front side of copper winding respectively. Furthermore, regarding the fan location at the rear part of motor, the temperature on the areas far away from fan was found to have a significantly higher temperature than those within the vicinity of the fan area. One of an example was the copper winding in front of the stator that had a higher temperature than the copper winding on the rear side.

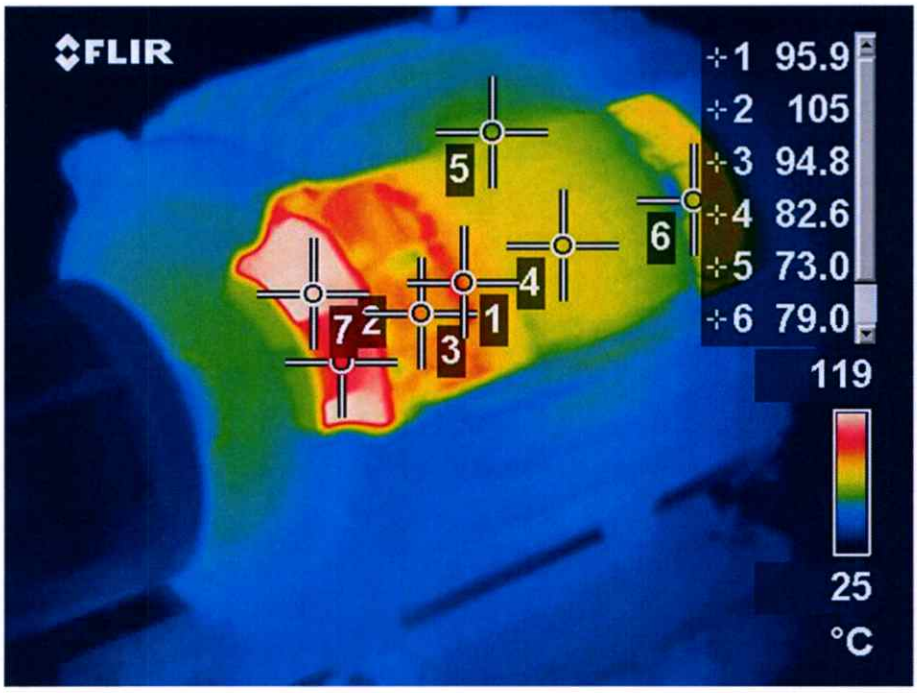

Figure 4.34 Example of thermogram showing the internal components temperatures at steady-state under 100% rated load with temperature markers for individual temperature value on a camera display screen

The measurements were recorded at every 5-minute interval during the motor operation from a start until the temperature was steady. The obtained results from each measurement were plotted together to show the rate of temperature rise inside the motor as shown in Figure 4.35. From the results, the temperature of internal components increased until reaching the steady state for the duration of 90 minutes. The variation trend of temperatures was similar to those observed from the housing surface in the previous tests. The corresponding temperatures of each internal motor component at steady state are listed in Table 4.6.

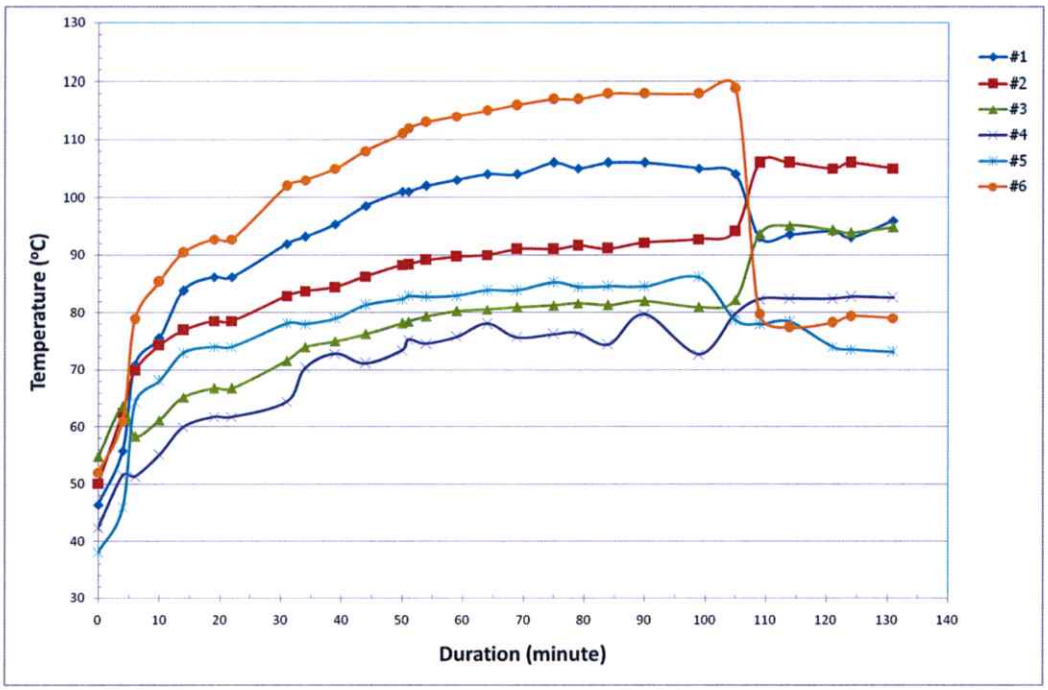

Figure 4.35 The variation of temperature on internal motor components for motor operated at 100% rated load

Table 4.6 Steady state temperatures of internal motor components operated at 100% rated load

Position	Measurement Locations	Temperature (°C)
1	Front surface of stator core	95.9
2	Rotor core	105
3	Copper winding in front of stator	94.8
4	Cylindrical surface on outside of stator core	82.6
5	Housing	73
6	Copper winding on the rear of stator	79
7	Tip of rotor fin	119

The results of internal component temperature could be applied to solve the heat transfer effect in the internal of motor. The simulation results were validated with the experimental results. The validated simulation model was applied as the heat generation model for liquid cooling system designing.

4.2 Material Thermal Properties Measurement

As explained in the previous chapter, in order to perform a computational analysis on a heat transfer phenomena in an induction motor involving heat conduction and heat convection mechanisms, several thermal material properties of both solid objects and coolant were required. The relevant values obtained from the test as well as how they were assigned into the computational model are reported in this section.

In order to analyze heat transfer of TEFC motor, the simulation model should comprised of necessary components such as rotor, stator, copper winding, housing, fan, fan cap and the internal/external air domain as shown in Figure 4.36

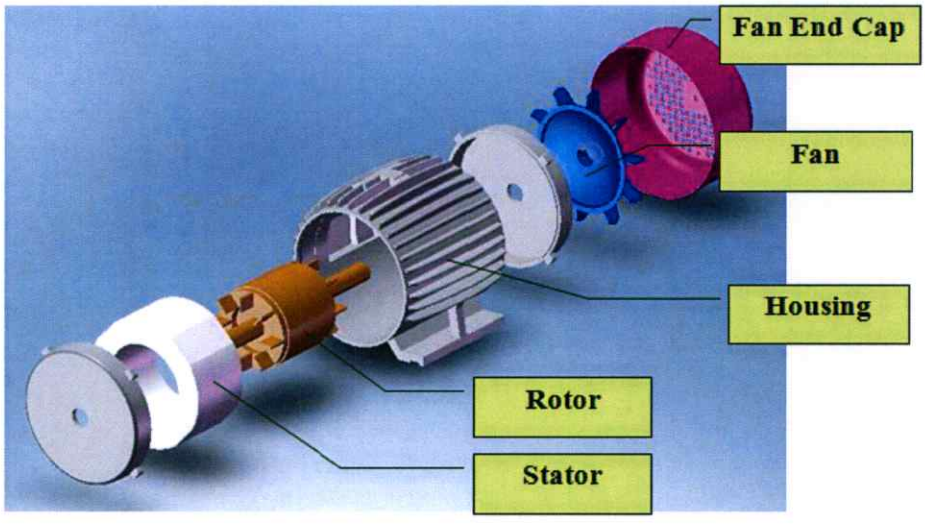

Figure 4.36 The model of TEFC motor components for heat transfer simulation

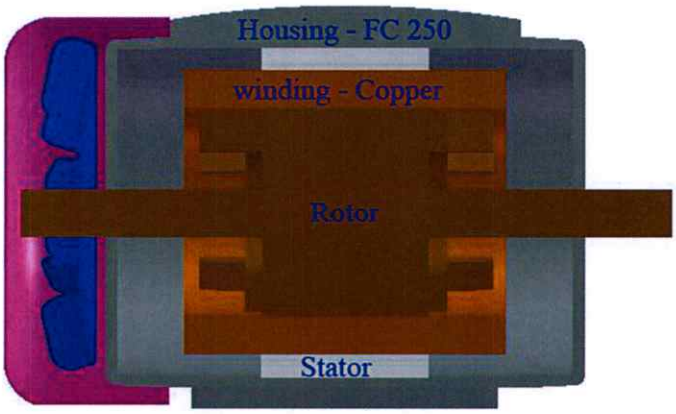

Figure 4.37 Cross section of TEFC motor model for heat transfer simulation

The details of properties to assign in each motor component were explained in following.

4.2.1 Solid

As explained in chapter 3, the solid objects that were important for the thermal analysis were comprised of a rotor, stator, copper winding, and housing.

4.2.1.1 Rotor

From a physical inspection of the spared parts from the test motor, it was found that the rotor assembly could be represented by two main parts, which were a rotor shaft and a rotor core (Figure 4.38(a)). Generally, the shaft is inserted into the center of the core with a spline configuration. The rotor core itself is an assembly of thin metal sheets compressed together as can be seen from Figure 4.38(c). Considering a cross sectional view of the core in Figure 4.38(b), there are 28 poles of squirrel cage made from aluminum located at the outside diameter. These poles are all connected to the fins of rotor at both front and rear edges of rotor core.

(a) (b) (c)

Figure 4.38 Physical inspection of a rotor component (a) rotor assembly (b) cross-section of rotor core and (c) section along the length of rotor core

In order to reduce the time and computation resource of simulation, the rotor model was simplified as a uniform solid model assigned with the steel material properties. The relevant heat transfer properties of rotor steel obtained from TCA and DSC techniques explained in previous chapter (Section 3.1.4.1) are shown in Table 4.7.

Table 4.7 Heat transfer properties of solid parts of motor

Properties	Steel	Copper	FC250 Cast Iron
Density	8030	8939.58	7250-7400
Thermal conductivity (w/m-K)	60.5	401	42.8
Specific Heat Capacity: Cp (J/kg-K)	502.48	385.718	503

4.2.1.2 Stator

The stator core was an assembly of thin metal sheet similar to a rotor core. The general appearance of stator core was a cylinder with a through hole at the center, which was a place to accommodate a rotor. The inner edge of a cylindrical surface was cut as a array of slots to place the copper winding. Similarly to the case of rotor, the analytical model of stator was simplified to a uniform solid with the properties of steel as those assigned in rotor from Table 4.7.

4.2.1.3 Copper winding

A Copper winding interwoven around the stator core was the copper wires with 1-2 millimeter in diameter. The surface of the copper wire was coated with an electrical insulator, which could resist the heat up to a certain limit. The grade of the insulator was the main factor in determining a capacity of motor. As observed from Section 4.1.2.2 the experiment #2 (150% load), when the motor was operated at overload for a certain period of time, the exceeding heat could cause a burnt damage to the insulation which, in turns, would allow an electrical short circuit within the copper winding.

For simulation purpose, the model of copper winding was simplified as a single uniform solid assigned with copper properties. The relevant heat transfer properties of copper obtained via TCA and DSC techniques are shown in Table 4.7.

4.2.1.4 Housing

From initial inspection, it could be seen that the housing was fabricated from iron casting process. Additionally, the surface of housing was coated with a rust protection agent. A small sample of specimen was cut off from the housing to undergo the optical emission

spectroscope test. The chemical composition results suggested that the material of the housing was of FC250 cast iron, which possessed the relevant thermal properties as shown in Table 4.7.

4.2.2 Coolant Agent

The cooling oil was selected to use as coolant in liquid cooling system for motor. The coolant oil was tested using DSC technique to determine the specific heat capacity, which is an influential property for the convective heat transfer. The specific heat capacity of coolant oil was measured in a temperature range of 30-250 °C, which is similar to the operating temperature of motor in this study. The test condition was to increase specimen temperature at 10°C/minute until the temperature reached 250°C and was kept stable for 2 minutes in the nitrogen chamber. The test could determine the specific heat capacity according to DIN 51007 standard. The specific heat capacity results of selected cooling oil are shown in Figure 4.39.

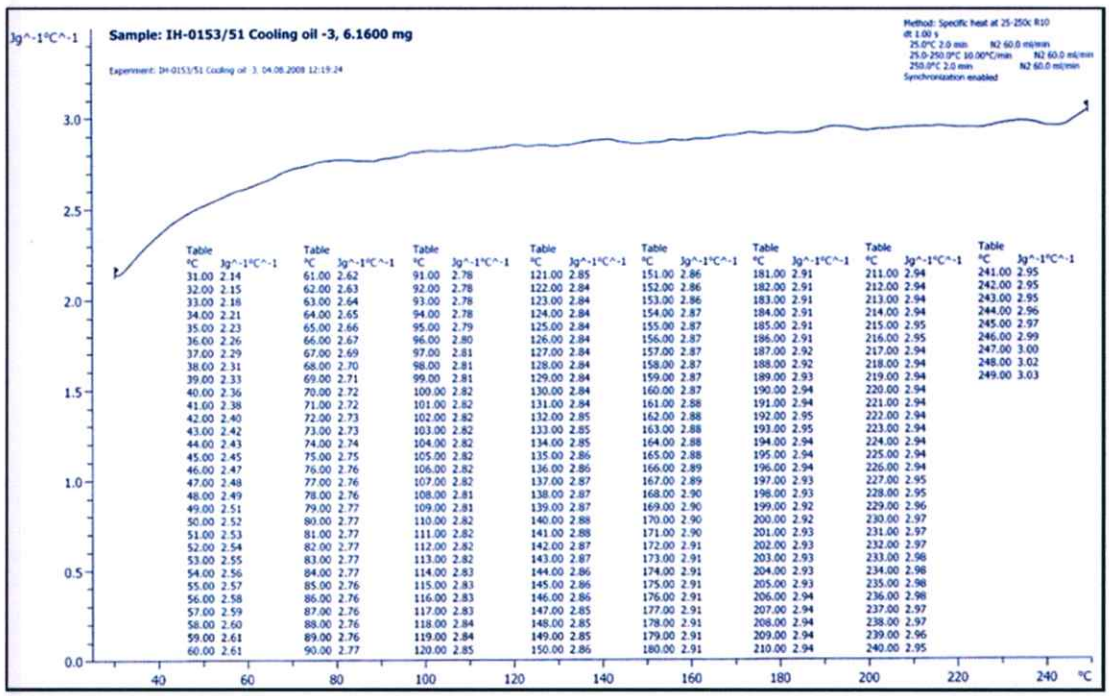

Figure 4.39 DSC specific heat capacity test results of selected cooling oil

The results showed that the specific heat capacity depended on the coolant temperature. When the temperature went up, the corresponding specific heat capacity was increased. The interested temperature range was between 30-160 °C in which the specific heat

capacity was determined to be 2.14-2.87 J/g.°C. The overall heat transfer properties of cooling oil are shown in Table 4.8. Apart from the test results, some of properties were referred from a data sheet provided by the manufacturer.

Table 4.8 Heat transfer properties of selected cooling oil at 100 °C

Properties	Properties value
Thermal Conductivity (W/m.K)	2.173
Specific Heat (J/g-K)	2.82
Density (kg/m^3)	811
Kinematic Viscosity (mm^2/s)	4.7
Flash Point FMCC (°C)	220
Fire Point COC (°C)	255
Pour Point (°C)	-12
Auto Ignition Temperature (°C)	360

4.2.3 Thermal Contact Resistance

As mentioned in the previous chapter, in the heat transfer simulation of an induction motor, there were a couple of thermal contact interfaces necessary to be considered. One was the contact between stator-to-housing and another was a contact between rotor-to-stator. The results of thermal contact resistance investigations are reported in this section.

4.2.3.1 Stator-to-housing

Examples of the thermogram from the stator-to-housing experiment at steady-state are shown in Figure 4.40. The specimen was heated by a uniform heat flux at the cylindrical surface of inner hole where the rotor would be located.

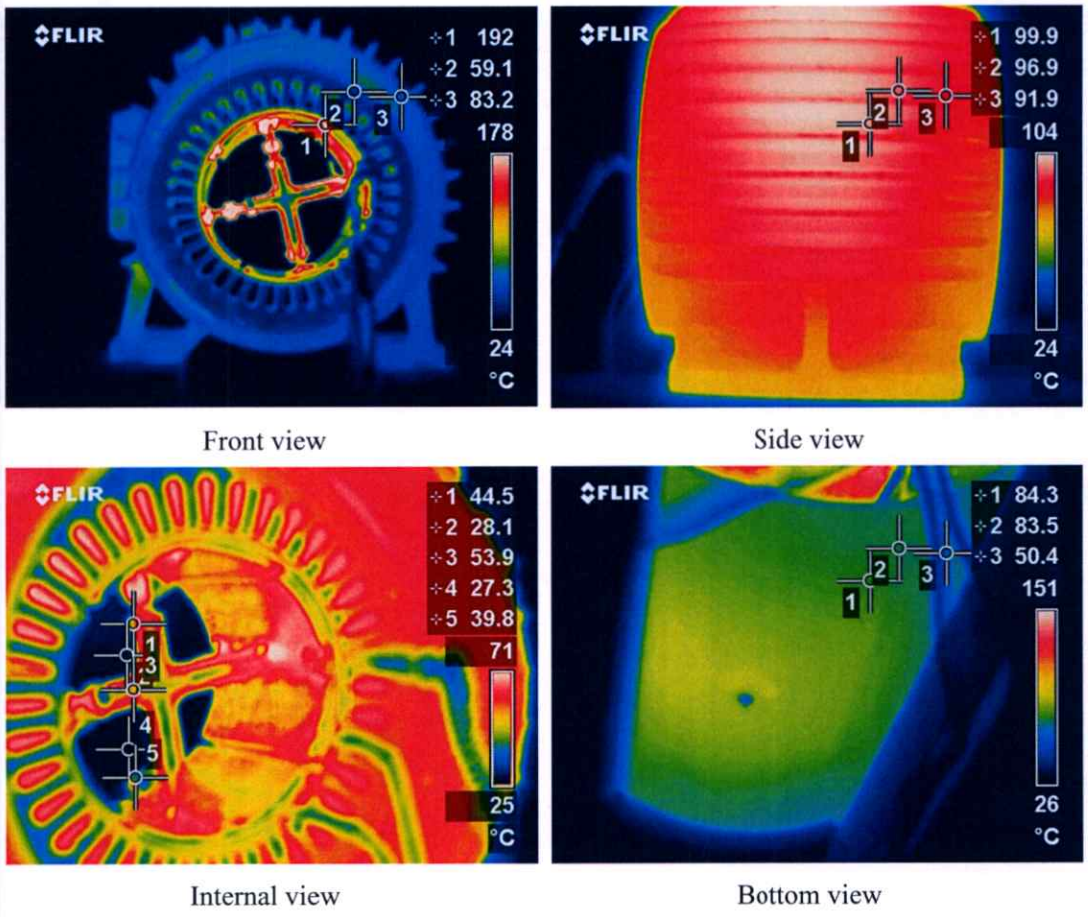

Figure 4.40 Steady state thermograms from the stator-to-housing contact experiment

The experimental temperature results were compared with those from the simulation to determine the appropriate value of stator-to-housing thermal contact resistance. Four different sets of radial temperature variation were taken from the thermogram along the locations shown in Figure 4.41. The result of stator-to-housing contact simulation is shown in Figure 4.42 and the temperature results comparison between simulation and measurement is shown in Figure 4.43.

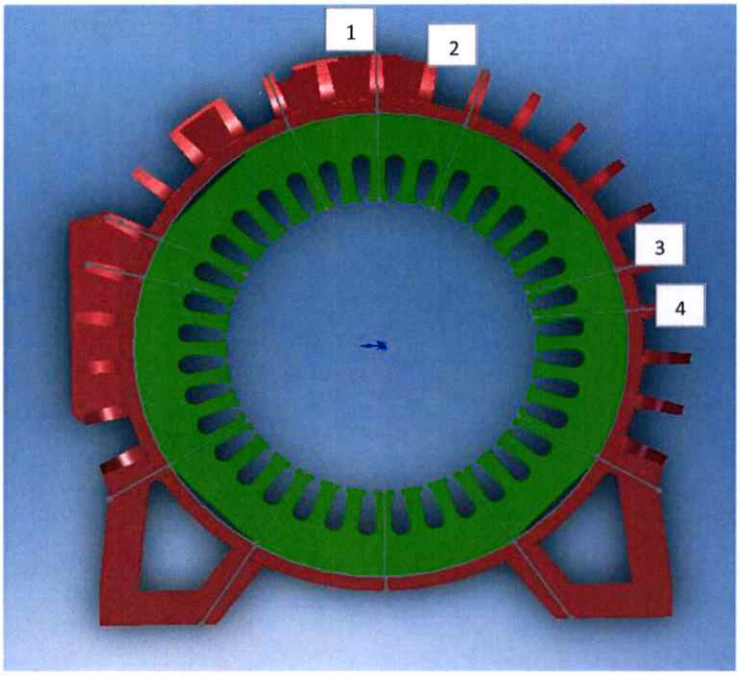

Figure 4.41 Temperature sampling positions for result comparison of the stator-to-housing contact

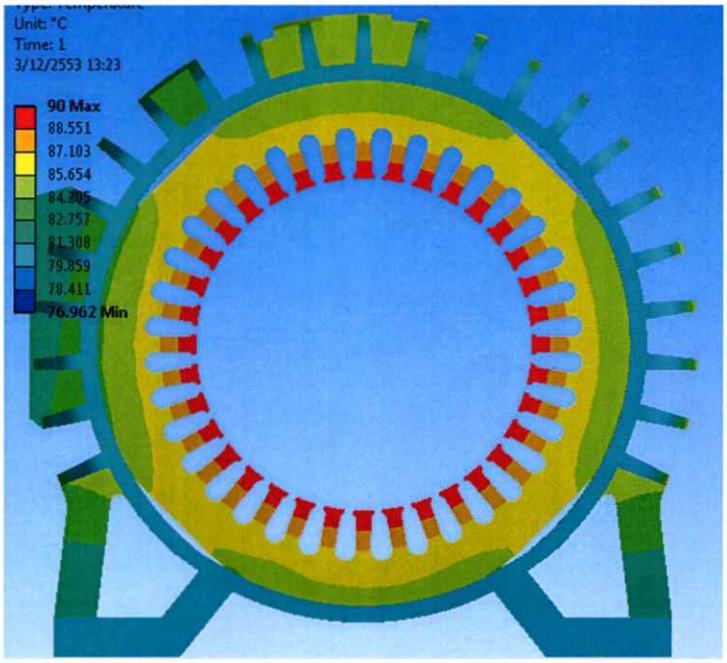

Figure 4.42 Simulation results for stator-to-housing thermal contact determination

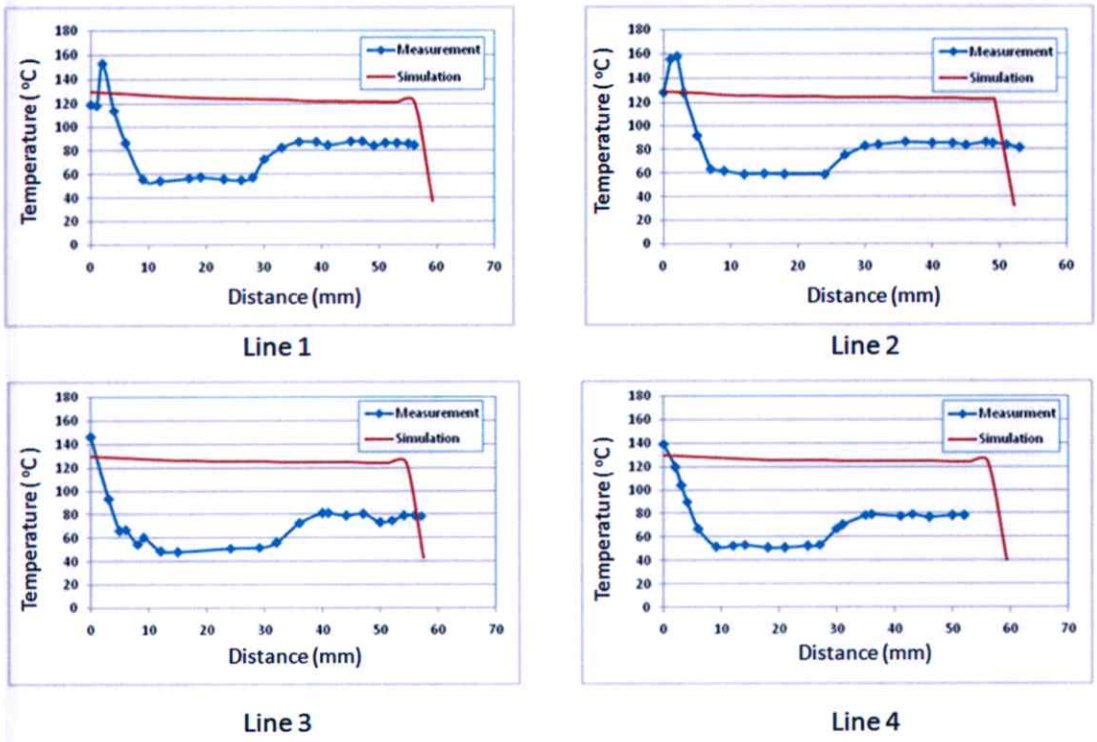

Figure 4.43 Comparison of radial temperature distribution between measurement and simulation for stator-to-housing thermal contact resistance determination

As can be seen from the comparison in Figure 4.43, there was a significant difference between simulation and experiment results. The experimental results displayed a significant decrease of temperature at positions further away from the center of stator. The differences of temperature between inner radius and outer radius were about 40°C. On the other hand, the simulation results showed a slight decrease at constant rate and the overall difference was about 10°C.

4.2.3.2 Rotor-to-stator

In order to determine the stator-to-rotor contact resistance, the corresponding temperature was measured using 6 probes of thermocouple. The measurements were recorded when the heater was operated until the overall temperature reached a steady-state. The probe positions are shown in Figure 4.44. The obtained results are plotted together in Figure 4.45. The temperature closed to the heater area, such as Heater 1 and Heater 2, were very similar. This showed that the temperature distribution between heater and rotor surface was symmetry to the radial direction. Similarly, the temperature distribution on the outer surfaces of stator was also

symmetry. These observations indicated the symmetry of temperature distribution on the diameter plane. Therefore, the simulation model could be simplified by using the symmetric modeling and by using the heat generation boundary condition as a uniform distribution.

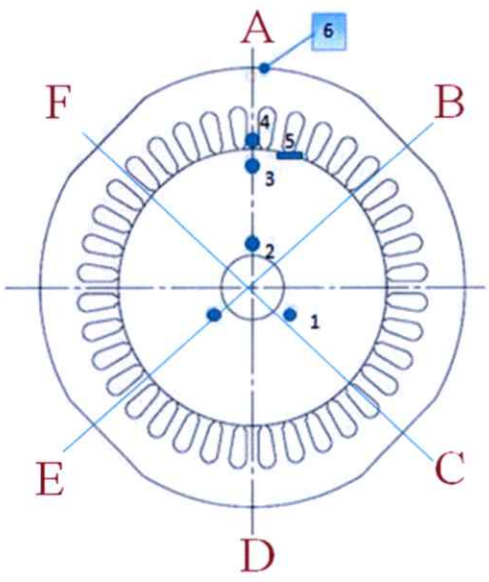

Figure 4.44 Thermocouple positioning on stator and rotor specimen in rotor-to-stator thermal contact resistance experiment

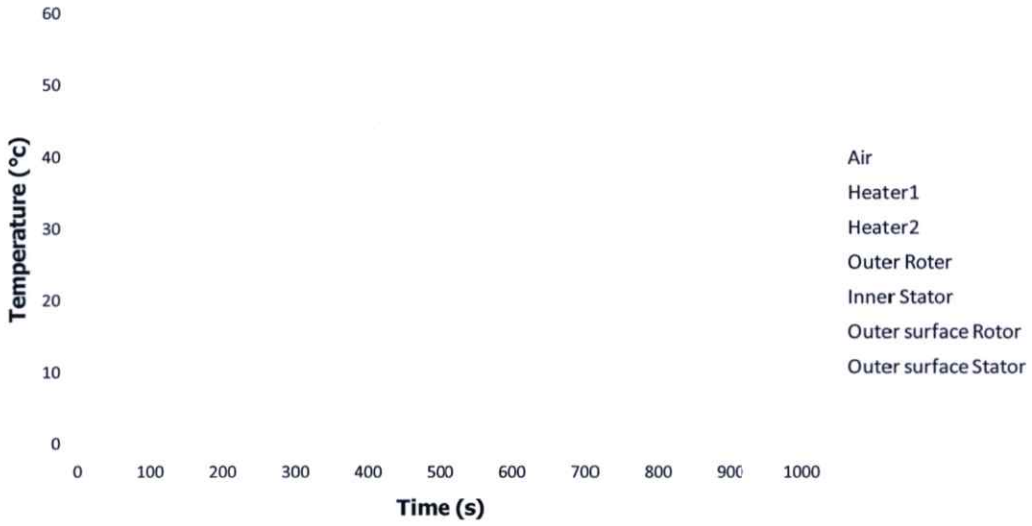

Figure 4.45 Measured temperature variation from the rotor-to-stator thermal contact experiment

Table 4.9 Steady state temperature at measurement locations of rotor-to-stator experiment

Location	A (°C)	B (°C)	C (°C)	D (°C)	E (°C)	F (°C)
1	80.09	77.30	77.66	78.65	79.51	79.65
2	81.22	78.63	78.93	79.88	80.72	81.14
3	76.23	74.0	74.06	74.98	76.21	76.22
4	57.61	58.4	56.63	53.35	52.37	54.0
5	64.57	65.18	66.85	63.02	65.46	61.29
6	44.49	46.05	46.91	46.01	46.10	45.55

4.3 Result of Computation Analysis and Simulation

4.3.1 Simulation of Air Flow in TEFC Motor

The flow regime was a turbulence flow which was assumed to be the K-Ɛ model. As shown in Figure 4.46(a), the air was generated from the tip of the blades and circulated along the tangential direction of fan rotation before flying pass the fan cap exit and along the housing fins. The velocity at the fan cap exit was approximately 15 m/s and decreased rapidly at the position far away from the fan cap exit towards the front portion of motor. Furthermore, a velocity vector plot in Figure 4.46(b) indicated that a movement of the fan drew the surrounding air through the end cap before propelling it onto the housing surface towards the front end of the motor. Inside the housing, the flow was circulated according to the rotation of the rotor fan blades. The internal air velocity was approximately 5 m/s.

Areas of circulating air flow were also determined in the frontal part of the motor. This might explain a relatively high temperature zone observed in this area via the thermal camera (Figure 4.47).

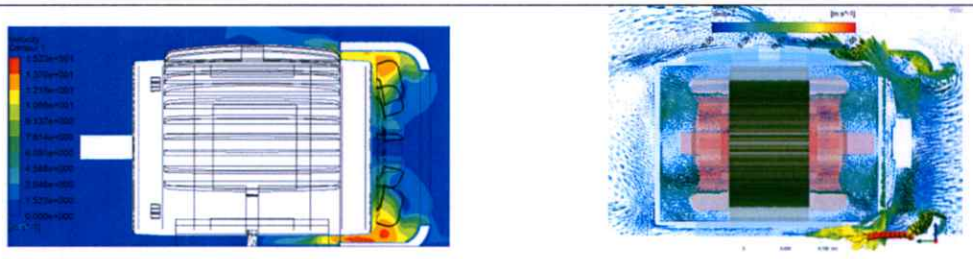

(a) velocity contour (b) velocity vector

Figure 4.46 The computed velocity profile of original motor model

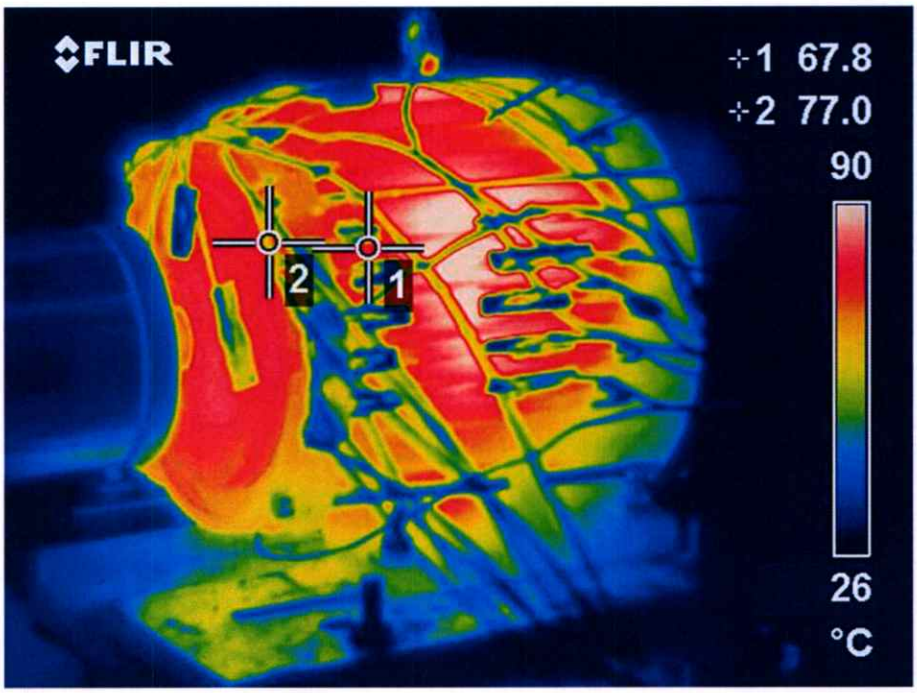

Figure 4.47 The measured temperature of the original model at 100% rated load

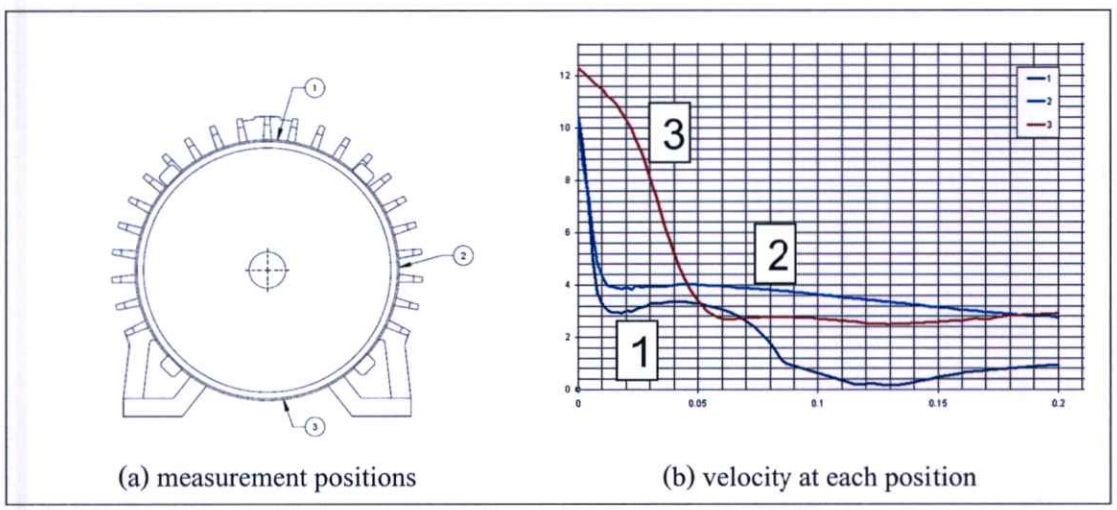

(a) measurement positions (b) velocity at each position

Figure 4.48 The air velocity along the housing between the fins

The profiles of generated air velocity along the housing between the fins from three different locations are displayed together in Figure 4.48. Generally, the air velocity was relatively high coming out from the end cap at the rear side of the housing before rapidly dropping to a much lower value and steadily decline towards a front part of the housing. However, the velocity profile from bottom part of the motor (location 3) seemed to remain high for a longer distance

compared to other locations. This could be due to a tunnel-liked air path that the motor housing formed with the floor. While the velocity profile at the top part of the motor (location 1) displayed another significant dip around half way through the housing. This was most likely because of the presence of a mounting holder for a carrying hook. It effectively acted as an air flow blockage.

4.3.2 Simulation of Heat Transfer in TEFC Motor

4.3.2.1 100 % rated load

The applied heat generation on the rotor, stator core and winding are shown in Figure 4.49. The values of heat generation were the ones measured from the motor efficiency test at 100% workload explained in previous section. In addition, due to the results obtained in section 4.2.3, both thermal contacts were neglected in this simulation. The flow regime was a K-ε model turbulence flow. A simulated temperature distribution of the TEFC motor in a sectioned view is displayed in Figure 4.50. The maximum temperature of around 148 $^{\circ}$C occurred on a front and rear tip of rotor shaft. The trend of temperature was decreasing along the radial distance from the center of rotor shaft to housing.

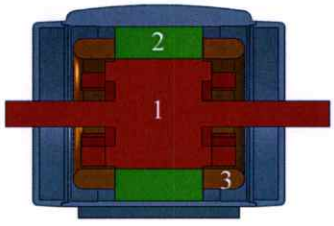

	Motor Component	Heat Generation (W)
1	Rotor	291.81
2	Stator	121.93
3	Copper Winding	396.41

Figure 4.49 Details of heat generation model for heat transfer simulation of motor under 100% rated load

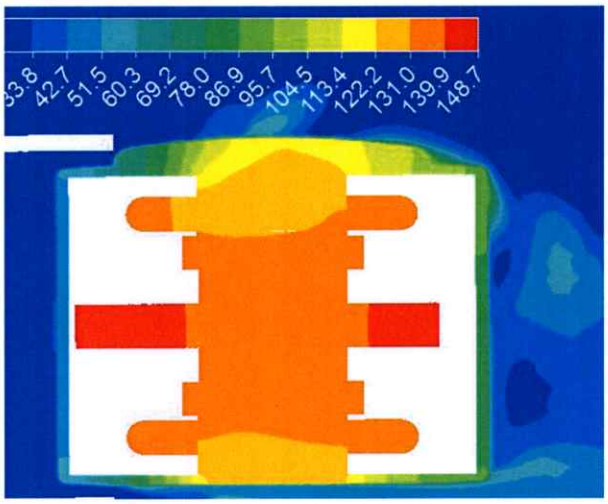

Figure 4.50 Temperature distribution around and inside TEFC motor under 100% rated load

Figure 4.51 shows a temperature distribution on the main housing. There were 4 regions of high temperature appeared in the vicinity of the stator-to-housing contacts. The temperature of housing was in range 50-90 °C. The calculated maximum temperature was 91.65 °C which occurred on the stator-to-housing between motor legs on the bottom part of motor housing.

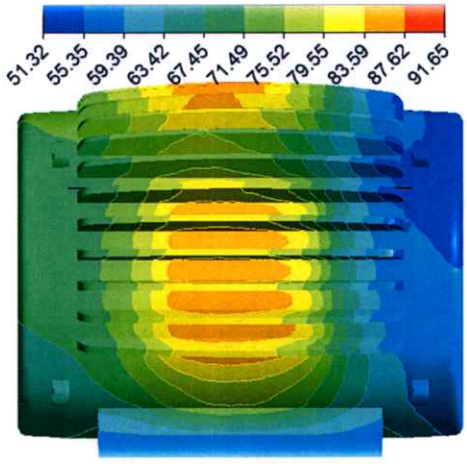

Figure 4.51 Simulation of temperature distribution on main housing surface

The calculated temperature distribution on rotor surface is shown in Figure 4.52. The highest temperature occurred on the front tip of rotor shaft at 148.7 °C. The temperature of the cylindrical surface along the air-gap was within a range of 129 – 135 °C.

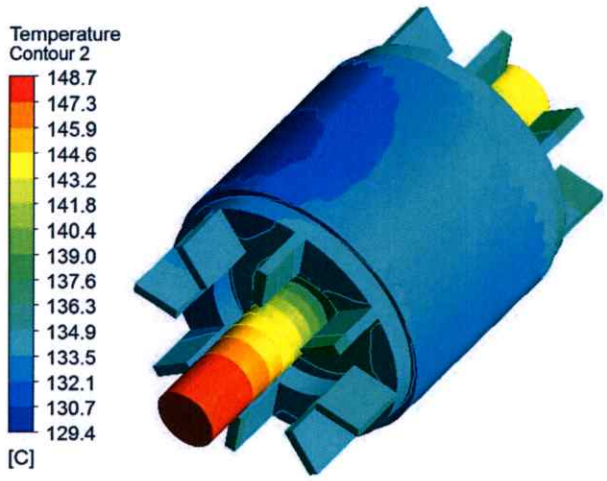

Figure 4.52 Simulated temperature distribution on rotor surface of TEFC Motor at 100% rated load

Figure 4.53 shows the temperature distribution of stator core. The highest temperature occurred on the surface at the tip of teeth where the temperature was around 128-134 °C. The temperature of stator core was in a range of 108 – 134 °C.

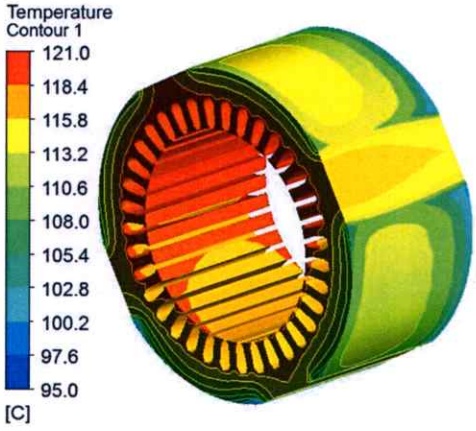

Figure 4.53 Temperature distribution of stator core

Figure 4.54 shows the temperature distribution of copper winding. The highest temperature occurred on the front roll of copper winding at 134°C equal to the maximum of stator core. The temperature of copper winding was in a range of 127-134 °C.

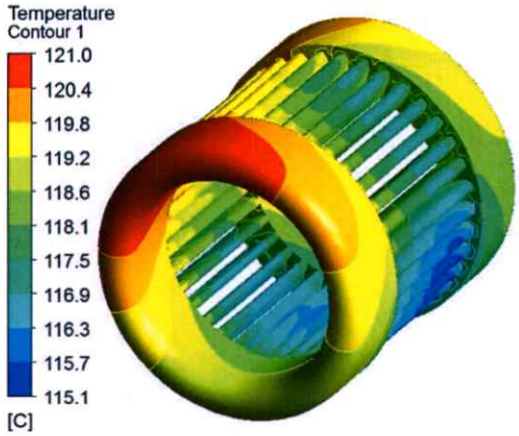

Figure 4.54 Temperature distribution of copper winding

Table 4.10 The temperature results of the simulation of TEFC motor at 100% work load

	Temperature (°C)			
	Rotor	Stator	Copper winding	Housing
Maximum	148.7	133.85	134	91.45
Minimum	129.35	108	127.7	51.35
Average	119	116.675	105	78

4.3.2.2 120 % rated load

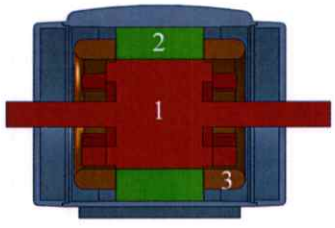

	Motor Component	Heat Generation (W)
1	Rotor	445.5
2	Stator	121.93
3	Copper Winding	556.2

Figure 4.55 Details of heat generation model for heat transfer simulation of motor under 120% rated load

The applied heat generation on the rotor, stator core and winding are shown in Figure 4.55. The heat generation was measured from the motor efficiency testing at 120% work load explained in previous section. The flow regime was turbulence flow which was assumed to

be the K-ε model similar to the simulation of TEFC at 100%. A simulated temperature distribution of the TEFC motor in a sectioned view is displayed in Figure 4.56. The maximum temperature of around 198°C occurred on front and rear tip of rotor shaft.

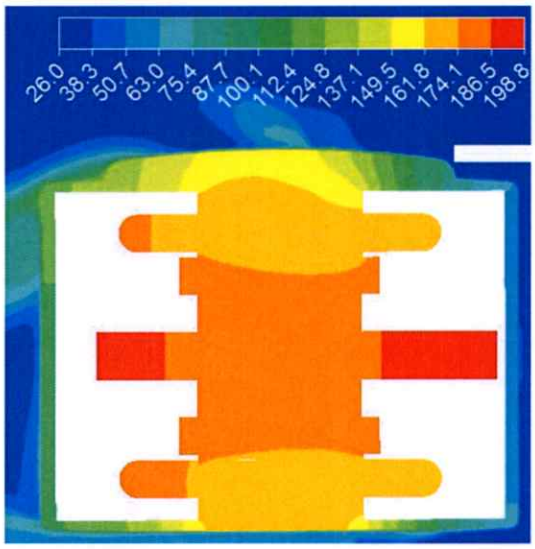

Figure 4.56 Temperature distribution around and inside TEFC motor under 120% rated load

Table 4.11 The results of the simulation of TEFC motor at 120% work load

	Temperature (°C)			
	Rotor	Stator	Copper winding	Housing
Maximum	198.832	175.836	175.874	168.338
Minimum	170.083	147.21	167.227	56.139
Average	184.01	169.747	172.692	118.289

4.3.3 Simulation of Heat Transfer in Liquid Cooling System

4.3.3.1 Liquid Cooling System Design

In an attempt to improve the cooling capacity of TEFC motor, the cooling fan was to be replaced with the liquid cooling system. An advantage of the liquid as a cooling medium is a higher specific heat capacity. However, the system configuration could become more complex than that of the fan cooled system. The liquid cooling system would be comprised of a

radiator, also acting as coolant storage, a coolant pump, a valve, and a motor housing providing a passage for liquid coolant. The schematic of liquid cooling system is shown in Figure 4.57

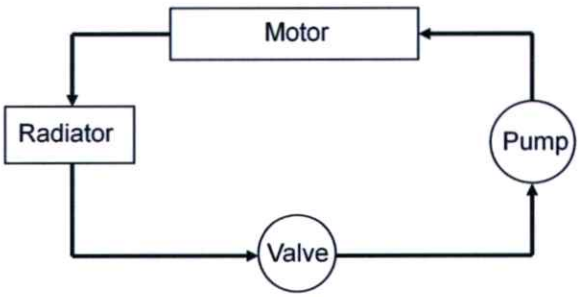

Figure 4.57 Schematic layout of liquid cooling system

The main idea of housing design in this study was to have coolant passages on the motor housing in an axial direction. The cross section of passage was a round hole to simplify the manufacturing process such as by drilling through the housing. The materials of the liquid cooling housing were aluminum due to its advantages regarding specific mass and thermal properties compared to cast iron.

In order to optimize the design of liquid cooling housing, the configurations of the housing were varied by 4 parameters: flow pattern, number of cooling passages, diameter of passages, and coolant flow rate. In this study, there were two types of flow pattern considered i.e. parallel and series flow pattern. Figure 4.58 shows the overall arrangement of housing with parallel and series flow pattern.

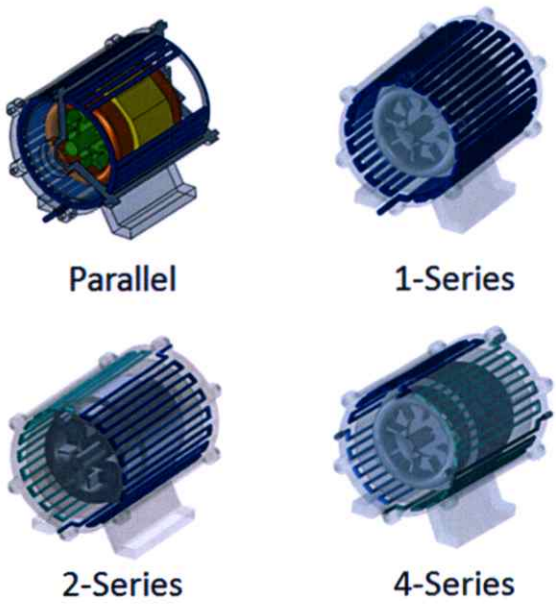

Figure 4.58 General arrangement of housing with parallel and series flow pattern

Figure 4.59 shows coolant flow direction of parallel and series flow pattern. The concept of parallel flow pattern was that the coolant from inlet was evenly distributed to the cylindrical array of coolant passages in the housing. The distribution of coolant flow occurred on the shared passages on end caps. For series flow pattern, the coolant would flow through every coolant passage on housing as a sequence before exiting at the outlet. At the end cap of housing, the coolant flow would need to change direction to return to another passage on housing by the guide-way passages on end caps. The approximated locations of inlet and outlet of the liquid cooled housing are displayed in Figure 4.60.

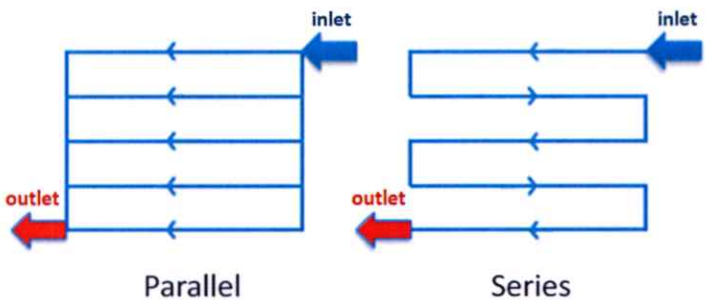

Figure 4.59 Schematics flow pattern of liquid cooling system (left) parallel (right) series

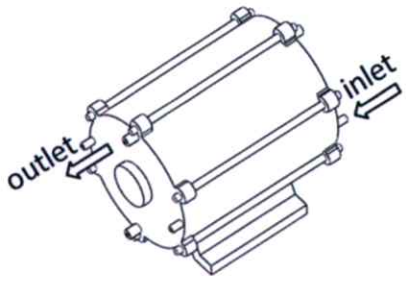

Figure 4.60 Direction and location of inlet and outlet of liquid cooling housing

4.3.3.2 Boundary Conditions

The simulation was calculated at thermal steady-state where equilibrium of heat transfer was satisfied. The overall approach was to replace the TEFC finned housing with the designed liquid cooled housing by keeping the same internal components. As a result, the same heat generation models on the rotor, stator core and winding as those previously used in TEFC simulation were applied. The flow regime was a turbulence state with K-ε model. In order to focus on the cooling performance of the new housing, the convection by air surrounding the external housing surface was assumed to be negligible. The coolant was assigned as a fluid flowing into the cooling passages with the thermal properties as reported in previous section. The inlet coolant temperature was assigned as 45°C according to a typical coolant temperature from a radiator. An outlet pressure was assumed at atmospheric pressure.

4.3.3.3 Simulation Result of Liquid Cooling System

- **Parameter study**

Figure 4.61 shows computational results of the relationship between the maximum temperature of copper winding and the number of cooling passages. This calculation results were based on flow rate of 0.01 kg/s with a parallel flow pattern configuration. The number of cooling passages was varied in a range of 10 – 60 passages. The results indicated that the temperature of copper winding was reduced at a decreasing rate with an increasing number of passages. Additionally, the effect of the passage diameter was studied in this case. There were 2 configurations of passage diameter: 6 mm and 10 mm. The 10 mm of passage diameter yielded a lower temperature than that of the 6 mm of passages in a calculation range of interest. However, there were physical limitations of housing geometry regarding the number of passages and

diameter. Therefore, the chosen configuration should be 50 passages with 10 mm passage diameter.

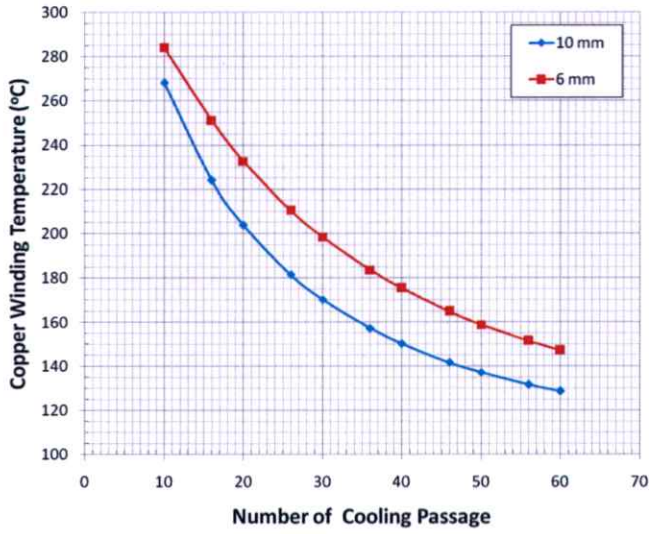

Figure 4.61 Relationship of copper winding temperature and number of cooling passages from simulation

In order to study the effect of the pattern of cooling passage, 4 different types of flow pattern displayed in Figure 4.58 were studied. The general configuration of housing in this case was 40 cooling passages and 10 mm passage diameter. The flow rate was varied in a range of 0.01- 0.5 kg/s with inlet temperature of 60 °C. The results showed all types of series flow patterns performed better than the parallel flow pattern as can be seen from Figure 4.62.

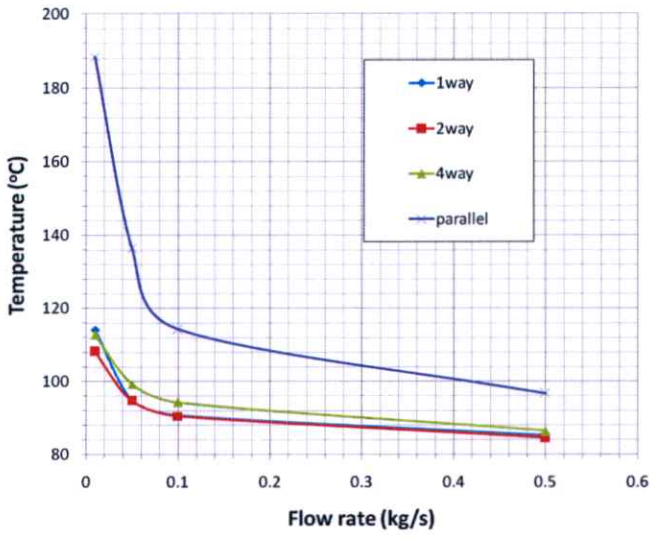

Figure 4.62 Simulated results of copper winding temperature winding against a different flow rate with various flow patterns

With the chosen design point of housing of 50 passages, the effect of flow rate was studied over a range of 0.01 – 0.15 kg/s with an inlet temperature of 45 °C. The analysis also examined 3 different configurations of passages diameter i.e. 6, 8, and 10 mm. The results revealed that the copper winding temperature decreased in an exponential fashion with increasing the coolant flow rate. The effect of the coolant flow rate and the passage diameter to the resulting copper winding temperature is shown in Figure 4.63.

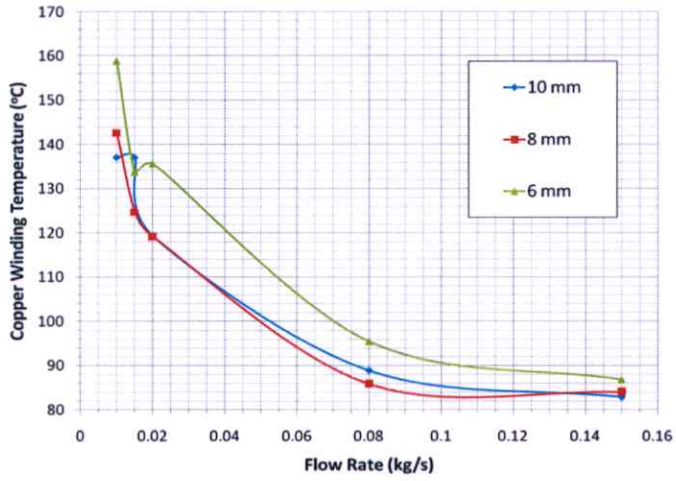

Figure 4.63 Computed correlations between coolant flow rate and copper winding temperature for different coolant passage diameters

- Chosen design point, 100% rated load [Parallel flow, 10 mm ∅, 0.1 kg/s, 50 cooling passages]

After considering the results of parameter study explained in the previous section, the chosen configuration of liquid cooled housing was consisted of the parallel flow pattern, 10 mm of passage diameter, 50 cooling passages, and flow rate of 0.1 kg/s. This chosen configuration was then simulated under the 100% rated load to investigate the resulting temperature distribution and the corresponding cooling capacity in more details. The simulated temperature distribution of the liquid cooling motor on the center half is displayed as a sectioned view in Figure 4.64. The maximum temperature of approximately 106.6 °C occurred on front and rear tip of rotor. Additionally, the temperature of coolant at the outlet was 47 °C which was higher than the inlet temperature by 2 °C.

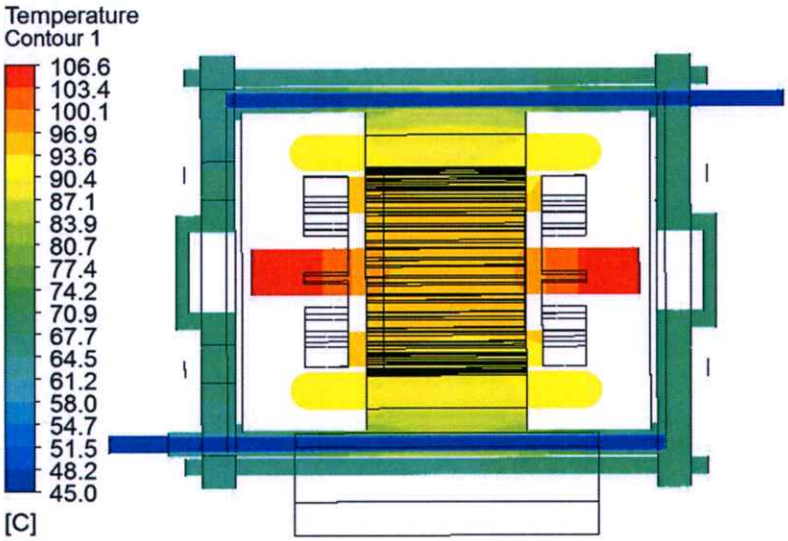

Figure 4.64 Simulation of temperature distribution around and inside of liquid cooling motor at 100% rated load

Figure 4.65 illustrates temperature distribution on the housing surface. Similar to TEFC case, there were 4 regions of high temperature appeared near the contact area between stator-to-housing. The overall housing temperature was in a range of 65-87 °C. The maximum temperature was 86.548 °C occurring on the stator-to-housing between motor legs on the bottom portion of a motor.

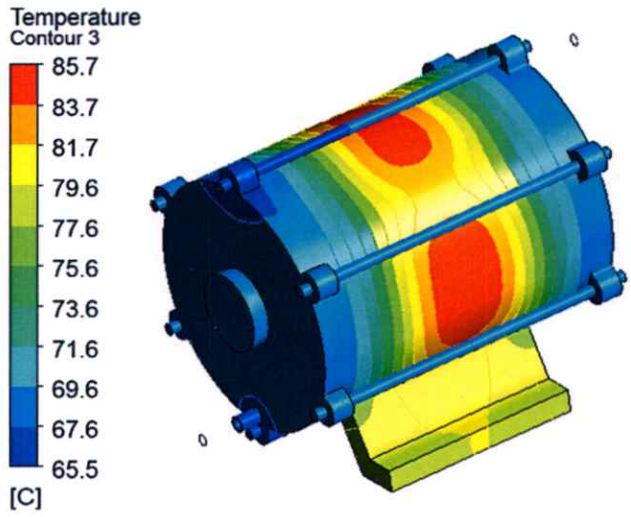

Figure 4.65 Simulated temperature distribution on housing surface of liquid cooling motor at 100% rated load

As the main component regarding temperature damage, the corresponding temperature distribution of a copper winding is displayed in Figure 4.66. The highest temperature occurred on the front portion of copper winding at 92.3 °C which was equal to the maximum temperature of the stator core. Generally, the temperature of copper winding was in a range of 88.8-92.3 °C.

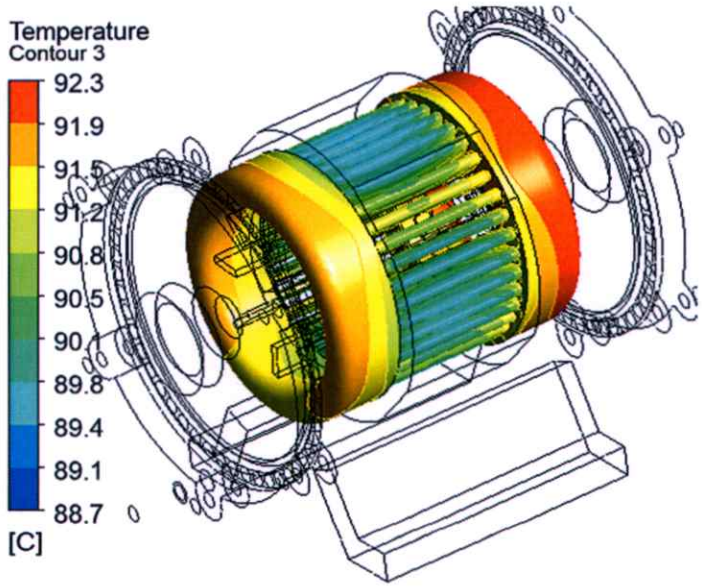

Figure 4.66 Calculated temperature distribution on copper winding surface of designed liquid cooling motor at 100% rated load

Table 4.12 The maximum, minimum and average temperature results of the simulation of liquid cooling motor at 100% work load

	Temperature (°C)			
	Rotor	Stator	Copper winding	Housing
Maximum	106.6	92.333	92.253	86.548
Minimum	90.802	81.429	88.766	65.578
Average	98.289	89.519	90.69	75.4

CHAPTER 5

DISCUSSIONS

5.1 Experiment Results

5.1.1 Temperature Measurement Validation

In order to validate the temperature measurement results, four temperature values were obtained from the thermogram at the surface around the thermocouple probe which was the nearest and the most perpendicular to the infrared camera. These 4 measurement values from thermogram were then averaged and compared with the thermocouple measurement value at the same test duration. The temperature sampling locations from thermogram is shown in Figure 5.1. The comparison results are listed in Table 5.1.

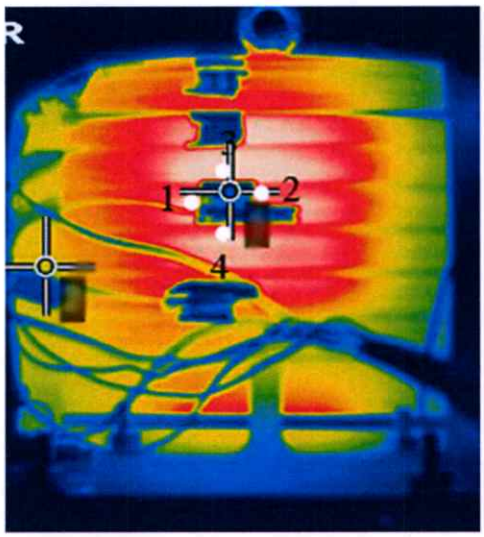

Figure 5.1 Location of thermogram sampling for temperature measurement validation at 100% rated load

Table 5.1 Measured temperature comparison between thermocouple and infrared camera

Motor sample No.#	Experiment No.#	Work Load (%)	IR camera (°C)	Thermocouple (°C)	Difference (%)
1	1	100%	77.825	74.9	-3.76%
	2	150%	147.25	146	-0.8%
2	3	100%	73.6	73.72	0.16%
	4	120%	75.63	70.00	-7.84%

It could be seen from the table that the observed maximum difference was 7.84% for the 120% load experiment. The error might be due to the loosen attachment of thermocouple probe which could reduce the probe sensitivity. However, in general, the comparison results between the thermogram and thermocouple in this measurement was in good agreement. Thus, the measurement results were acceptable.

5.1.2 Measured Temperature Comparison between Different Sample of Motor

In order to compare the resulting temperature between 1st sample and 2nd motor sample at 100% rated load, the common measurement locations on both test motor were considered i.e. SM1, SM3, SM5, SM7, SM8, CM1, and CM2. It could be seen from the comparison shown in Figure 5.2 that both test motors demonstrated a similar trend in the temperature variation throughout the experiment. However, it was observed that the measured temperatures from the housing of 2nd motor were slightly higher than those of the 1st motor at some locations as the test went on. In general, the temperature differences were around 3-5 °C.

Additionally, the corresponding thermogram from each test motor is shown in Figure 5.3 together for comparison. Similar temperature distribution pattern on the main housing could be seen between the two motors. Coupled with a similarity noticed from the efficiency and loss measurement between two motors at 100% load, it could be said that, within the same room temperature, both test motors were subjected to the same forced convection conditions. As a result, this illustrated the repeatability of the observed temperature distribution results to be used as a validating tool for the employed computational model.

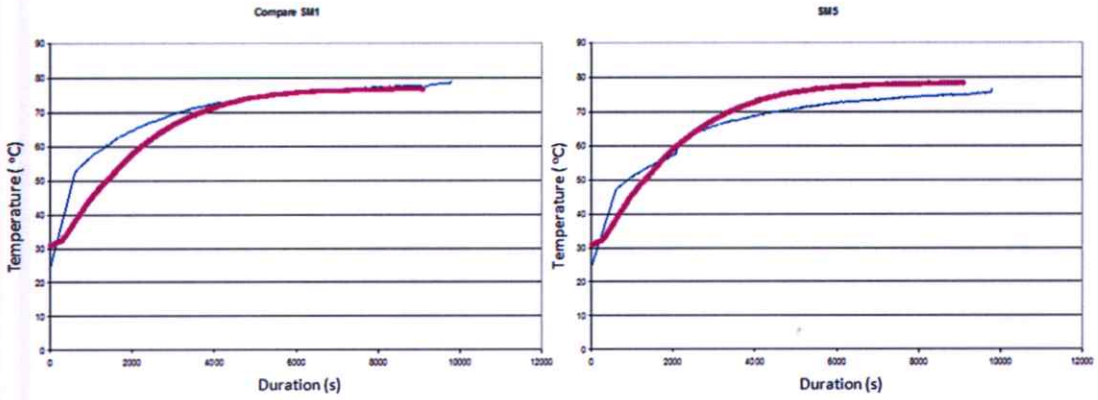

Figure 5.2 Examples of generated temperature comparison between 1st and 2nd motor at 100% rated load at location SM1 (left) and SM5 (right)

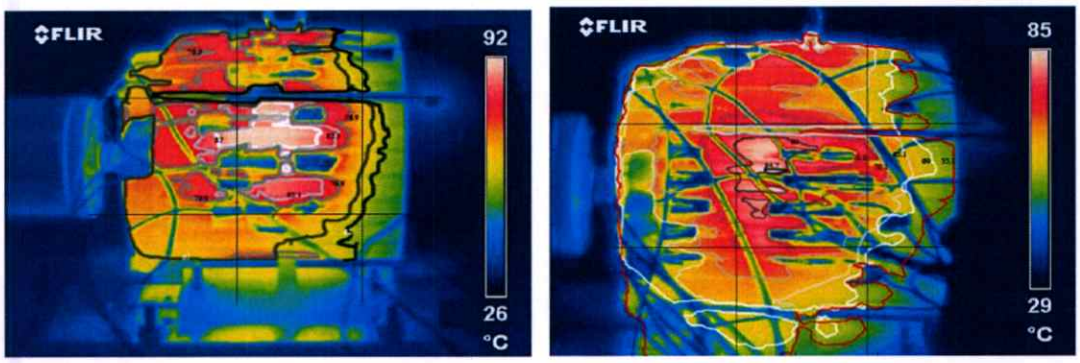

Figure 5.3 Thermogram comparison between 1st (left) and 2nd (right) motor at 100% rated load

5.2 Computational Results Validation

5.2.1 Simulated Results of Air Flow in TEFC Motor Validation

A comparison of resulting temperature distribution on housing surface obtained via computational and by experimental means is shown in Figure 5.4. It could be seen that the computational results displayed a distribution pattern in a similar fashion to that observed in the experiment despite some discrepancies in terms of velocity magnitudes. A good agreement between two sets of results could be clearly seen. Hence, it was reasonable to assume that, in the computational work, the main housing would be subjected to the forced convection similar to that occurred on the actual case, and that the suitable temperature distribution on the housing could be calculated providing that the appropriated amount of heat was applied to the housing.

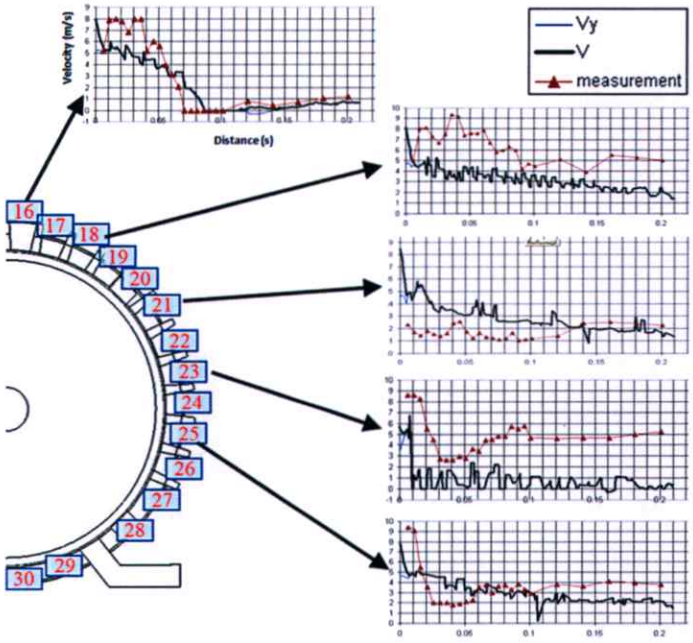

Figure 5.4 Results comparison of air velocity along the fin panel of TEFC motor

5.2.2 Simulated Results of Temperature Validation

The principle of an induction motor is based on a use of a magnetic field, which is generated by stator winding, to induce the magnetic property of rotor. Consequently, the effect of the magnetic field also induces the heat generation of rotor. A rotor shaft also gets the effect of magnetic fields. Therefore, the magnetic fields also effectively induce a heat generation to the rotor shaft.

The measurement of rotor loss is determined from the measurement of motor slip by the equation (3.3). However, the distribution of rotor loss cannot be determined by this equation. It might probably occur on rotor and rotor shaft due to it magnetic properties. In order to simplify the simulation of the motor heat transfer in this study, the heat generation model of rotor was assigned as a uniform distribution over both rotor and shaft component.

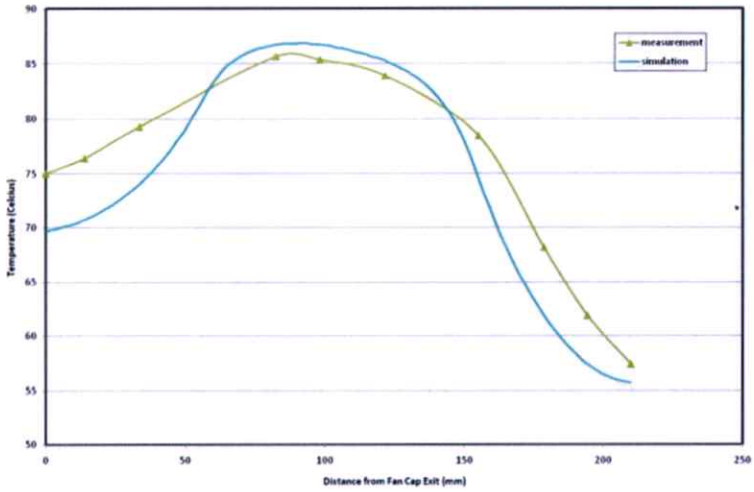

Figure 5.5 Comparison of temperature distribution along the fin panel between measurement and simulated results

By assigning this heat generation model, the simulated results of temperature distribution on external surface displayed the same trend after a comparison with the measurement. Figure 5.5 shows the temperature distribution along the fin panel on the housing surface. The temperature was relatively highest around the middle portion of the housing while decreasing in both directions away from the middle area with the front portion at higher temperature than the rear portion. Figure 5.6 shows the overall comparison of resulting temperature distribution on the housing surface. The appearance of temperature distribution was also in a good agreement. The differences between simulated results and measured results were around 3-5 $^{\circ}$C or 6.4 % with the computational model under predicting the results on the front and rear portion of the main housing.

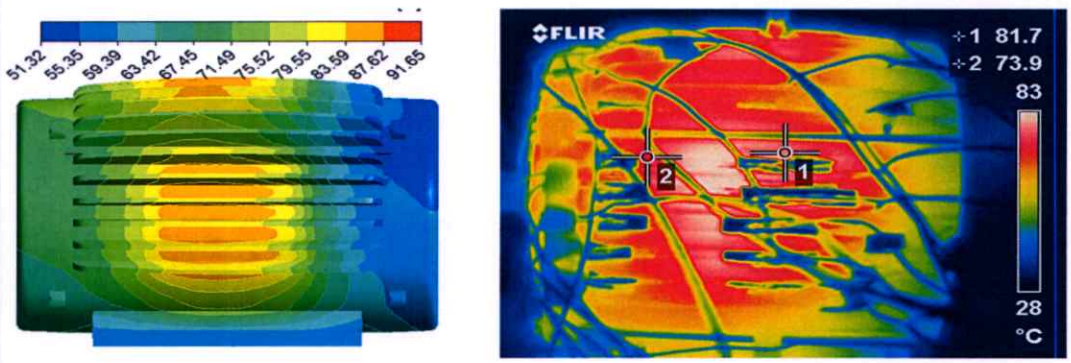

Figure 5.6 Temperature comparison between simulation and measurement of 100% rated load TEFC motor

Furthermore, the simulated result of the internal components temperature is showed in Figure 5.7. There were large differences on both tips of the rotor shaft comparing with the measurement. It was believed that this high temperature concentrated on the tips of shaft was because of the heat generation value also being applied to a rotor shaft in the simulation.

It was considered that the rotor shaft was a portal to partially transfer the heat from the rotor in an axial direction. Thus, the shaft was kept in the whole model in an attempt to allow an appropriate amount of heat going into the housing i.e. radial direction. Originally, it was intended to model the rotor shaft extending to the outside and came into contact with the housing at both end of shaft. However, with the rotation of rotor taken into account, the additional interfaces between shaft and housing increased the complexity of the calculation and no result convergence was achieved. As a result, the model of the shaft had to be cut at both ends to omit the interface with the housing.

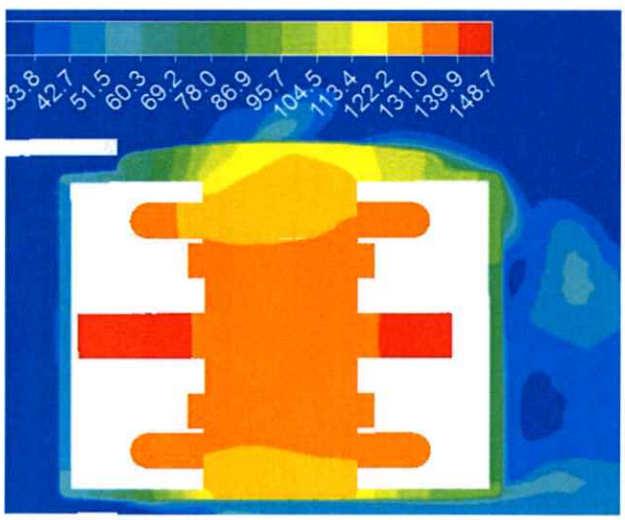

Figure 5.7 Simulated result of internal of TEFC motor 100% workload at steady state

The simulation result in Figure 5.7 shows that the temperature was high at both tips of shaft region. This could be because there was no interface on the shaft to the housing. According to the measurement results in Figure 5.8 the front-end cap was one of high temperature regions observed during the test. The highest temperature of this area was nearby the rotor shaft. This indicated that the shaft temperature did get rather high during the motor operation.

However, when considered that the main focus of the study was on the heat transfer of the main housing body i.e. force convection on the finned housing, the housing temperature

distribution comparison between experiment and simulation did show a good agreement as seen in Figure 5.5 and Figure 5.6. This indicated that the appropriate amount of generated heat assigned to those internal components has been conducted to the main housing body. This included the heat from the copper winding which would preferably travelled through a stator core to the main housing body where the heat would be convected away by airflow from the rear fan. Therefore, it was strongly believed that the resulting temperature of the copper winding would not be significantly affected by such model arrangement of the rotor shaft.

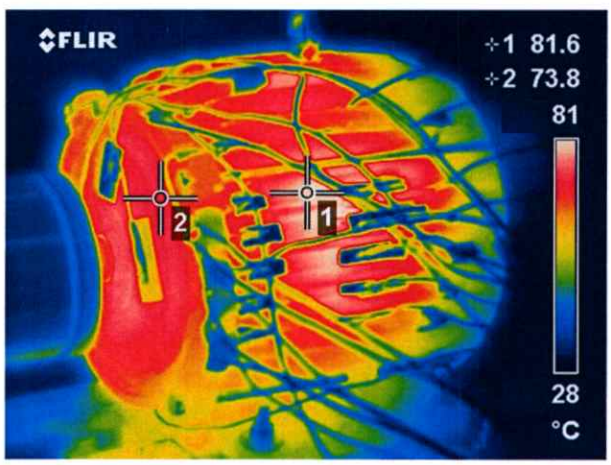

Figure 5.8 Measurement of TEFC motor 100% work load before steady-state

5.3 Contact Resistance

5.3.1 Stator-to-Housing Contact

According to comparison results of temperature profile between the experiment and simulation in Figure 4.43. The simulation results were higher than the measurement results with a significant difference. There might be some errors in temperature measurement because the measurement was performed by infrared camera, which could only measure temperature on surface. There could be a natural convection by surrounding air, which would reduce temperature on surface. Therefore, the temperature measurement method in this particular test could not determine the stator-to-housing contact resistance. The temperature measurement should be performed with probes inserted into the center of body in order to neglect the effect of convection on surface.

Nonetheless, by initial inspection, the stator was inserted tighten into the inside diameter of the housing. The 2 surfaces of stator and housing were in contact under a high

compression condition. Thus, it was reasonable to assume that the corresponding contact resistance would be rather low. On the other hand, the rotor-to-stator contact was an air-gap with 0.32 mm width. Therefore, the stator-to-housing contact resistance should be much less than that of the rotor-to-stator contact.

5.3.2 Rotor-to-Stator Contact

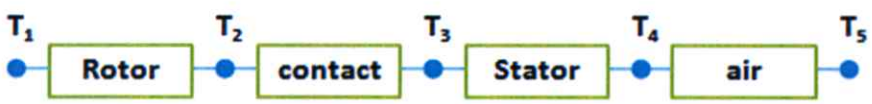

Figure 5.9 One-dimensional model of rotor-to-stator heat transfer

From the diagram in Figure 5.9, the conduction equation in a cylindrical coordinate could be presented as shown below in equation (5.1)

$$q = \frac{2\pi Lk(T_1 - T_1)}{\ln(r_2/r_1)} \tag{5.1}$$

Where L is length of rotor in axial direction $= 0.095\ m$, k is thermal conductivity of rotor $= 60\ W/m \cdot K$, $r_1 = 0.014\ m$, $r_2 = 0.06\ m$. These values yielded a result of $q = 60.35\ W$.

By applying $q = 60.35\ W$ to calculate the rotor-to-stator contact resistance, the result was

$$R_{rotor-motor} = 0.074\ K \cdot m^2/W \tag{5.2}$$

After applying this result to the TEFC 100% workload simulation, the result of temperature in rotor would be higher than 200 °C. In this case, there was an even larger difference of rotor temperature between the measurement and simulation.

However, there have been several studies of a traditional empirical method to calculate the average heat transfer coefficient in an air-gap of electric machine by using Nusselt number [Saari 1995]. The air-gap was considered as a channel between concentrated cylinders and its Nusselt number could be expressed as

$$Nu = \frac{h\delta}{k_f} \tag{5.3}$$

where δ is the radial air-gap length, h is the heat transfer coefficient for one air-gap surface (rotor or stator) and k_f is the thermal conductivity of the fluid.

The rotating rotor forced the fluid to a tangential movement and induced toroidal vortices. This toroidal movement was referred to as the Taylor-vortex flow. The flow in the air-gap was different compared to the flow between two parallel plates. The Taylor vortices could be described using the Taylor number

$$Ta = \frac{\rho^2 \omega^2 r_m \delta^3}{\mu^2} \tag{5.4}$$

where ω is the angular velocity, r_m is the averaged value of the stator and rotor radius. In this study, the corresponding Taylor number could be calculated to 1.22×10^{-1}.

Furthermore, the modified Taylor number, which takes into account the rotor radius and the radial air gap length, was needed in this calculation.

$$Ta_m = \frac{Ta}{F_g} \tag{5.5}$$

where F_g is the geometrical factor defined by

$$F_g = \frac{\pi^4}{1697(1-\frac{\delta}{2r_m})^2 P_g} \tag{5.6}$$

where

$$P_g = \frac{0.0056+0.00571(\frac{2r_m-2.304\delta}{2r_m}-\delta)}{(\frac{2r_m-2.304\delta}{2r_m-\delta})} \tag{5.7}$$

The results from these equations are $P_g = 6.62 \times 10^{-2}$, $F_g = 8.72 \times 10^{-1}$ and $Ta_m = 2.43 \times 10^{-1}$

There have been several studies about the heat transfer in the air gap. The Nusselt number in the air gap has been measured by many researchers, for example [Gazley, 1958], [Becker et al., 1962], etc. Aoki et al. (1967) proposed the correlation regarding the air gap flow depended on the modified Taylor number as shown below

$$Nu = 0.44 {Ta_m}^{0.25} Pr^{0.3} \tag{5.8}$$

Since the calculated modified Taylor number for the present study was 2.43×10^{-1}, the corresponding Nusselt number was found to be 0.241 according to equation (5.8). Then, in order to calculate the average heat transfer coefficient of the air-gap, the thermal conductivity of air of $0.029\ W/m \cdot K$ was employed. Thus, the calculated of the average convective heat transfer coefficient was found to be

$$\bar{h} = 228\ W/m^2 \cdot K \tag{5.9}$$

With the above heat transfer coefficient, the rotor-to-stator contact resistance was determined to be $0.0044\ W/m^2 \cdot K$. Thus, it could be seen that by taking into account the effect of rotational movement, the corresponding contact resistance between rotor and stator was greatly reduced by a factor of 16.8. As a result, a trial study was made such that the contact resistance was ignored from the computational model in order to simplify the simulation process further. Mainly, it was found that the resulting temperatures on stator and housing were in good agreement with the experimental ones. Hence, this indicated that the assumption made about the contact resistance was applicable for the computational model employed in this study.

5.4 Design of Liquid Cooling System

According to the preliminary results shown in the previous chapter, the 50-passages configuration of liquid cooled housing was chosen to optimize the proper passage diameter and coolant flow rate. The simulations were based on 45 °C of the coolant temperature at inlet and the heat generation at 100% workload. The response surface approach was applied to obtain the optimized design of liquid cooled housing. The flow rate was calculated in a range of 0.08 - 0.15 kg/s regarding the pump capacity. The results from Figure 4.63 show the distribution of temperature results in a range of 0.08 - 0.15 kg/s could be matched with the 2nd order polynomial distribution of response surface. The general equation of 2nd order polynomial distribution could be expressed as:

$$y = \beta_0 + \beta_1 x_1 + \beta_2 x_2 + \beta_3 x_1^2 + \beta_4 x_2^2 + \beta_5 x_1 x_2 \tag{5.10}$$

where y was simulated results of maximum temperature of copper winding

x_1 was parameter of passage diameter (mm)

x_2 was parameter of coolant flow rate (kg/s)

The coefficient of the 2nd order polynomial equation (β) could be obtained from following equation:

$$\beta = (\mathrm{X^T X})^{-1} \mathrm{X^T Y} \tag{5.11}$$

In order to interpolate the response surface of the simulated results, 9 points of the simulated results in different configuration of housing were used. Table 5.2 shows the design points using for the response surface calculation.

Table 5.2 Design points for response surface of liquid cooled housing

		x_2		
		0.08 kg/s	**0.115 kg/s**	**0.15 kg/s**
x_1	**6 mm**	95.434	85.839	86.762
	8 mm	85.85	87.75	84.037
	10 mm	88.842	88.842	83.53

All design points could be arranged in a matrix and calculate the β by using equation (5.11). Therefore,

$$X = \begin{bmatrix} 1 & 0.06 & 0.08 & 0.06^2 & 0.08^2 & 0.0048 \\ 1 & 0.06 & 0.115 & 0.06^2 & 0.115^2 & 0.0069 \\ 1 & 0.06 & 0.15 & 0.06^2 & 0.15^2 & 0.0090 \\ 1 & 0.08 & 0.08 & 0.08^2 & 0.08^2 & 0.0064 \\ 1 & 0.08 & 0.115 & 0.08^2 & 0.115^2 & 0.0092 \\ 1 & 0.08 & 0.15 & 0.08^2 & 0.15^2 & 0.0120 \\ 1 & 0.10 & 0.08 & 0.10^2 & 0.08^2 & 0.0080 \\ 1 & 0.10 & 0.115 & 0.10^2 & 0.115^2 & 0.0115 \\ 1 & 0.10 & 0.15 & 0.10^2 & 0.15^2 & 0.0150 \end{bmatrix} \quad Y = \begin{bmatrix} 95.434 \\ 85.839 \\ 86.762 \\ 85.850 \\ 87.750 \\ 84.037 \\ 88.842 \\ 82.833 \\ 83.530 \end{bmatrix} \tag{5.12}$$

The results were:

$$\beta = \begin{bmatrix} 0.1550 \\ -0.7760 \\ -0.5346 \\ 3.3192 \\ 1.5797 \\ 1.2000 \end{bmatrix} \times 10^3 \tag{5.13}$$

Therefore, the distribution equation of the designed housing was:

$$\begin{aligned} y \quad = \quad & (1.55 \times 10^2) - (7.76 \times 10^2)x_1 - (5.346 \times 10^2)x_2 \\ & +(3.3192 \times 10^3)x_1^2 + (1.5797 \times 10^3)x_2^2 + (1.2 \times 10^3)x_1x_2 \end{aligned} \tag{5.14}$$

Figure 5.10 shows the calculated results according to equation (5.14). The results were represented in a form of response surface. The top corner into the page was the group of results with the highest copper winding temperature and the bottom corner nearer to the reader was the group of results with the lowest copper winding temperature.

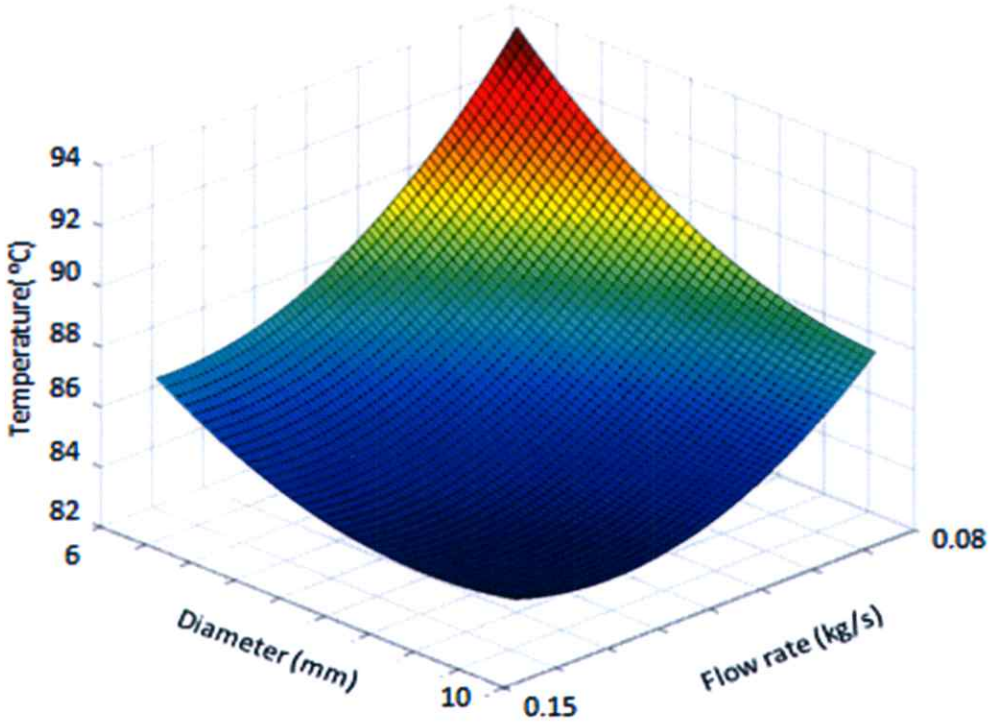

Figure 5.10 Calculated 2nd order polynomial response surface of liquid cooled housing design

The target of the optimization process was to obtain the design points, which gave the minimum temperature of the stator copper winding. After a group of design points was obtained from the calculated response surface i.e. the near bottom corner area in Figure 5.10, a further selection of a final design point from this group was based on the size of coolant storage required. For an example of passage diameter 10 mm, the minimum temperature was 84.889 °C at 0.1 kg/s, while it was 83.886 °C at 0.15 kg/s. It could be seen that in order to reduce a copper winding temperature by 1 °C, the coolant flow rate had to be increased by 0.05 kg/s. Therefore 0.1 kg/s was the better choice than 0.15 kg/s in this case.

5.5 Motor Cooling Capacity

5.5.1 TEFC Cooling Capacity Calculation

In order to simulate the heat transfer of TEFC motor, the heat transfer system was included with 5 solid bodies such as rotor, stator core, copper winding, housing, and external air. The equation of conservation of energy of TEFC motor could be simplified as followed:

$$Q_{Gen} = Q_{\Delta T} + Q_{cooling} \tag{5.15}$$

These are 3 important terms related to the heat transfer on TEFC motor. First term is the heat generation from TEFC motor (Q_{Gen}). This term could be obtained from the result of losses from the motor efficiency measurement. Under an assumption that all losses of motor were presented as the heat generated at motor, the heat generation of motor was:

$$Q_{Gen} = \tau \sum P_{loss} \tag{5.16}$$

where P_{loss} was the summation of rotor, stator, and copper loss. (W)

t was the duration to reach steady state. (s)

The duration for steady state (t) was obtained by a differential of temperature by time. Figure 5.11 shows the results of derivative of temperature against duration from temperature measurement. The duration at 5800 s where the derivation of temperature equaled to zero marked an onset of a steady state.

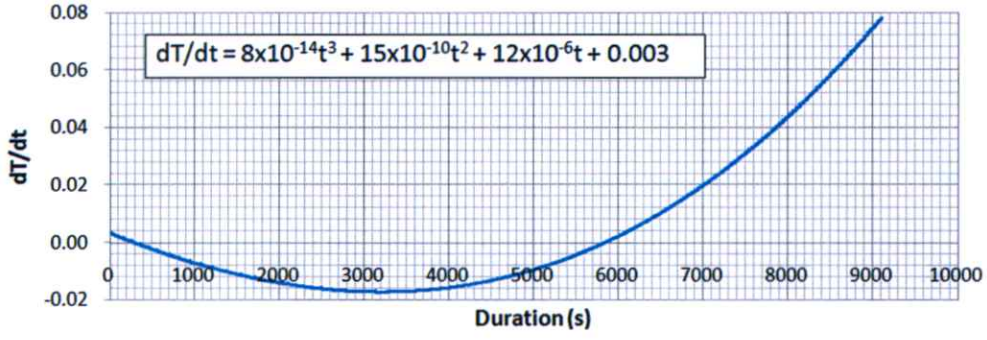

Figure 5.11 Correlation of derivative of temperature against duration of TEFC motor at 100% work load

The 2nd term of equation (5.15) was the term of specific heat capacity of materials. This term represented the heat used to raise the temperature of material i.e. motor. In this case, all components of motor were assumed to be uniform body. Therefore, the specific heat capacity (c_p) was recognized as uniform. The temperature of motor components was obtained from the average temperature in each component. From those values, this term could be calculated from equation:

$$Q_{\Delta T} = \sum m c_p \Delta T \tag{5.17}$$

Table 5.3 Calculated results of specific heat (equation 5.17)

Component	$Q_{\Delta T}$ (MJ)
Rotor	0.488
Stator Core	0.424
Copper Winding	0.442
Housing	0.515
Result (Total)	**1.829**

The 3rd term ($Q_{cooling}$) was the heat dissipated from motor by the cooling system. This term was unknown regarding to the unknown of air quantities. In this case, this term could be calculated from the known 1st and 2nd term of equation (5.15). The cooling rate of TEFC motor ($P_{cooling}$) could be calculated from the quantity of heat dissipated from motor by equation:

$$P_{cooling} = \frac{Q_{cooling}}{\tau} \tag{5.18}$$

The calculated resulted of cooling capacity of TEFC motor from the start of motor to steady state was 2.83 MJ regarding to equation (5.15). Hence, the corresponding cooling rate of TEFC motor was 464.15 W regarding to equation (5.18).

5.5.2 Cooling Capacity of Liquid Cooled System

The simulation of liquid cooled housing was assumed to exclude the convection of surrounding air and the heat transfer to the mounting on legs. The cooling rate (W) of liquid cooled system could be calculated relating to a specific heat capacity of a coolant.

$$P_{cooling} = \dot{m}c_p(T_{out} - T_{in}) \tag{5.19}$$

At the chosen design point of 50 passages, 10 mm ∅, 0.1 kg/s flow rate, 45 °C at inlet, with 100% work load, the simulated result of outlet temperature was 47 °C. By using those parameters, equation (5.19) yielded a cooling rate of liquid cooled system at 540 W.

In case of the liquid cooled motor operating for 5800 s according to the steady state of TEFC motor, the calculated cooling capacity of liquid cooled system was approximately 3.13 MJ.

Table 5.4 Comparison of TEFC system and liquid cooling system

Cooling System	Copper winding Maximum Temperature (°C)	Cooling Capacity @ 5800 s (MJ)
TEFC	118.543	2.83
Liquid Cooled	92.333	3.13

In order to maintain the temperature of motor as in TEFC motor at 100% workload, temperature at outlet was assumed to be 47 °C, the chosen design of liquid cooled system could be operated on this motor with total loss as 869.14 W. According to Figure 5.12, this new motor could at least operate at 105 % workload of the original TEFC motor in order to generate the 869.14 W of total loss.

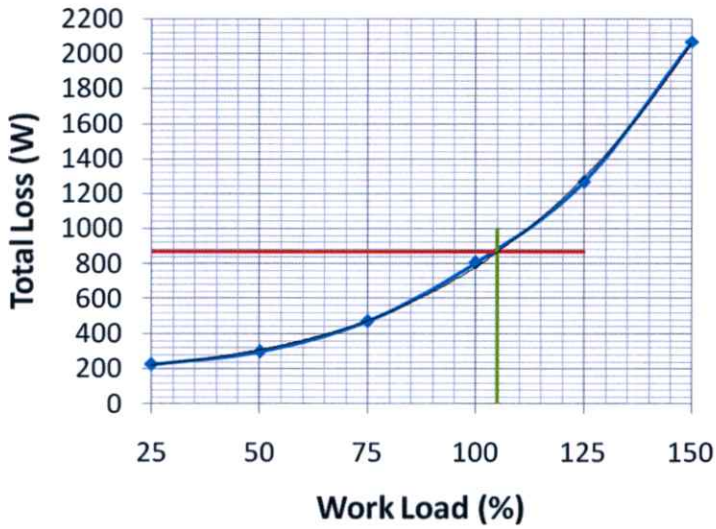

Figure 5.12 Correlation of total loss of motor against workload

However, this estimation above was based on outlet temperature at 47 °C. In fact, the outlet temperature could be higher than 47 °C because the overall temperature of motor at 105% work load could be higher than at 100% workload. Figure 5.13 and Table 5.5 show the simulated results under the 120% work load. As the results of 120% work load, the simulated maximum temperature of copper winding was 117.03 °C which was still less than the critical temperature of class F insulator. This indicated that the new liquid cooled motor could comfortably cope with a higher workload than 120%.

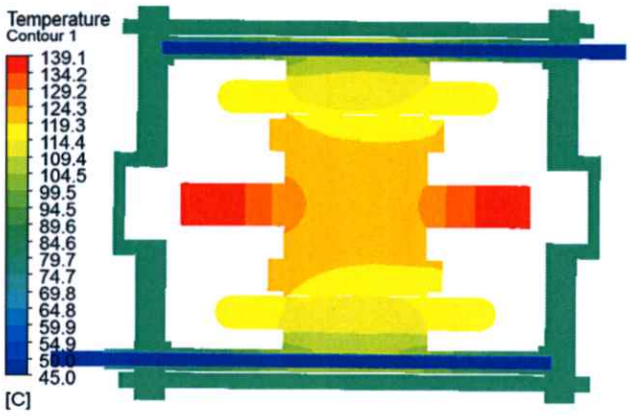

Figure 5.13 Simulated result of liquid cooled motor at 120% workload

Table 5.5 Summary of simulated results of temperature of liquid cooled motor at 120% rated load

Component	Rotor	Stator	Housing	Copper winding	Outlet
Maximum (°C)	139.15	117.25	109.24	117.03	
Average (°C)	126.43	113.15	92.51	114.69	49
Minimum (°C)	115.22	101.41	77.42	111.97	

Additionally, the simulated results of liquid cooled motor under work load at 100%, 120%, and 150% yielded the maximum temperature of copper winding of 92, 117, and 178 °C respectively. Thus, in order to work out a capable practical workload of the proposed liquid cooled motor, a correlation of the maximum temperature of copper winding against workload of the developed motor was expressed in a binomial format shown in Figure 5.14. It could be seen from Figure 5.14 that the liquid cooled motor could operate at approximately 140% under the condition that the resulting copper winding temperature did not exceed a class F insulator limit of 155 °C.

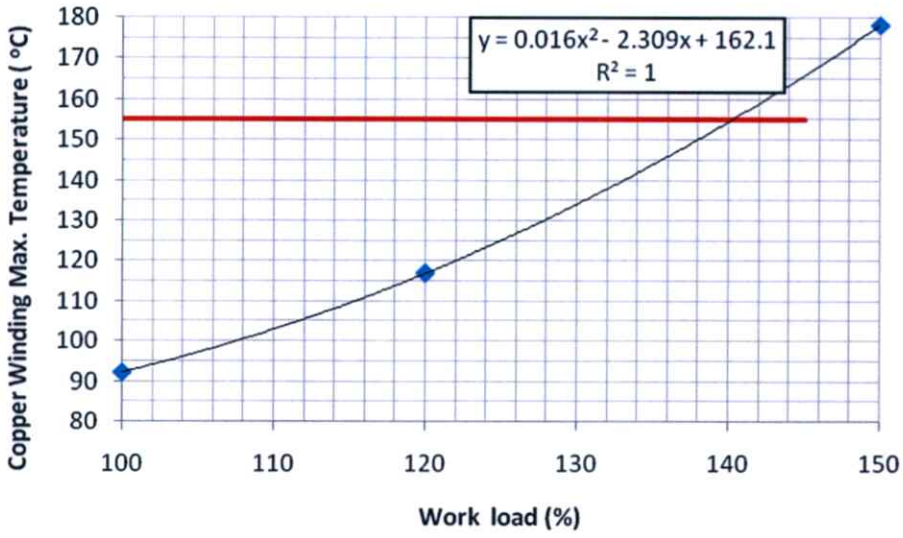

Figure 5.14 Correlation of the maximum temperature of copper winding and workload of liquid cooled motor

In order to maintain the temperature of cooper winding at 155 °C under 140 % rated load, the cooling rate should be more than 1720 W regarding to Figure 5.15. The calculated coolant temperature at outlet could be was 51.37 °C.

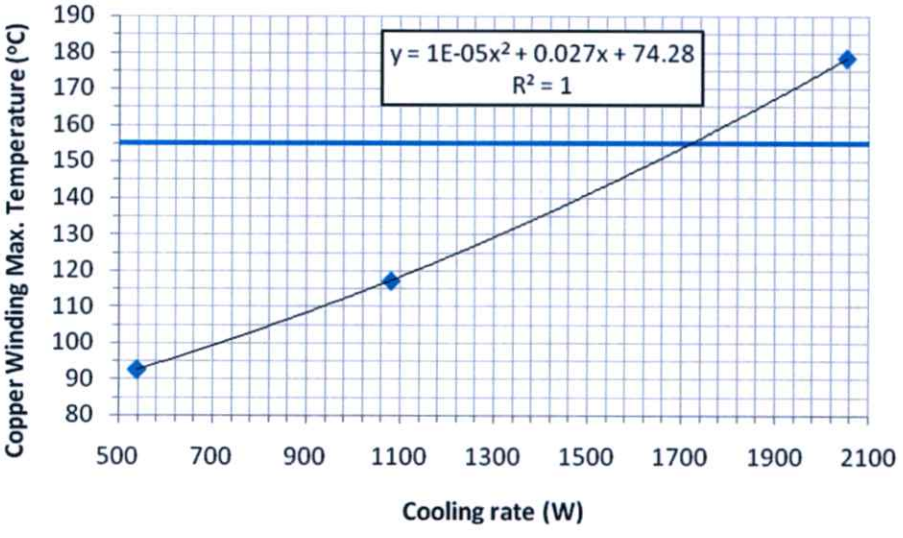

Figure 5.15 Correlation of the maximum temperature of copper winding and cooling rate of liquid cooled motor

CHAPTER 6

CONCLUSIONS

The main objectives of this study were to obtain the heat generation model of an induction motor, and to develop liquid cooling system to replace a conventional Totally Enclosed Fan Cooled (TEFC) system with an improved motor cooling capacity. When operated over the specific load, the induction motor would be damaged due to the high temperature causing a melting of electrical insulator on copper winding, and a short circuit of motor.

The study of heat generation model of an induction motor was attempted on 3.7 kW, 3-phases, TEFC motor. The heat generation of motor was obtained by means of losses of motor, which were measured by the motor efficiency measurement under IEEE-112 standard. The temperature of motor was measured under the various loads at 100%, 120%, and 150% of rated load assigned by a dynamometer. The experimental temperature results were measured using an infrared camera and thermocouples for comparative validation of the computational simulation.

Furthermore, 2 locations of thermal contact were studied i.e. stator-to-housing and rotor-to-stator thermal contact. The experimental results of losses and thermal contact resistances were applied in order to simulate the heat transfer phenomenon of TEFC motor at steady-state. The simulated results were validated by the measured housing temperature distribution from the experiment. The steady-state heat transfer simulation of TEFC motor could be described with the heat generation model of an induction motor. The developed computational model of TEFC motor was validated by means of resulting temperature distribution comparison.

The validated heat generation model was further used in designing a liquid cooling system. The new liquid cooling system was comprised of radiator, pump, and liquid cooled housing. This new system was a closed circuited system using the special heat transfer oil ($c_p = 2.7$ J/g.°C) as a coolant. In order to design the liquid cooled housing, the number of passages, flow pattern and flow rate were the factors considered. The liquid cooled housing was then optimized by the Response Surface approach. The conventional TEFC motor and the proposed liquid cooled motor design were compared by means of a cooing capacity. Finally, the capable working capacity of the proposed liquid cooled motor was estimated under a criterion of keeping the temperature of copper winding under the critical temperature of insulator.

In the previous chapters of this thesis, the study of heat transfer in TEFC motor and the details of liquid cooling system development have been reported and discussed. The main conclusions of this study were as follows:

- The important heat sources of an induction motor were in rotor, stator, and copper winding. The quantity of heat generation in each component was applied as a uniform distribution.
- Both thermal contact resistances could be neglect for the heat transfer simulation of an induction motor in this study.
- By the Response Surface approach, the chosen design point was comprised of 50 passages, 10 mm ∅, and parallel flow pattern at 0.1 kg/s flow rate. The proposed liquid cooling system could keep the temperature of copper winding at 90°C under 100% workload of studied TEFC motor.
- Motor capacity with the liquid cooling system was calculated to increase to at least 20% of rated workload of conventional TEFC motor. In order to keep the temperature of copper winding under the critical temperature of insulator (155°C), the motor capacity could be increased by approximately up to 40% of the rated workload of conventional TEFC model.

REFERENCES

[1] AIEE. 1956. "Test procedure for evaluation of systems of insulating materials for random-wound electrical machinery." **AIEE 510.**

[2] ANSYS CFX. 2012. **CFX-Solver Reference Guide.** Version 14.

[3] Aoki, A. Nohira, H. and Arai, H. 1967. "Convective Heat Transfer in an Annulus with an Inner Rotating Cylinder." **Bulletin of J.S.M.E.** vol.10 : 523-532.

[4] Becker, K.M. and Kaye, J. 1962. "Measurements of Diabatic Flow in an Aunulus with an Inner Rotating Cylinder." **Transactions of the ASME, Journal of Heat Transfer.** vol.84 : 97-105.

[5] Bellettre, J. Sartre, J. Biaist, F. and Lallemand, A. 1997. "Transient State Study of Electric Motor Heating and Phase Change Solid-Liquid Cooling." **Applied Thermal Engineering.** 17 (1) : 17-31

[6] Bjorklund, I.S. and Kays, W.M. 1959. "Heat Transfer between Concentric Rotating Cylinders." **Transactions of ASME, Journal of Heat Transfer.** vol. 81 : 175-186.

[7] Boldea, I. and Nasar, S.A. 2002. **The Induction Machine Handbook.** London : CRC Press.

[8] Bonnett, A.H. and Soukup, G.C. 1992. "Cause and Analysis of Stator and Rotor Failures in Three-Phase Squirrel-Cage Induction Motors." **IEEE Transactions on Industry Applications.** vol.28(4) : 921-937.

[9] Champrnois, G. Roye, D. and Zhu, D.S. 1994. "Electrical and Thermal Performance Predictions in Inverter-fed Squirrel Cage Induction Motor Drives." **EMPS.** vol.22(3) : 355-369.

[10] Farsane, K. Desevaux, P. and Panday, P.K. 2000. "Experimental Study of the cooling of a Closed Type Electric Motor.", **Applied Thermal Engineering 20(2000).** : 1321-1334.

[11] Gazley, C.Jr. 1958. "Heat Transfer Characteristics of the Rotational and Axial Flow Between Concentric Cylinders." **Transactions of the ASME.** vol. 80 : 79-90.

[12] Huai, Y. Melnik, R.V.N. and Thogersen, P. 2003. "Computational Analysis of Temperature Rise Phenomena in Electric Induction Motors." **Applied Thermal Engineering 23(2003).** : 779-795.

REFERENCES (CONT.)

[13] Institute of Electrical and Electronics Engineers. 1992. "IEEE Recommended Practice for Thermal Evaluation of Insulation Systems for Alternating-Current Electric Machinery Employing Form-Wound Preinsulated Stator Coils for Machines Rated 6900 V and Below", **IEEE 275.**

[14] International Electrotechnical Commission Standard 60085. 2004. **Electrical Insulation-Thermal Evaluation and Designation.** 3rd ed.

[15] Incropera, F. and De Witt, D.P. 1990. **Fundamentals of Heat and Mass Transfer.** 3rd ed. New York : McGraw-Hill Companies.

[16] Jaaskelainen, M. 2009. "Determination of Coefficients of Thermal Convection in a High-speed Electrical Machine." Master thesis. Helsinki University of Technology.

[17] Lee, S.B. Habetler, T.G. Harley, R.G. and Gritter, D.J. 2002. "An Evaluation of Model Based Stator Resistance Estimation for Induction Motor Stator Winding Temperature Monitoring." **IEEE Transactions on Energy Conversion.** vol.17(1) : 7-15.

[18] Myers, R.H. and Montgomery, D.C. 1995. **Response Surface Methodology.** New York : John Wiley & Sons Inc.

[19] Saari, J. 1995. "Thermal modeling of High-speed Induction Machines", Ph.D. dissertation, Helsinki University of Technology.

[20] Saari, J. 1998. "Thermal Analysis of High-speed Induction Machines", **ACTA Polytechnica Scandinavica Electrical Engineering Series**. vol.90.

[21] Sarkar, D. 1998. "Approximate Analysis of Temperature Rise in an Induction Motor During Dynamic Braking", **EMPS.** vol.26(6) : 585-599.

[22] Yoon, M.K. Kauh, K. 2005. "Thermal Analysis of a Small, Totally Enclosed, Fan-Cooled Induction Motor." **Heat Transfer Engineering.** vol. 26(3) : 77-86.

BIOGRAPHY

Name: Mr. Jenwit Soparat

Date of Birth: November 10, 1980

Place of Birth: Bangkok, Thailand

Education:

1998-2002	B. ME. Department of Mechanical Engineering, Faculty of Engineer, Kasetsart University
2007-2012	M.Eng. in Automotive Engineering (International program), International College, King Mongkut's Institute of Technology Ladkrabang (KMITL)

Honour and Scholarships:

2007-2009	Full scholarship for study in the master degree from National Science and Technology Development Agency (NSTDA)

Publications:

1. Soparat J., Benyajati C., Pitaksapsin N., Wattanawongsakun P., and Phuchumnong A., "Computational Study of Totally Enclosed Fan Cooled System in an Electric Induction Motor", 2010, 14th International Annual Symposium on Computational Science and Engineering (ANSCSE 14), March 23-26, 2010, Mae Fah Luang University, Chiang Rai, Thailand.
2. Soparat J., Benyajati C., Thianpong C., and Okawa S., "Development of a Liquid Cooling System for an Induction Motor", The 7th International Conference on Automotive Engineering (ICEA-7), March 28- April 1, 2011, Challenger, Impact, Muang Thong Thani, Bangkok, Thailand.

Computational Study of Totally Enclosed Fan Cooled System in an Electric Induction Motor

Jenwit Soparat ,Chi-na Benyajati, Narong Pitaksapsin, Prasit Wattanawongsakun, Anek Phuchamnong

National Metal and Materials Technology Center 114 Thailand Science Park, Pahonyothin Rd., Klong 1, Klong Luang, Pathumthani 12120

E-mail: jenwits@mtec.or.th ; **Fax**: 02-5646370; **Tel**. 02-5646500 ext 4357

ABSTRACT

In order to use an electric induction motor to power an automotive vehicle, consequential heat in a motor is one of key issues. Generally, an induction motor could be operating under high load for extensive periods. The generated heat in motor can cause damage on the motor or its parts, subsequently decreasing their useful lifetime. One of examples is an overheating of electric insulators coated on stator wires. This can cause an electrical short circuit and a motor failure. A Totally Enclosed Fan Cooled (TEFC) system is often used in a small size induction motor. Its general configuration consists of a fan attached on the rear-side of a housing case. A rotation of fan generates an air flow along the surface of housing case to remove the heat away from the induction motor. The objective of the current study is to demonstrate that the capacity of induction motor can be improved by using a higher efficiency fan cooling system.

This study is concerned with the effect of the air flow generated by fan which, in turn, affects the heat transfer on the induction motor. Main parameters of the TEFC cooling system that will be considered are fan and end cap geometries. For each case, the effect of the heat transfer on the induction motor will be simulated. The simulation results will be compared with those obtained experimentally from the prototype model of a 3 phases 4 poles induction motor rated at 5 horsepower. Finally, the studied parameters will be discussed to make the comparison of the variation of parameters.

Keywords: *Fan cooled, convection, induction motor*

1. INTRODUCTION

Due to a demanding nature of various applications, modern class of induction motors need to come in a compact size while performing with high efficiency and capable of running at high speed. All these demands indicate a higher working temperature of a stator wiring. As a result, a computational analysis becomes an important tool in enhancing the working performance of existing motor models. In a current study, a thermal analysis was carried out by means of a numerical method. The calculated results were then compared with those obtained experimentally from an actual induction motor.

The objective of the current study was to demonstrate that the capacity of TEFC induction motor could be improved by using a higher efficiency fan cooling system. The air flow generated by fan and its effect on the heat transfer on the induction motor were studied. Fan and end cap

geometries were main parameters of interest. The simulation results were compared with those obtained experimentally from a prototype model of a 3 phases 4 poles induction motor rated at 5 horsepower.

2. THEORY AND RELATED WORKS

Previously, there have been various studies on thermal performance of an electrical motor by using a thermal network method. [1,2,3] Majority of proposed models showed that a highest temperature would occur on the wiring on the stator. However, one of limitations for such method was that no detail of temperature contribution on motor parts was provided. Also, parts geometry was not taken into the account either.

These issues become apparent when the convection effect needed to be determined on motor with finned housing or other configurations. This was shown experimentally by Farsane et al. [4] who employed a Laser Doppler Anemometry technique to measure air velocity around the motor housing. It was reported that the shape of motor housing had a significant effect on both air velocity and a flow pattern along the housing. Thus, a performance of a motor cooling system could be directly affected by the design of housing and other parts.

3. EXPERIMENTAL AND COMPUTATIONAL DETAILS

Experimental - induction motor efficiency measurement

An induction motor efficiency testing was carried out according to international standards, IEEE 112 and IEC 34-2 [5]. Generally, a test motor was connected to a dynamometer which acted as a controlled load of the system. A load or a torque required to operate a dynamometer could be varied by means of a current adjustment while the rotational speed of the motor was kept at a rated value. Thermocouples were also attached on the outer surface of the housing to monitor corresponding temperature at various locations. Additionally, an infrared camera was employed to capture overall temperature distribution pattern at constant interval during the test. Each test was carried out under uniform conditions until a thermal equilibrium was observed.

Fig.1 setup of the induction motor efficiency measurement

Computational analysis – convection simulation on TEFC motor

A computational model for a convection analysis of the induction motor is displayed in Figure 2. The model mainly consisted of a finned-motor housing case, a fan, and a fan cap. All components were assembled and placed within a cube-shaped space filled with air. The total air region size was set to be 2 × 3 m with 1 m height. The air property was assumed to be in atmospheric conditions. The air velocity was generated by the movement of a fan which was mounted at the

rear of motor. The elements of the fan and nearby air were set to be the smallest, approximately 3mm, in order to resolve the steep gradients in the impeller region. Similarly, all spaces in the vicinity of vessel walls were meshed with a dense grid. Total meshing was approximately comprised of 400,000 nodes and 2,000,000 elements. The fan velocity was set at 1,450 RPM in a clockwise direction, in accordance with the experiment. A heat flux boundary condition was applied on inner surface of motor housing where there are contacts with a stator core. Referring to the motor efficiency test results, the heating value of 9800 W/m was used. Furthermore, a k-ε turbulence model was employed in a fluid dynamic part of the analysis.

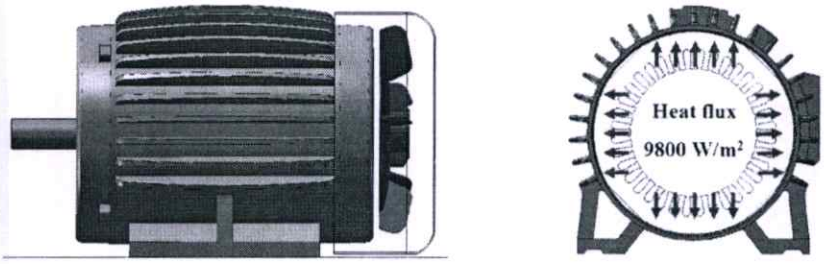

Fig.2 A computational model for a convection analysis of the induction motor

4. RESULTS AND DISCUSSION

Motor efficiency testing results

Total heat loss occurred in an induction motor could be considered to comprise four different heat sources i.e. stator, rotor, friction, and stray losses. Variation of losses determined under three different loading conditions, 100%, 125%, and 150%, is displayed in Figure 3.

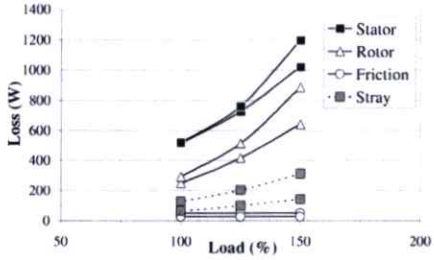

Fig.3 Losses in an induction motor at 100% , 125% and 150% of rated loads

Resulting total loss was found to be directly proportional to the applied load. It could be seen from the results that majority of heat came from stator and rotor components. The values included resistive losses occurred in copper wiring and induction bars for stator and rotor respectively. These obtained heat losses were used as a boundary condition for the thermal analysis. On the other hand, friction loss seemed to be minimally affected by load variation.

Computational Results

The results from the computational analysis mainly consisted of a resulting air flow pattern around the motor and a corresponding temperature distribution on the outer surface of the housing. Three different cases were considered: normal motor configuration, fan blade number variation, and end cap variation. For the initial case in which a motor used in the calculation was

identical to that employed in the experiment, the calculated air flow pattern is shown in Figure 4. It can be seen that the air velocity was relatively high near the tip of fan blades and around the gap between the end cap and the housing.

Furthermore, a velocity vector plot indicated that a movement of the fan drew the surrounding air through the end cap before propelling it onto the housing surface towards the front end of the motor (Figure 4b). Areas of circulating air flow were also determined in the frontal part of the motor. This might explain a relatively high temperature zone observed in this area via the thermal camera (Figure 5).

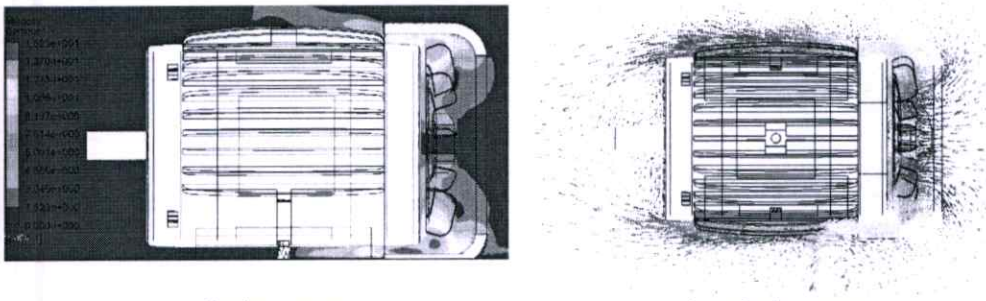

a. velocity contour b. velocity vector

Fig 4. The computational velocity of original model

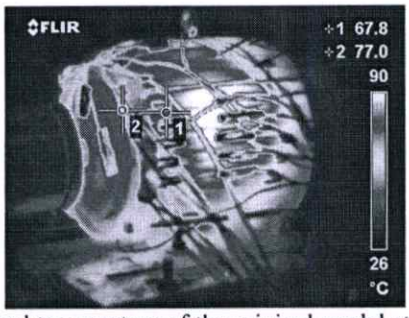

Fig 5. The measured temperature of the original model at 100% rated load.

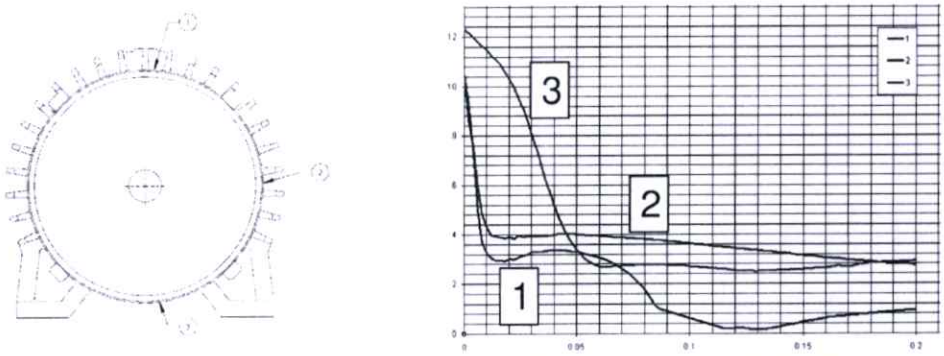

a. measurement position b. the comparison of velocity

Fig 6. The air velocity along the housing between the fins

The profiles of generated air velocity along the housing between the fins from three different locations are displayed together in Figure 6. Generally, the air velocity was relatively high coming out from the end cap at the rear side of the housing before rapidly dropping to a much lower value and steadily decline towards a front part of the housing. However, the velocity profile from bottom part of the motor (location 3) seemed to remain high for a longer distance compared to other locations. This could be due to a tunnel-liked air path that the motor housing formed with the floor. While the velocity profile at the top part of the motor (location 1) displayed another significant dip around half way through the housing. This was most likely because of the presence of a mounting holder for a carrying hook. It effectively acted as an air flow blockage. Furthermore, a good agreement could be seen from a velocity profile comparison between calculated and measured results at location 2 as shown in Figure 7.

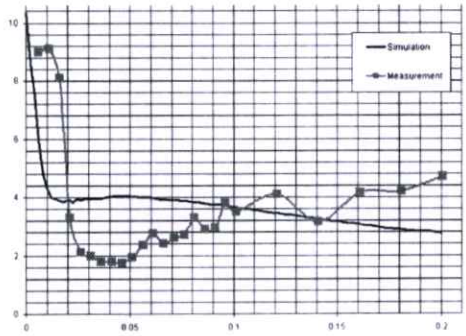

Fig 7. The velocity comparison between calculated and measured of the original model

A comparison of resulting temperature distribution on housing surface obtained via computational and experimental means is shown in Figure 8. It can be seen that the computational results displayed a distribution pattern in a similar fashion to that observed in the experiment despite some discrepancies in terms of temperature values. This could be supported by a temperature profile comparison between computational and experimental results as shown in Figure 9 for location 2. Good agreement between two sets of results can be clearly seen. A discontinuity seen in the experimental temperature profile was due to technical difficulty of an infrared camera to measure the temperature of reflective surface such as the adhesive tapes that were used to attach the thermocouples to the housing surface and all the wirings

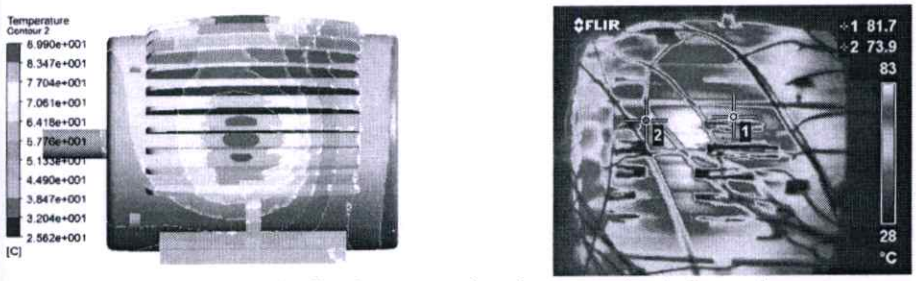

Fig 8. the temperature distribution comparison between simulation and measurement

Fig 9 The temperature profile comparison at location 2 of the original model

After it has been verified that the computational model shown in Figure 2 could be used to satisfactory predict the convection phenomena occurred on TEFC induction motor, the effect of a number fan blades on corresponding heat transfer was studied. The original fan was modified using CAD commercial software such that five different numbers of fan blade were studied i.e. 3, 5, 8, 10, and 15 blades. The calculated air velocity and surface temperature profiles along the housing for each case are shown in Figure 10. All the results were taken from location 2. For all number of fan blades considered, air velocity results displayed a similar trend to that obtained from the original case of 10 blades. However, small difference between each set of results could be seen such that the higher the number of blades, the higher the resulting air velocity. Similarly, the small difference between temperature results could also be seen. A higher number of blades yielded a slightly lower surface temperature of the housing. Furthermore, a significant difference between the temperature at the front and the rear section of the housing can be seen. This was most likely due to the rapid drop of air velocity profile as the air flowed from the end cap to the front section of the housing as explained earlier.

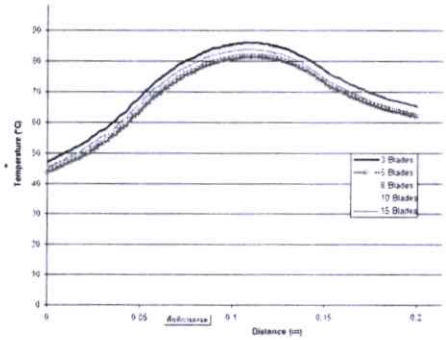

Fig 10. The temperature profile comparison of the variation of the number of fan blade at 3, 5, 8, 10 and 15 blades

In order to study the effect of end cap on heat transfer of induction motor, the end cap itself was removed from the computed model. The determined air flow and temperature results were compared with those obtained from the original case as shown in Figure 11. The distinction between with and without end cap can be clearly observed. Without the end cap, there seemed to be almost no air flowing along the housing compared to the case in which there was an end cap present. This could be displayed graphically by the streamline plot shown in Figure 12. Without the end cap, the air was just propelled outwards in radial direction rather than being guided to the housing. Thus, this resulted in a much higher housing surface temperature.

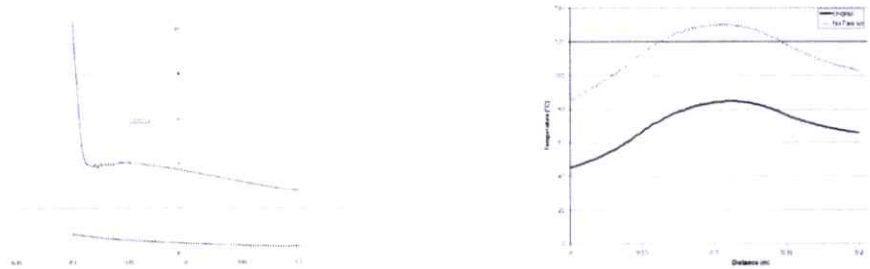

a. velocity profile b. temperature profile

Fig 11. The velocity profile and temperature profile comparison between original model and no end cap model

a. no end cap b. original

Fig 12. the streamline generated by the rear fan between the original model and no end cap model

5. CONCLUSIONS

A computational study was carried out to investigate the convective heat transfer phenomena in an electric induction motor. A 3 phases 4 poles TEFC induction motor rated at 5 horsepower was chosen as a model of interest in this study. Comparison between the analyzed results and those observed from the experiment, under the same settings, was found to be satisfactory. A small discrepancy presented, especially for corresponding temperature distribution, was probably due to a lack of knowledge on an accurate heat source inside the motor. Nonetheless, it was demonstrated that the resulting air flow pattern was very important while the shape of the housing could also have a significant effect on the flow pattern.

An analytical study on the effect of fan blade showed that by number of fan blade seemed to have only slight effect on the convection process. Another possible relevant parameter that would probably be interesting to investigate further is the shape of the blade itself. Furthermore, the importance of the end cap as part of the heat removal system in the TEFC configuration was highlighted. It was the geometry formed between the end cap and the housing that generate an air flow sufficiently needed to cool the motor.

Even though no practical recommendation regarding a motor design could be drawn at present, a computational approach has been shown as an effective tool in investigating the heat transfer process of the induction motor. It is therefore strongly recommended to be employed as a main designing tool for either inventing a new type of motor or improving the performance of the existing ones.

The 7th International Conference on Automotive Engineering (ICAE-7)
March 28 – April 1, 2011, Challenger, Impact, Muang Thong Thani, Bangkok, Thailand

Development of a Liquid Cooling System for an Induction Motor

JENWIT Soparat, CHI-NA Benyajati
Automotive Laboratory, National Metal and Materials Technology Center, Thailand

Assoc. Prof. Chinaruk Thianpong
Faculty of Engineering King Mongkut's Institute of Technology Ladkrabang (KMITL)

Assoc. Prof.Seiji OKAWA
Graduate School of Science and Engineering, Tokyo Institute of Technology, Japan

ABSTRACT

The present study involved investigating a heat transfer phenomenon in TEFC motor and determining the design criteria of liquid cooling for an induction motor application. The study of heat transfer phenomenon in TEFC motor was carried out by both experimental and computational means. Results were compared to work out the relevant heat source model of motor. This determined heat source model was then employed in designing a liquid cooling system. The calculated results could display the difference in cooling capacity between the two systems and the feasibility of employing the liquid cooling system was also discussed.

INTRODUCTION

Due to a demanding nature of various applications, modern class of induction motors need to come in a compact size while performing with high efficiency and capable of running at high speed. All these demands indicate a higher working temperature of a stator wiring. As a result, a computational analysis becomes an important tool in enhancing the working performance of existing motor models. In a current study, a thermal analysis was carried out by means of a numerical method. The calculated results were then compared with those obtained experimentally from an actual induction motor.

Previously, there have been various studies on thermal performance of an electrical motor by using a thermal network method. [1,2,3] Majority of proposed models showed that a highest temperature would occur on the wiring on the stator. However, one of limitations for such method was that no detail of temperature contribution on motor parts was provided. Also, part geometries were not taken into the account either.

These issues become apparent when the convection effect needed to be determined on motor with finned housing or other configurations. This was shown experimentally by Farsane et al. [4] who employed a Laser Doppler Anemometry technique to measure air velocity around the motor housing. It was reported that the shape of motor housing had a significant effect on both air velocity and a flow pattern along the housing. Thus, a performance of a motor cooling system could be directly affected by the design of housing and other parts.

The objective of this study is to develop a liquid cooling system for an induction motor which has more cooling capacity than existing TEFC motor. By using simulation approach, a new design of liquid cooling system was developed by applying the heat source which represented that occurred in TEFC motor at 100% rated load. Variables such as number of passages, and inlet flow rate were applied to the simulation to obtain the proper design for liquid cooling system. Finally, the calculated results of both models were compared by temperature distribution.

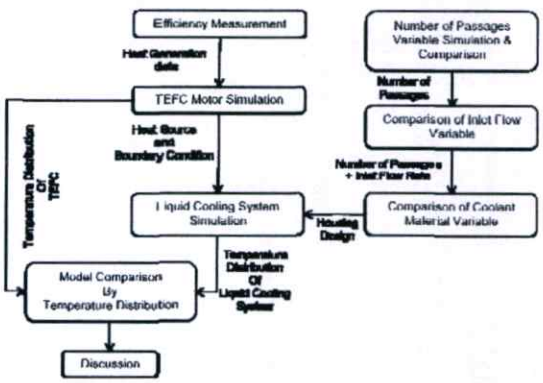

Figure 1 Procedures diagram of the study

METHOD AND PROCEDURES

The procedures diagram showing design and analysis involved in the present study is shown in Figure 1. Details of each part are explained in this section.

MOTOR EFFICIENCY TESTING

In an induction motor, the heat is emitted when the motor is operating. The heat is caused by friction, electrical resistant and electro-magnetic which occur in some components such as rotor, stator, and winding. The generated heat could be measured by an induction motor efficiency testing. In this study, an induction motor efficiency testing was carried out according to international standards, IEEE 112 and IEC 34-2 [5]. A test motor was connected to a dynamometer which acted as a controlled payload of the system. A payload or torque required to operate a dynamometer could be varied by means of a current adjustment while the rotational speed of the motor was kept at a rated value. Thermocouples were also attached on the outer surface of the housing to monitor corresponding temperature at various locations. Additionally, an infrared camera was employed to capture overall temperature distribution pattern at constant interval during the test. Each test was carried out under uniform conditions until a thermal equilibrium was observed.

Figure 2 Experimental arrangement of the induction motor efficiency measurement

HEAT TRANSFER SIMULATION ON TEFC MOTOR

In order to obtain the model of heat generation in a motor, the heat transfer model of TEFC was simulated based on the data of motor efficiency and temperature measurements. The relevant components used in the analysis are shown in Figure 3. The internal components such as rotor, stator core, and winding, were applied as the heat generating sources according to the results from the efficiency test. Two air domains were used in the analysis. One covered surrounding ambient while the another was contained inside motor housing. An air flow within the outside domain was generated by the fan component as a moving region to rotate around the rotor axis at 1450 RPM in counter clockwise direction. An ambient air temperature was assigned as a room temperature at 26°C. On the other hand, an air flow within the inside air domain was generated by the fan attached on both ends of the rotor component which rotated at the same speed as that of the fan.

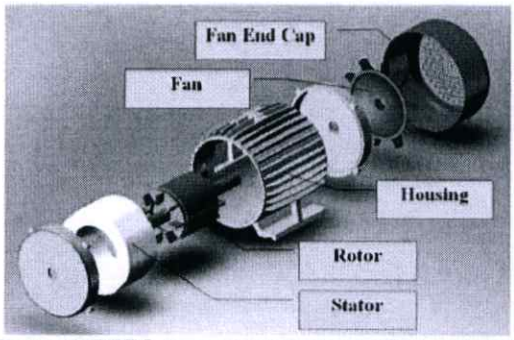

Figure 3 TEFC motor components for heat and flow analysis

LIQUID COOLING SYSTEM DESIGN

In an attempt to improve the cooling capacity of TEFC motor, the cooling fan was to be replaced with the liquid cooling system. An advantage of the liquid as a cooling medium is a higher specific heat capacity. However, the system configuration could become more complex than that of the fan cooled system. The liquid cooling system would be comprised of a radiator, also acting as coolant storage, a coolant pump, a valve, and a motor housing providing a passage for liquid coolant. The schematic of liquid cooling system is shown in Figure 4.

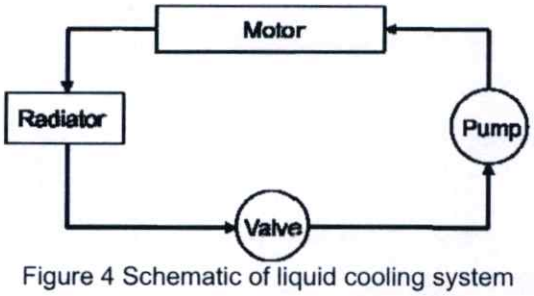

Figure 4 Schematic of liquid cooling system

A new housing for this study was designed by allocating a radial array of liquid passages on the housing. With such arrangement, a coolant liquid could flow in from the rear end of housing to the front end or vice versa. The conceptual design of the new housing for liquid cooling is shown on figure 5.

In order to optimize a liquid housing, there were 2 parameters of liquid cooling housing to be varied in this study, namely, a number of cooling passages and an inlet flow rate. The comparison and discussion was accounted on each parameter case by case. The cooling passage was designed by series of drilled troughs around the housing circumference from rear to front. The cross-section of the passage side wall was 6 mm width with 8 mm height. The number of passages was varied from 4 to 80 passages. In case of inlet flow rate, the comparison was account on the obtained new housing geometry. The flow rated was varied from 0.1 kg/s to 0.8 kg/s in reference to the commercial pump capacity.

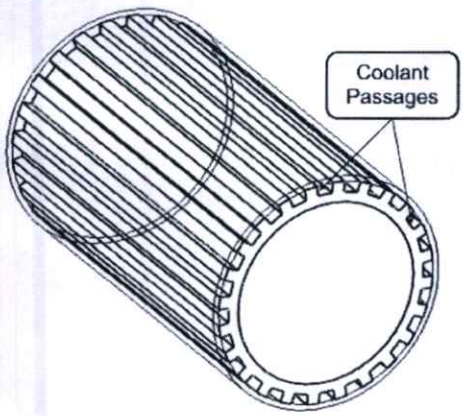

Figure 5 Coolant passages geometry for study on an effect of number of coolant passages

RESULTS

HEAT TRANSFER SIMULATION ON TEFC MOTOR

The applied heat generation on the rotor, stator core and winding are shown in Table 1. The heat generation was measured from the motor efficiency testing explained in previous section. There are 2 contact areas in an induction motor model. The first place was the contact area between the rotor-stator where the thermal contact resistance was set as 0.1 $K.m^2/W$. The other place was the contact area between the stator-housing where the thermal contact resistant was set as 0 $K.m^2/W$. The flow regime was turbulence flow which was assumed to be the K-ε model. As shown in figure 6, the air was generated from the tip of the blades and circulated along the tangential direction of fan rotation before flying pass the fan cap exit and along the housing fins. The velocity at the fan cap exit was approximately 15 m/s and decreased rapidly at the position far away from the fan cap exit towards the front of motor. Inside the housing, the flow was circulated according to the rotation of the rotor fan blades. The comparison between the measurement and the simulation of the velocity profile from the fan cap exit to the front end along the fin direction is shown in figure 7. Furthermore, a simulated temperature distribution of the TEFC motor in a sectioned view is displayed in Figure 8. These calculated thermal distribution results were then compared with the measurement by the infrared thermal camera on the outer surface of housing as shown in Figure 9. A good agreement can be clearly seen with the difference about 3-5°C.

Table 1 Quantity of heat generation on 5 HP motor components

Domain	Heat Generation (W)
Rotor	278.71
Stator Core	123.32
Copper Winding	393.62

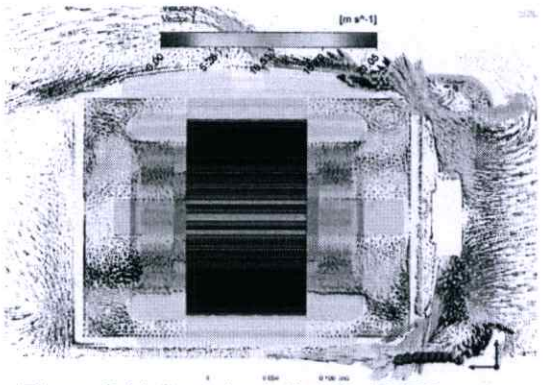

Figure 6 Air flow simulation for TEFC motor

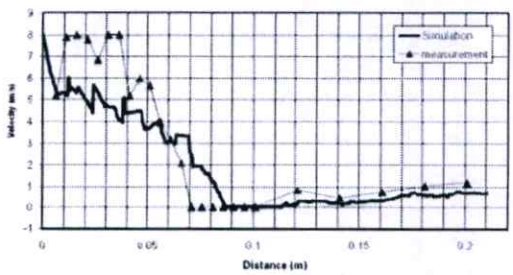

Figure 7 Air velocity comparison between simulation and measurement along the fin channel

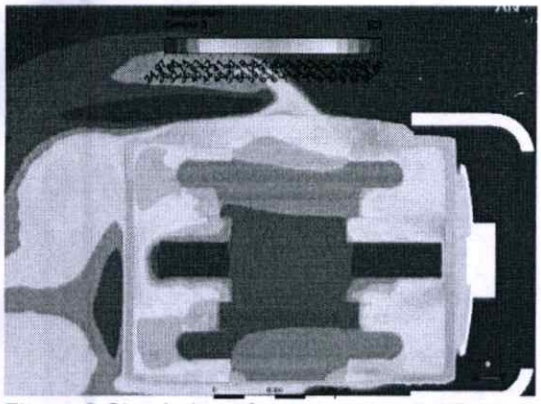

Figure 8 Simulation of temperature distribution around and inside TEFC motor

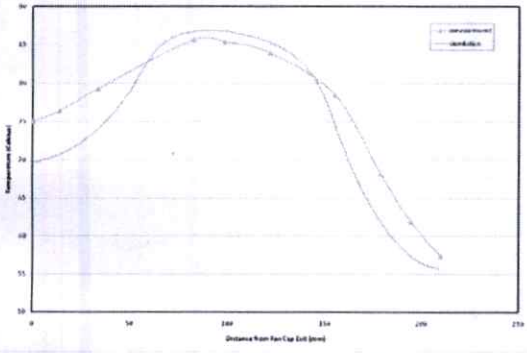

Figure 9 Comparison between computational and experimental results of TEFC motor temperature

RESULTS OF NUMBER OF COOLANT PASSAGE VARIABLE STUDY

Present topic was focused on the change of maximum temperature at the front end of rotor shaft resulting from additional passages in each design. The passages were placed on a radial array with equal spacing. By increasing the number of coolant passages, the contact area between the coolant and housing was also effectively increased. However, the maximum number of coolant passages would be limited by the size of designed housing. The boundary conditions of simulation was assigned as followed: the 100000 W/m^3 heat generation on the domain at the center of housing which was connected to the inner surface of housing, and the inlet flow of 0.1 m/s^2 at 26 $^{\circ}C$.

The estimated relationship between numbers of passage and resulting maximum temperature is shown in Figure 10. The results showed that increasing number of coolant passages could decrease the maximum temperature at the front end of rotor shaft. Besides, the decrease of maximum temperature shows a binomial relation to number of passages. According to calculated results, the minimum temperature could be obtained with 66 coolant passages under this particular flow rate and passage geometry.

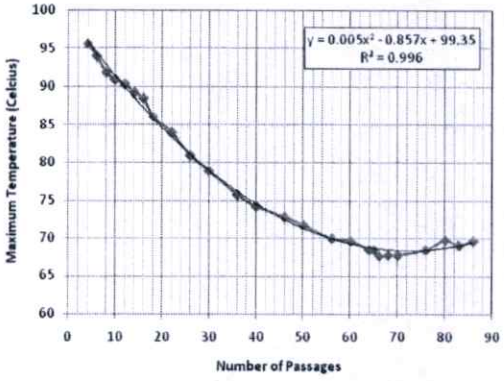

Figure 10 Comparison of the maximum temperature by the number of passages variable

HEAT TRANSFER SIMULATION ON LIQUID COOLING MOTOR

The best design of housing which has 66 coolant passages was positioned in place of existing TEFC housing. Several components such as fan and fan cap were removed from the model. The coolant inlet was located at the bottom of rear surface of housing while the outlet was positioned at the top of front surface of housing. The housing was assigned as aluminum with 4 mm thickness. This new design of liquid cooled motor is shown graphically in Figure 11.

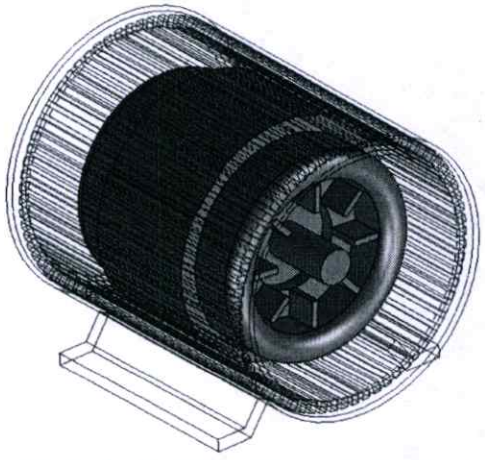

Figure 11 Overall geometry of the liquid cooling housing

In order to simulate the new liquid cooling system, the scope of simulation was focused on the motor only. The radiator and pump

were simplified to an inlet and outlet flow for the housing. The inlet flow rate was varied from 0.1 to 0.8 kg/s according to the commercial pump capacity. The inlet temperature was set at 60°C as the lowest temperature of the coolant liquid in actual situation. The heat generation was applied in a similar way to those used in TEFC motor analysis.

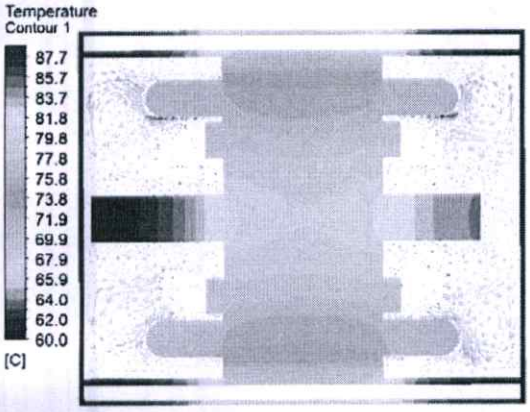

Figure 12 Temperature simulation results with 0.1 kg/s inlet flow rate of water coolant

With the inlet flow rate of 0.1 kg/s, the simulated temperature distribution is shown in Figure 12. The maximum temperature was 87.7 °C at the front end of rotor shaft. The results suggested that the liquid cooling system had more cooling capacity than that of an existing TEFC motor by reduction of 11.2 °C or 11.3% compared to the maximum temperature generated in TEFC motor.

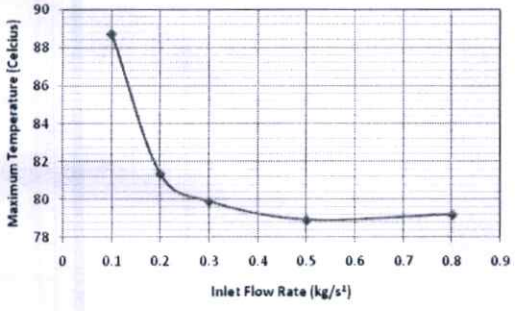

Figure 13 Variation of the maximum temperature of the 66 passages model as a function of the inlet flow rate

By varying the inlet flow rate, the relationship between the inlet flow rate and resulting maximum temperature is shown in Figure 13. According to this, the lowest temperature could be achieved with the inlet flow rate of 0.5 kg/m^3.

CONCLUSION AND DISCUSSION

The best conditions for liquid cooling system determined in this study was 66 coolant passages housing with water coolant operating at 0.5 kg/m^3 of inlet flow rate.

In practice, water has a high risk to cause a short circuit and electric hazard. The designer should be concerned with this issue. In manufacturing approach, the rectangular cross-section of coolant passages can lead to relatively high cost and production time. Therefore, it would be better to design the cross-section with a circular-shape which could be easily drilled by a simple machine tool.

ACKNOWLEDGMENTS

The authors would like to thank National Metal and Material Technology Center (MTEC) for research funding, and Mechanical Engineering department, Chulalongkorn University for the Infrared Thermal Camera.

REFERENCES

1. Y. Huai, RV.N. Melnik, P.B.Thogersen, *Computational Analysis of Temperature Rise Phenomena in Electric Induction Motors.* Applied Thermal Engineering 2003, 23, 779-795.
2. M.K. Yoon, S. K. Kauh, *Thermal Analysis of a Small, Totally Enclosed, Fan-Cooled Induction Motor*, Heat Transfer Engineering 2005, 26(4), 77-86.
3. J. Bellettre, V. Sartre, F. Biaist, A. Lallemand, *Transient State Study of Electric Motor Heating and Phase Change Solid-Liquid Cooling.* Applied Thermal Engineering, 1997, 17 (1), 17-31
4. K. Farsane, P. Desevaux, P.K. Panday, *Experiment Study of the Closed Type Electric Motor*, Applied Thermal Engineering 2000, 20, 1321-1334.
5. Anonymous, *IEEE Standard Test Procedure for Polyphase Induction Motors and Generators, IEEE Std 112-1996*, The Institute of Electrical and Electronics Engineers, USA, 1996
6. Y.Jaluria, *Design and Optimization of Thermal Systems*, 2nd Edition, CRC Press, USA, 753
7. S. Poncet, E. Serre, *High-Order LES of Turbulent Heat Transfer in a Rotor-Stator Cavity*, International Journal of Heat and Fluid Flow, 2009, 30, 590-601.
8. J. Saari, *Thermal Analysis of High-Speed Induction Machines*, Electrical Engineering Acta Polytechnica Scandinavica, 1998, 90.